NANOSCALE ENGINEERING FOR THE DESIGN OF EFFICIENT INORGANIC-ORGANIC HYBRID THERMOELECTRICS

A Dissertation

by

LANCE ROBERT BROCKWAY

Submitted to the Office of Graduate and Professional Studies of
Texas A&M University
in partial fulfillment of the requirements for the degree of

DOCTOR OF PHILOSOPHY

Chair of Committee,	Sreeram Vaddiraju
Committee Members,	Rusty Harris
	Tahir Cagin
	Mustafa Akbulut
Head of Department,	Nazmul Karim

May 2014

Major Subject: Chemical Engineering

ABSTRACT

Research aimed at enhancing the thermoelectric performance of semiconductors comprised of only earth-abundant elements has recently come under renewed focus as these materials systems offer a cost-effective path for scavenging waste heat. In light of the prediction that nanostructuring could increase the thermoelectric performance of materials; semiconductor nanowires comprised of non-toxic, low cost, and earth-abundant elements were synthesized and studied for their thermoelectric performance. For accomplishing this task, zinc phosphide (Zn_3P_2), zinc antimonide (Zn_4Sb_3), and zinc oxide (ZnO) nanowires were synthesized on the gram-quantity scale. Post-synthesis decomposition techniques were developed to controllably reduce the nanowire diameter and to create nanotubes. This decrease in nanowire diameter comes at an additional cost of an exponential decrease in surface stability. To combat this, a vapor phase surface passivation technique was developed to protect the nanowire surfaces from degradation and agglomeration. Finally, gram quantities of both functionalized and unfunctionalized nanowires were compressed into dense nanobulk pellets and characterized for their thermoelectric performance.

The reactive vapor transport synthesis technique resulted in gram-quantities of single-crystalline nanowires with consistent 20 nm diameters. The nanowire diameters were further reduced to create sub-5 nm quantum wires and nanotubes using controlled decomposition. A self-consistent mechanism to describe this phenomenon was proposed. The nanowires were further surface-functionalized with various organic molecules to

prevent surface degradation and to control the interfacial transport properties within the consolidated nanowire-pellets. The stability enhancement of the nanowires using this vapor-phase self-assembled monolayer technique was shown using traditional organic characterization techniques and suspension stability. Zn_3P_2 and ZnO nanowires were then hot-pressed and spark plasma sintered, respectively, into nanobulk pellets. It was observed that the nanowires in the Zn_3P_2 pellet did not break upon compaction, but bent elastically to achieve their sintered density; this was confirmed using a single nanowire inside a TEM. The thermoelectric performance of the functionalized nanowires was shown to be 3-fold higher than that of unfunctionalized nanowires due to less nanowire surface oxidation. Finally, the ZnO nanowire-bulk pellets were optimally-doped resulting in a 30% decrease in thermal conductivity compared to the bulk and the highest reported n-type oxide zT to date of 0.60.

ACKNOWLEDGEMENTS

I would like to thank the Vaddiraju research group for all of their help, guidance, and support throughout this research project including, but not limited to, Sreeram Vaddiraju, Yongmin Kang, Venkata Vasiraju, and Maxime Van Laer.

Additionally I would like to thank Jean-Pierre Fleurial and Sabah Bux of the NASA Jet Propulsion Laboratory for their generosity in helping with all of the thermoelectric materials characterization and facilities use. Also thanks to Jacek Jasinski of the Conn Center for Renewable Energy at the University of Louisville for his help with the transmission electron microscopy and data analysis.

Finally, I would like to thank my family for their encouragement throughout the entirety of this project.

NOMENCLATURE

4-ATP	4-Aminothiophenol
3DT	3-Propanedithiol
BDT	*p*-Benzenedithiol
COD	Crystallography Open Database
C_p	Heat Capacity
CVD	Chemical Vapor Deposition
D	Diameter
D_0	Initial Diameter
DSC	Differential Scanning Calorimetry
E_B	Energy Barrier
EDS	Energy Dispersive Spectroscopy
E_g	Bandgap
FFT	Fast Fourier Transform
FTIR	Fourier-transform Infrared Spectroscopy
h	Planck's Constant
HR	High Resolution
k_B	Boltzmann's Constant
L	Lorenz Number
LFA	Laser Flash Analyzer
m_e	Theoretical Electron Mass

m^*	Effective Electron Mass
n	Carrier Concentration
NW	Nanowire
P	Pressure
S	Seebeck Coefficient
SAED	Small Angle Electron Diffraction
SAM	Self-assembled Monolayer
SEM	Scanning Electron Microscopy
SLV	Solid-vapor-liquid
SPS	Spark Plasma Sintering
STEM	Scanning Transmission Electron Microscopy
STM	Scanning Tunneling Microscopy
t	Time
T	Temperature
TE	Thermoelectric
TEG	Thermoelectric Generator
TEM	Transmission Electron Microscopy
THF	Tetrahydrofuran
UV-Vis	Ultra-violet/Visible Spectroscopy
VLS	Vapor-liquid-solid
XPS	X-ray Photoelectron Spectroscopy
XRD	X-ray Diffraction

zT	Dimensionless Thermoelectric Figure of Merit
α	Absorption Coefficient
α	Thermal Diffusivity
Δ	Lattice mismatch
η	Reduced Fermi-level
κ	Total Thermal Conductivity
κ_l	Lattice Thermal Conductivity
κ_e	Electronic Thermal Conductivity
μ	Hall Mobility
ν	Frequency
ρ	Electrical Resistivity
ρ	Density
σ	Electrical Conductivity

TABLE OF CONTENTS

Page

LIST OF FIGURES

Page

LIST OF TABLES

Page

CHAPTER I

INTRODUCTION

Thermoelectric generators (TEGs) are solid state devices utilized to convert heat into electricity. These generators work by diffusing carriers down the temperature gradient from the device's hot side to cold side. This net movement of carriers generates an electric potential that can be used for power generation. State-of-the-art modules are currently made of rare and toxic materials; consequently, these heat engines are cost prohibitive for most terrestrial applications and are only used in specialty applications such as space exploration and remote power systems.[1, 2] Also thermoelectric generators are rather inefficient relative to other heat engines, with current materials boasting efficiencies of only 1/6 Carnot efficiency.[2] If the efficiency of TEGs can be increased while reducing materials costs, the market base could potentially be extended to automobile waste heat recovery,[1-3] small-scale cogeneration units,[4, 5] and topping cycles for gas turbines.[6, 7]

Semiconductors comprised of earth abundant elements have recently made large breakthroughs in thermoelectric performance due to their large elemental abundance, low cost, and relatively high stability under atmospheric conditions, relative to traditional thermoelectric materials. Therefore, the drive to make TEGs viable for terrestrial power generation using earth abundant semiconductors is substantial. In this context, the first question that must be addressed here is what materials give the best cost per Watt? After looking at various materials available, it was determined that very few

materials could compete with the extreme low cost of Zn_3P_2 and ZnO, yet they have not received the same attention from the thermoelectric community as Mg_2Si and $CoSb_3$, for example. Unfortunately, ZnO and Zn_3P_2 give subpar thermoelectric performance in the bulk material state. Hicks and Dresselhaus predicted that nanostructuring could increase the thermoelectric performance of materials of a given composition.[8] This leads to the second question: what nanomorphology can give the maximum efficiency boost to thermoelectrics? It was reported that nanowire morphology relative to nanoparticles can potential give the maximum gains in thermoelectric efficiency due to the long single-crystalline conduction pathways and ability to scatter phonons.[9] Unfortunately, typical synthesis techniques for nanowires do not result in wires small enough in diameter to observe properties unique to the nanoscale. Also, current methods to create nanowires with ultra-small diameters result in contamination by catalyst or chemical etchant. Furthermore, application such as thermoelectrics require mass production of nanowires, which has not been discussed extensively in the current nanowire synthesis literature. Therefore the next question arises: how can these nanowires be synthesized on a gram-quantity scale and their diameters be controllably reduced to observe these unique nanoproperties without degrading their pristine electronic properties from contamination? As the nanowire diameter decreases, the surface stability exponentially decreases. To make the nanowires process able at a low cost and under ambient conditions, the surfaces must be stable to atmospheric conditions. The surface area of nanomaterials is inversely proportional to their diameter and is typically over 10% of the entire volume compared to a fraction of a percent for bulk materials. This high reactivity

in conjunction with a high specific surface area leads to a high propensity to oxidation rendering the material useless for electronics. The next question then becomes how can the surfaces of nanowires be protected from degradation and agglomeration under ambient conditions? Additionally, the surface stabilization technique should also offer pathways for tuning interfacial transport between the nanowires. In the literature, there are few reports discussing the thermoelectric performance of individual nanowires. Although these studies exhibit excellent experimental control, high-resolution measurement techniques, and enhanced efficiency compared to the bulk, these single-nanowire devices are useless for harvesting waste heat on any appreciable scale due to low power output and heat transfer limitations. Therefore, to make nanowires useful on the large scale, how can the performance enhancements observed in single nanowires be extended to assemblies of large quantities of nanowires?

The overall objective of this dissertation is to answer these questions and deduce the maximum performance of nanowire-bulk thermoelectric modules. For iteration, the questions that will be answered are presented below:

1. How can nanowires of various earth-abundant semiconductors be synthesized on a large scale?
2. How can the diameter of these nanowires be controllably reduced to observe properties unique to the nanoscale?
3. How can the highly reactive surfaces of the nanowires be protected from degradation and agglomeration upon exposure to atmosphere using interfacial chemistry control?

4. How can the nanowires be assembled into macro modules without damaging the interfaces or losing the property enhancements unique to the nanoscale?

By the end of this document, it will be experimentally evident that the mass-production and assembly of nanowires with controlled interfaces can greatly increase the thermoelectric performance of materials, specifically those comprised of earth-abundant elements. This will be shown to be due to the retention of the nanowire morphology within the highly dense nanobulk pellets obtained by consolidating the nanowires. This is due to the nanowires bending elastically instead of breaking upon compaction. Not only will these strategies be shown to produce the highest cost specific power output thermoelectric modules to date, but they also will be able to compete in a total efficiency and weight specific power output.

This dissertation is divided into nine chapters, including this introduction chapter. Chapter II of this dissertation provides a general overview of relevant literature and background information, while Chapter III summarizes general nanowire synthesis and characterization methods. Chapter IV describes a controlled thermal decomposition technique to uniformly reduce the diameter of nanowires into quantum wires and their resulting properties. The variation of the thermal decomposition conditions can also create nanotubes using nanowires as templates. This result is discussed thoroughly in Chapter V. An *in situ* functionalization method for protecting the surfaces of nanowires is discussed in detail using Zn_3P_2 nanowires as an example system in Chapter VI. Finally, unfunctionalized and functionalized Zn_3P_2 nanowires were hot-pressed into

dense nanobulk pellets and the effect of the functionalization on the thermoelectric performance was discussed in Chapter VII. Chapter VIII describes how these oxide nanowires were pressed into optimally doped nanobulk solids using spark plasma sintering and characterized resulting in the highest n-type oxide zT reported to date. The conclusions drawn from the results in this dissertation and possible future work are discussed in Chapter IX.

CHAPTER II

LITERATURE AND BACKGROUND*

Waste Heat Recovery Using Thermoelectrics

Demand for energy in the United States has been on a constant rise, increasing from 62.9 quads (1 quad = 10^{15} BTU) in 1982 [13] to 97.3 quads in 2011 [14] according to estimates from the Energy Information Administration (EIA). The increase in the demand for energy has been met through increased generation from both renewable and non-renewable sources. Data from EIA also indicates that ~ 56-57% of the energy generated is consistently rejected as waste heat.[14] Future increases in the demand for energy, a certainty, can be met either through increased generation or by enhancing the energy efficiencies of the existing processes through waste heat scavenging. The potential amount of energy that could be saved through waste heat scavenging is staggeringly high, on the order of 10's of quads.[14] Solid-state thermoelectric modules could be used to convert a major portion of this waste heat into electricity, and thus increase the overall energy efficiency of the US. These solid-state thermoelectric modules offer many advantages over the conventional Rankine cycles in the scavenging of waste heat: they are portable, do not require intensive maintenance, have no moving parts, and last longer.[15]

---

* Excerpts are reprinted with permission from Cryst. Growth Des. **11** (10), 4559-4564 (2011) - Copyright (2011) American Chemical Society,[10] Physical Chemistry Chemical Physics **15** (17), 6260-6267 (2013) - Reproduced by permission of the PCCP Owner Societies,[11] and Nanotechnology **25,** 145401 (2014) - Copyright (2014) IOP Publishing.[12]

The efficiency of a thermoelectric material is gauged by the dimensionless figure of merit of a material, zT, is given by $zT = \frac{S^2\sigma}{\kappa_e+\kappa_L}T$ where S is the Seebeck coefficient, σ is the electrical conductivity, T is the absolute temperature, and κ_e and κ_L are the electronic and lattice contributions to the thermal conductivity, respectively. An ideal thermoelectric material has electrical transport properties of a heavily-doped semiconducting single crystal and the thermal conductivity of a glass.[15-17] In band-type semiconductors, Seebeck coefficient and electrical conductivity are inversely coupled via carrier concentration, and the Wiedemann-Franz law proportionally couples electrical conductivity and electronic thermal conductivity.[15] These restrictions make engineering high-efficiency thermoelectric materials very difficult and have resulted in commercial materials having zTs of ~1.[2] Therefore, one possible route for increasing the zT of optimally-doped band-type materials requires selectively reducing the lattice thermal conductivity via scattering at boundaries and interfaces. One way to enhance this scattering and reduce κ_L is to increase the number of interfaces within a material via nanostructuring.[8, 18] Relative to other nanomorphologies, single-crystalline nanowires were previously shown to enhance charge transfer within a nanobulk TE material,[19] potentially giving the highest zT for a given optimally-doped material. If the efficiency of thermoelectrics can be increased while reducing materials costs, the market base could potentially be extended to automobile waste heat recovery,[1-3] small-scale energy cogeneration units,[4, 5] and topping cycles for gas turbines.[6, 7]

Nanowire Thermoelectrics

Theoretical and more recent experimental studies indicated that thermoelectric efficiency can be increased via enhanced phonon scattering at boundaries interfaces using nanostructuring of materials.[20, 21] Specifically, materials in nanowire form with either small diameters or rough surfaces have been shown to exhibit lower thermal conductivities relative to their bulk counterparts, without exhibiting any adverse changes in their electrical conductivities. For example, Boukai *et al*. reported efficiency enhancements as high as 100-fold in silicon by using nanowire morphology.[22] They also demonstrated the ability to control the temperature at which maximum zT is attained by tuning the diameters and the carrier concentrations of the silicon nanowires.[22] Hochbaum *et al*. showed a 50-fold enhancement in the *zT* of silicon nanowires relative to the bulk by creating rough surfaces to reduce the phonon transport via boundary scattering.[23] Zhou *et al*. measured the thermoelectric transport properties of individual electrodeposited Bi_2Te_3 nanowires and reported not only a decrease in the thermal conductivity, but also an enhancement in the power factor relative to the bulk.[24] Li *et al*. fabricated bismuth nanotube arrays and indicated that the formation of a metal-semiconductor transition at lower wall thicknesses enhances their thermoelectric performance due to quantum confinement.[25] This same transition was also shown in thin bismuth nanowires.[26] What is currently not known is whether the thermoelectric performance of individual nanowires translates to bulk assemblies of nanowires and how these nanowires can be synthesized on a large-scale.

Selection of Materials

A semiconductor useful for thermoelectrics, zinc phosphide (Zn_3P_2), is a metal deficient p-type semiconductor with a bandgap of 1.5 eV.[27, 28] It is also relatively inexpensive and is comprised of components that are abundantly available in the earth's crust.[29] One of the problems plaguing the fabrication of thermoelectrics based on Zn_3P_2 is its low surface stability in the presence of moisture[30] and oxygen.[31, 32] Typically, Zn_3P_2 reacts with moisture to form zinc hydroxide (reaction 1) and with oxygen to form zinc phosphate (reaction 2). This problem is amplified when Zn_3P_2 is synthesized in nanomaterial format due to the higher specific surface area, and consequently, higher reactivity relative to the bulk.[33, 34]

$$Zn_3P_2 + 6H_2O \rightarrow 3Zn(OH)_2 + 2PH_3 \quad (1)$$

$$Zn_3P_2 + 4\ O_2 \rightarrow Zn_3(PO_4)_2 \quad (2)$$

As mentioned in Chapter I, even though both Zn_3P_2 nanowires and nanoparticles can be used for the fabrication of energy conversion devices,[35, 36] enhanced charge transfer is possible in nanowire format.[37, 38] Consequently, Zn_3P_2 nanowires are an ideal material and format to be used in energy conversion devices including thermoelectrics. Employing Zn_3P_2 nanowires for the fabrication of energy conversion devices requires their synthesis on a gram-quantity scale and stabilizing their surfaces to enhance resistance against air- and moisture-assisted degradation.

Similarly, "Zn_4Sb_3" (β-$Zn_{13}Sb_{10}$) is a p-type metal deficient valence semiconductor that can be used to convert waste heat into electricity. Zn_4Sb_3 exhibits the "phonon-glass electron crystal" behavior that is desired in thermoelectric materials due

to substantial zinc disorder and glass-like interstitial sites within its lattice.[17, 39] The high thermoelectric figure of merit of this material can be attributed to this disordered lattice scattering phonons, and results in the lowest thermal conductivity of all optimally doped p-type thermoelectric materials.[17] Nanostructuring has been predicted to enhance the thermoelectric efficiency of materials by reducing their lattice thermal conductivity.[8, 18] Additionally, single-crystalline nanowires have been shown to have enhanced charge transfer relative to other nanomorphologies.[19] Consequently, Zn_4Sb_3 in nanowire morphology has the potential to further enhance the already significant figure of merit of bulk Zn_4Sb_3. Like Zn_3P_2, there have been no previously reported gram-scale synthesis techniques for zinc antimonide.

Over the past two decades oxides have become viable thermoelectric materials due to their low cost, elemental abundance in the earth's crust,[29] low toxicity,[40] and high stability relative to other state-of-the-art thermoelectric materials in oxidizing environments.[40, 41] Many p-type materials have been shown to have thermoelectric performance on par with current commercial materials. Some of these polycrystalline materials include layered cobaltites such as $Ca_3Co_4O_9$[42-47] with a high zT of 0.61[45] and Na_xCoO_2[48-51] with a high zT of 0.92.[51] Contrarily, many n-type oxides have yet to exhibit such performance. The state-of-the-art n-type oxide thermoelectrics are $SrTiO_3$[52-57] with a high zT of 0.37[57] and ZnO alloy ceramics. Attempts to increase the efficiency of ZnO-based thermoelectrics using homologous compounds of $ZnO\text{-}In_2O_3$ resulted in small efficiency increases.[58-61] Doping[62-65] and co-doping[66-69] of ZnO with aluminum has

shown to give the highest n-type zT of 0.65 in $Zn_{1-x-y}Al_xGa_yO$ alloys.[69] The samples with the high zTs were bulk materials with very high thermal conductivities.

Nanowire Synthesis and Diameter Control

A review of the literature shows that the small-scale synthesis of Zn_3P_2 nanostructures has been reported. These reports include Zn_3P_2 trumpet-like nanostructure synthesis using a thermochemical method,[70] branched Zn_3P_2 nanostructure synthesis using laser ablation,[71] Zn_3P_2/ZnO and Zn_3P_2/ZnS core/shell nanowire synthesis using chemical vapor deposition,[72] and Zn_3P_2 nanowire synthesis using a simple evaporation process.[73] In all these studies, single-crystalline nanowires were obtained. None of these reports discussed the production of gram quantities of nanowires. However, a handful of reports in the literature discuss strategies for the mass production of nanowire powders using solution-based chemistry,[46] metathesis,[45] or an atmospheric plasma jet.[47] All of these methods either involve the use of noble metal catalysts, oxide assisted growth, or are limited in application to a few material systems.

There is also only one previously published report on the synthesis of Zn_4Sb_3 nanowires.[74] Chemical vapor transport of zinc and antimony from a Zn_4Sb_3 powder source onto silicon substrates led to the formation of nanowires in this study. Although the nanowire growth mechanism is not explicitly discussed, self-catalysis via the zinc droplets at the tips of the nanowires is the most probable mechanism in the absence of catalysts and contaminants.

Consequently, nanostructuring could potentially increase the thermoelectric performance of all the above material systems resulting in large decreases in the lattice thermal conductivity and increases in zT. When using materials in nanowire format, this can be accomplished by reducing the limiting dimension of the material: the nanowire diameter.

Vapor phase synthesis of nanowires was mainly accomplished in the past using catalyst-mediated techniques,[75-80] oxide-assisted methods[81-83] or direct synthesis schemes.[84-89] Typically, these processes suffer from two distinct disadvantages. Either the diameters of the nanowires obtained were greater than 20 nm,[75-89] or the nanowires obtained were contaminated with the catalyst metal.[90, 91] Typically, nanowire diameters need to be less than 20 nm to observe any quantum confinement effects in many of the III-V semiconductors. For example, diameters less than 11 nm are necessary to observe quantum confinement effects in GaN.[92-94] Unfortunately, this decrease in diameter exponentially increases the surface reactivity of nanomaterials. Consequently, the surfaces of the nanomaterials should be passivated to maintain their properties.

Surface Passivation

Attempts have also been made to passivate the surfaces of many metals[95-99] and compound semiconductors,[97] including compound semiconductors of zinc using thiols. For example, Sadik *et al.* studied the passivation of ZnO films with dodecanethiol molecules. It was observed that the surface coverage of the organic molecules on the zinc terminated surfaces was twice that of the oxygen terminated surface.[100] The

formation of Zn-S bonds between thiol functionalized ruthenium dye molecules[101] and mercaptosilanes[102] on nanoscale ZnO surfaces was also reported by Singh *et al.* Budz *et al.* compared many methods of surface treatment including atomic hydrogen cleaning, plasma treating, liquid phase assembly, and vapor phase assembly of octadecanethiol on GaAs surfaces.[103, 104] It was determined that the functionalization of the surface inhibited oxide formation. It was also observed that vapor phase functionalization offered better surface coverage of the functional molecules compared to liquid phase functionalization.[103] Sarigiannidis *et al.* grew ZnSe nanocrystals in the presence of pentanethiol, supplied via the vapor phase, and reported increases in surface stability. However, the concurrent supply of both pentanethiol and the precursors required for the formation of ZnSe crystals adversely impacted the morphology and size of the crystals obtained.[105] Holmberg *et al.* synthesized germanium nanowires and *in-situ* passivated their surfaces with thiols and alkenes in the liquid phase to show oxidative corrosion resistance.[106]

Nanobulk Materials

Typically, nanostructuring in bulk-3D solids is accomplished by ball-milling,[107] solidification,[108] eutectoid decomposition,[109] and precipitation.[110] These methods often result in insulating grain boundaries, a wide range of nanostructure sizes, and inconsistent results. Consequently, a bottom-up method to assemble nanowires into dense nanobulk masses without losing their morphology is required to overcome the shortcomings of current nanostructuring techniques. This can be accomplished by using

hot-pressing and spark plasma sintering (SPS).[111-113] It is important when using these techniques to achieve high consolidated-densities with no porosity,[114] while minimizing grain growth to maintain the nanostructuring[115] and achieve the maximum thermoelectric efficiency. Relative to conventional methods, this bottom-up oriented nanowire method can deliver advantageous properties including independent selection of the nanowire material and nanowire aspect ratio. There are also only very few reports that discuss the bottom-up assembly of nanowires, and all of these reports are based upon Bi_2Te_3 heterostructures.[116, 117] There are no other reports of large-scale nanowire assembly to date.

CHAPTER III

NANOWIRE SYNTHESIS AND CHARACTERIZATION METHODS*

Introduction

This chapter describes the techniques employed for the synthesis and characterization of nanowires and nanowire assemblies. More specifically, reactive vapor transport approaches utilized for the synthesis of binary compound semiconductor nanowires will be presented in detail. Additionally, the techniques utilized for consolidating nanowires, along with those used for measuring the nanowire-bulk electrical and thermal transport properties are discussed.

Multiple techniques were employed in this work for characterizing nanowires, including X-ray diffraction (XRD), scanning electron microscopy (SEM), transmission electron microscopy (TEM), small angle electron diffraction (SAED), energy dispersive spectroscopy (EDS), X-ray photoelectron spectroscopy (XPS), ultraviolet-visible spectroscopy (UV-Vis), and Fourier-transform infrared spectroscopy (FTIR). Many of these techniques were also utilized on the consolidated nanowire-bulk pellets. The thermoelectric performance of each nanowire-bulk system was gauged by the thermoelectric figure of merit. Determination of the figure of merit required measurement of the Seebeck coefficient, Van der Pauw electrical conductivity, Van der

---

* Excerpts are reprinted with permission from Cryst. Growth Des. **11** (10), 4559-4564 (2011) - Copyright (2011) American Chemical Society,[10] Physical Chemistry Chemical Physics **15** (17), 6260-6267 (2013) - Reproduced by permission of the PCCP Owner Societies,[11] and Nanotechnology **25,** 145401 (2014) - Copyright (2014) IOP Publishing.[12]

Pauw Hall coefficient, thermal diffusivity by laser flash analyzer (LFA), density by Archimedes Principle, and heat capacity from differential scanning calorimetry (DSC). All of these techniques for the synthesis and characterization of nanowires and their assemblies, and the information obtained from them, are discussed in detail in the following sections.

Nanowire Synthesis Methods

Reactive vapor transport in multiple CVD chambers were used to synthesize the GaN, Zn_3P_2, and Zn_4Sb_3 nanowires utilized for this dissertation. Schematics of the reactors along with experimental conditions used for the synthesis of the nanowires are included in the sections below.

GaN Nanowire Synthesis

The synthesis of GaN nanowires was performed in a custom-built chemical vapor deposition (CVD) chamber (Figure 1). This stainless steel vacuum chamber, capable of operating at pressures as low as 1 mTorr, is connected to mass flow controllers (1479A type mass flow controllers from MKS Instruments, Inc.) for the controlled flow of both hydrogen and ammonia into the chamber, and a pressure transducer (KJLC 317 type from Kurt J. Lesker Company®) for the measurement of pressure. The CVD chamber is also equipped with a ceramic substrate heater that can be heated to temperatures as high as 1400 ^{o}C. This setup was also described in detail previously.[88]

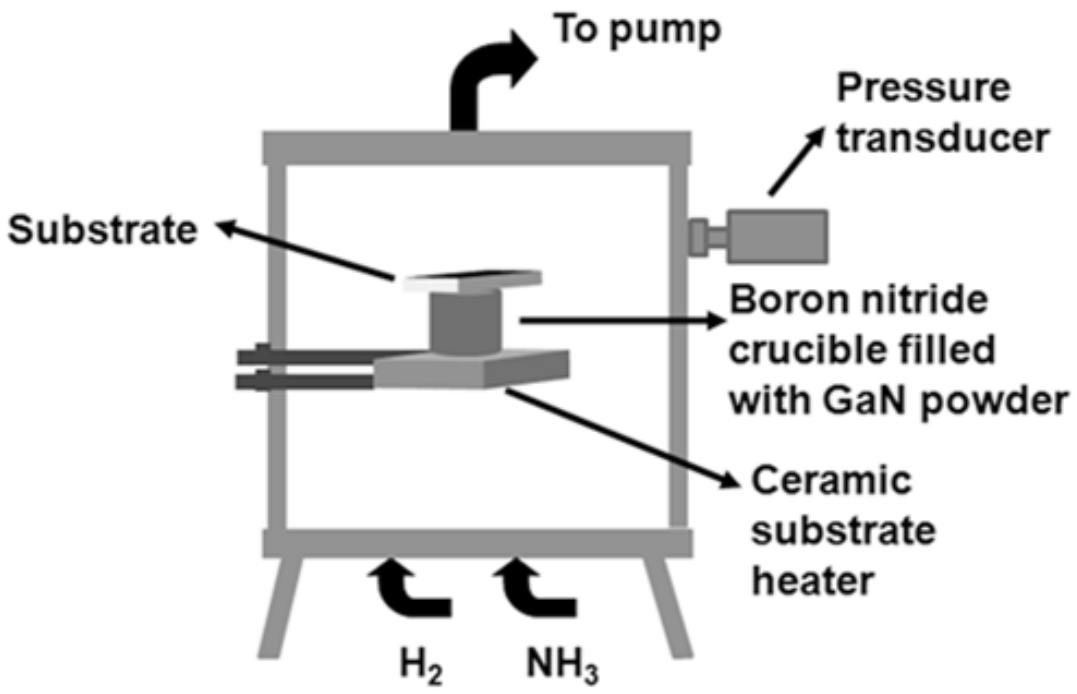

Figure 1. Schematic of the reactor used to synthesize GaN nanowires courtesy of Sreeram Vaddiraju.

Synthesis of GaN nanowires was performed in a manner similar to that described by Li *et al.*[86], using the reactive vapor transport approach [85, 86, 88, 89] with GaN powder and NH_3 as the sources for gallium and nitrogen, respectively. The GaN source was placed in a heated crucible, and the substrate was physically placed on top of this crucible. The distance between the source and crucible was adjusted to 2 mm. The temperature of the substrate was measured using a backside thermocouple placed on the side of the substrate not facing the GaN powder source. All the experiments were performed under an ammonia flow of 75 sccm, at a substrate temperature of 850 ^{o}C and at a pressure of 100 mTorr. The typical duration of the synthesis experiments was 20 minutes.

II-V Nanowire Synthesis

Zn_3P_2 nanowires were synthesized using reactive vapor transport in a three-zone hot-walled chemical vapor deposition (CVD) chamber. A schematic of this chamber is shown in Figure 2. This hot-walled CVD chamber is primarily comprised of a 1.5 inch diameter quartz tube housed inside a three-zone high temperature furnace (Thermo Scientific Lindberg/Blue M). One end of the quartz tube is connected to mass flow controllers, while the other end is connected to a pressure transducer and a pump. The functional molecules necessary for the *in-situ* functionalization were held in a bubbler (Precision Fabricators, Ltd) and connected to the upstream end of the reactor. The organic molecules were transported to the substrate by heating the bubbler to achieve the desired vapor pressure using a heating tape.

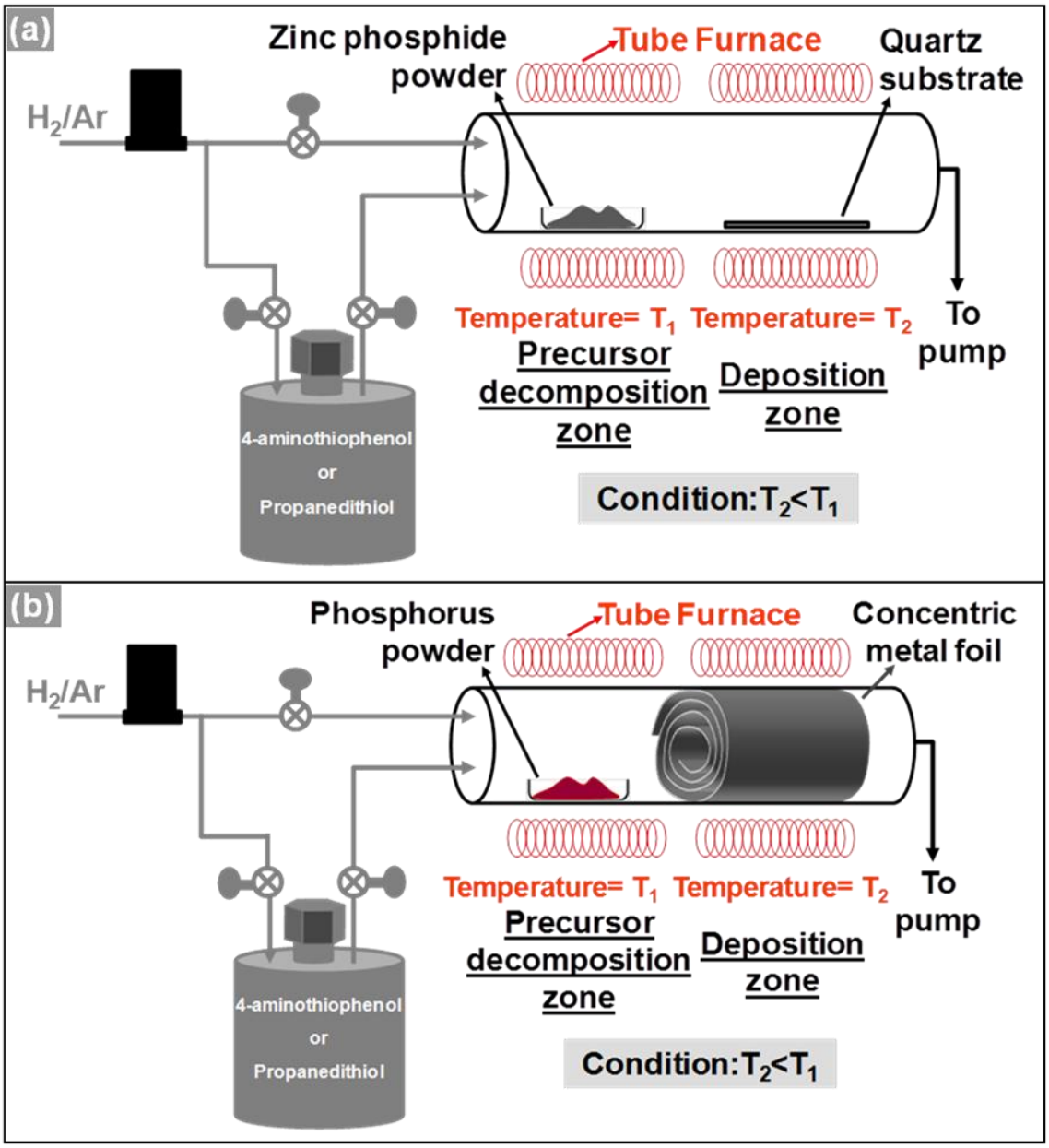

Figure 2. Schematic of the three-zone tube furnace employed for the synthesis and *in-situ* functionalization of Zn_3P_2 nanowires, indicating (a) the placement of the quartz substrate for the reactive vapor transport of zinc and phosphorus using Zn_3P_2 powder as the source for obtaining Zn_3P_2 nanowires on a small-scale (first experimental route), and (b) the placement of the coiled zinc foil employed for the large-scale synthesis of Zn_3P_2 nanowires using phosphorus vapor transport onto zinc foils (second experimental route).

The synthesis of Zn_3P_2 nanowires was accomplished using either (i) commercially-available Zn_3P_2 powder (Figure 2a) or (ii) a combination of zinc foils and red phosphorus powder as sources (Figure 2b). In the first route, 20 mg of Zn_3P_2 was placed in a boron nitride crucible and vapor transported onto amorphous quartz substrates. Using this method the Zn_3P_2 powder source was upstream at a temperature of 1000 ^oC, while the amorphous quartz substrates were downstream at a temperature of 600 ^oC. Hydrogen was used as a carrier gas at 20 sccm to aid in the source transport. These experiments lasted for one hour at an operating pressure of 1 Torr.

In the second route, phosphorus was vapor transported onto zinc foils for the synthesis of Zn_3P_2 nanowires (Figure 2b). Here, 250 mg of red phosphorus was placed in a boron nitride crucible at the hot end of the reactor maintained at a temperature of 480 °C, while zinc foil substrates cleaned using a 1M HCl solution for 5 minutes were placed at the downstream end of the reactor maintained at a temperature of 400 °C. Similar to the first experimental route, a flow of 20 sccm of hydrogen gas aided in the vapor transport of phosphorus onto zinc foils. These experiments also lasted for one hour and were performed at a pressure of 1 Torr.

Likewise, the synthesis of Zn_4Sb_3 nanowires was achieved by passing an antimony precursor over heated zinc foils. One gram of antimony trichloride, $SbCl_3$, was placed in the upstream end of the reactor maintained at a temperature of 280 ^oC. A flow of 20 sccm of hydrogen was used as a carrier gas to transport the $SbCl_3$ onto the cleaned zinc foils placed at the downstream end of the reactor and maintained at a temperature of

400 ºC. These experiments lasted a total duration of one hour and were conducted at a pressure of 1 Torr.

The ZnO nanowires were synthesized using an atmospheric plasma jet reactor[118] at the University of Louisville in Dr. Mahendra Sunkara's laboratory.

Nanowire Characterization Techniques

All the techniques employed for the characterization of nanowires were previously listed. SEM was employed for determining the morphology of the nanowires using the secondary electron detector and if the sample is phase-pure using the back-scattered electron detector. Further, an EDS attachment on the SEM was utilized to determine the elemental composition of the nanowire-bulk samples. Additionally, XRD was used to determine the crystal structure, lattice parameter, and mean particle size of a nanowire sample. TEM was further used to confirm the results of the SEM and XRD by generating electron diffraction (SAED) patterns to determine morphology, crystal structure, and growth direction. XPS was used to determine the bonding and chemical composition of a material. Also optical techniques, such as UV-Vis spectroscopy, were used to determine the bandgap of semiconductors. FTIR spectroscopy was used for determining how organic molecules are bound together or bound to nanomaterial surfaces. All of these techniques are commonly used to characterize materials and a plethora of information available on each of them can be found elsewhere.[119-124] In the interest of brevity, these techniques not be further described.

Nanowire Consolidation Techniques

The Zn_3P_2 and ZnO nanowires were compressed into dense bulk solids using hot-uniaxial pressing and spark plasma sinter (SPS), respectively. In the case of Zn_3P_2 nanowires, 1 gram of nanowires, either functionalized or unfunctionalized, were loaded into a 12 mm graphite die inside of an argon atmosphere glove box. The die was then sealed and transported to the uniaxial hot-press where the nanowires were sintered into a bulk mass for 1 hour at 650 °C and 100 MPa. The pellet was then removed from the die and mechanically polished to the specifications required by the characterization techniques listed below.

The dually-doped ZnO nanowire bulk pellet was manufactured using a different procedure and pressing technique. ZnO nanowires used as a starting material for this study were synthesized using a microwave plasma jet reactor and were previously reported.[118] These nanowires were mixed with Ga_2O_3 and Al_2O_3 nanoparticles in various ratios in a high-energy ball mill for 15 minutes at 20 Hz. The ceramic powders were then placed into a graphite die and consolidated using a Spark Plasma Sintering (SPS) apparatus. The nanowires were pressed at 1200 °C and 100 MPa for 5 minutes and then cooled to room temperature using water cooling. The consolidated $Zn_{1-x-y}Al_xGa_yO$ pellets were then removed from the die and polished into flat 12 mm diameter by 1 mm thick cylindrical pellets. As these powder metallurgy techniques are widely known and used, they will not be discussed in further detail. Any additional information regarding these techniques can be found in various published sources.[111-113]

Thermoelectric Performance Characterization

Van der Pauw probe Hall Effect measurements were used to determine the carrier mobility, carrier concentration, and electrical resistivity of each of the samples as a function of temperature. Seebeck coefficient was determined by applying a temperature gradient across the sample and measuring the voltage generated using W-Ni thermocouples. In all cases, pressure contacts were used. The thermal diffusivity was measured using a Netzsch LFA. Density measurements were determined using geometrical measurements and confirmed using Archimedes principle. The heat capacity was determined using DSC. From all of these properties, the thermoelectric figure of merit can be determined. Again, due to all of these measurements being standardized, they will not be further elaborated on. Additional information on these characterization methods can be found in the provided references.[125-128]

CHAPTER IV

POST-SYNTHESIS FORMATION OF QUANTUM WIRES*

Introduction

As mentioned in Chapter II, only a few reports in the literature discussed the syntheses of nanowires with diameters less than 20 nm. A few examples include the synthesis of 7.8 nm diameter silicon and 5 nm diameter germanium nanowires by the laser ablation method using gold and iron as the catalysts by Lieber and coworkers,[129] the synthesis of 15 nm diameter silicon nanowires using $TiSi_2$ followed by surface oxidation to reduce the diameter of the silicon core by Kamins and coworkers,[130] and synthesis of InP rods with diameters as small as 3 nm in diameter by thermal decomposition of an InP-containing metalorganic precursor by Nozik and coworkers.[131] Further, Korgel and coworkers synthesized silicon nanowires as small as 4 nm[132] and germanium nanowires as small as 7 nm[133, 134] by the supercritical fluid-liquid-solid (SFLS) method using gold as the catalyst. A 0.3 eV shift in the bandgap of germanium was observed at these small diameters. Solution phase synthesis of 7 nm diameter and 9 nm diameter CdSe nanowires using gold as the catalyst was also demonstrated by Kuno and coworkers.[135] In a series of papers, Buhro and coworkers have also reported the synthesis of InP,[136] CdSe,[137] ZnSe-ZnTe,[138] and InAs[139] nanowires using the solution-liquid-solid (SLS) method. Recently, SnO_2 nanorods with diameters as small as 2 nm

---

* Excerpts are reprinted with permission from Cryst. Growth Des. **11** (10), 4559-4564 (2011) - Copyright (2011) American Chemical Society.[10]

have also been synthesized.[140] In general, it is observed that the vapor-liquid-solid (VLS) mechanism rarely yields wires with diameters less than 20 nm, while the SLS mechanism typically yields nanowires with diameters in the range of 4-10 nm.[141] Unfortunately, the SLS mechanism has not resulted in high quality nitride nanowires.[141] Due to the inability of the current methods in synthesizing nanowires with sub-10 nm diameters (or quantum wires), especially in III-nitride systems, a post-synthesis approach for reducing the diameter of nanowires would be ideal for obtaining quantum-sized nanowires in a reliable manner, irrespective of the technique used for their synthesis.

Two post-synthesis strategies useful for reducing the diameter of nanowires are thermal decomposition and chemical etching. In the case of III-nitrides nanowires, it is possible to devise strategies based on thermal decomposition easily. For example, it is well-known that GaN decomposes above temperatures of 850 ^{o}C. Consequently, it is important to know whether the decomposition of pre-synthesized GaN nanowires leads to a reduction in their diameters. Secondly, it is crucial to know if this diameter reduction is uniform all along the lengths of the nanowire. Finally, it is imperative to understand the parameters affecting the decomposition to obtain nanowires with diameters less than 10 nm in a uniform and controlled manner.

Therefore, the primary aim of this chapter is to study whether post-synthesis decomposition could be employed as a strategy for reducing the diameter of nanowires. Specifically, the decomposition of GaN nanowires is studied and discussed in detail in this chapter. Our results indicated that the decomposition of GaN nanowires leads to a

uniform reduction in their diameter and results in the formation of quantum wires. It is also the aim of the chapter to understand the mechanism behind the uniform and controlled decomposition of GaN nanowires, along with the factors affecting the rates of decomposition of GaN. Based on the results, a layer-by-layer decomposition model is proposed to explain the uniform thinning of the GaN nanowire diameters all along their lengths. This layer-by-layer decomposition is a direct result of the ballistic diffusion of gallium adatoms, observed exclusively on nanoscale surfaces. Ballistic diffusion is intended to mean that the diffusion lengths are very large, on the order of tens of microns, in this chapter. A final aim of the chapter is to understand the variation in the optical bandgap of the nanowires with diameter. The bandgap of GaN nanowires was observed to increase with decreasing diameter. A blue-shift in the bandgap of GaN, as much as 0.5 eV, was observed. To our knowledge, no such studies indicating the use of post-synthesis decomposition as a strategy for uniformly reducing the diameter of nanowires currently exist in the literature.

Decomposition Methods

Experiments for the decomposition of GaN nanowires were performed by placing the pre-synthesized GaN nanowires on the heater and heating them to an elevated temperature of 900 ^{o}C. These experiments were performed both in the presence of only ammonia and only hydrogen in the gas phase for varying durations ranging from 1 to 10 minutes. The as-obtained nanowires and the quantum wires obtained by their decomposition were characterized using scanning electron microscopy (SEM), X-ray

diffraction (XRD), transmission electron microscopy (TEM), and ultraviolet-visible absorption (UV-Vis) spectroscopy. As-obtained GaN nanowires and quantum wires were used for the SEM and UV-Vis analysis, without any sample preparation. Samples for TEM analysis were prepared by simply scraping the nanowires onto holey-carbon coated copper TEM grids.

Results

This section encompasses the results of the synthesis of the GaN nanowires, the decomposition, and the unique properties resulting from the uniform reduction of the diameters of the gallium nitride nanowires.

Nanowire Synthesis

The reactive vapor transport of gallium in the presence of decomposed ammonia proceeded as expected and led to the formation of GaN nanowires.[86, 88] The as-obtained nanowires (Figure 3a) had an average diameter of 23 nm and are tens of microns long. XRD analysis of the GaN nanowires sample (Figure 3b) indicated that the obtained nanowires have a wurtzite crystal structure with lattice parameters of a=3.19 Å and c=5.17 Å.[80]

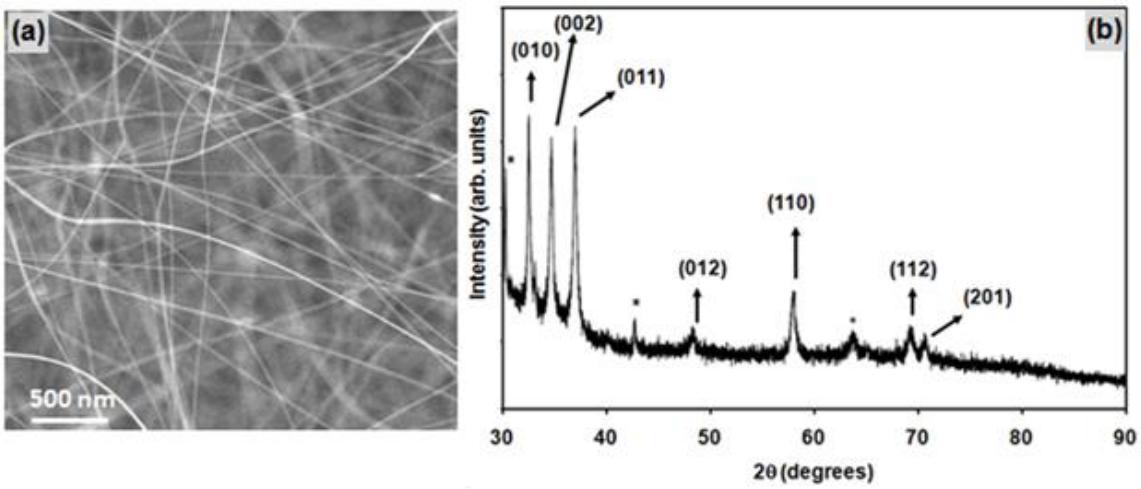

Figure 3. (a) Scanning electron micrograph of the as-synthesized GaN nanowires obtained by the reactive vapor transport approach. (b) XRD analysis of the nanowires indicating their wurtzite structure.

Nanowire Diameter Reduction

Decomposition of the as-obtained GaN nanowires was performed in the presence of ammonia in a sequential manner for durations of 3, 6 and 10 minutes. After each decomposition experimental step, the nanowires were characterized using SEM and TEM to understand the effect of high temperature decomposition on their morphology and size. Representative TEM micrographs of the 23 nm diameter as-synthesized nanowires, the 6.8 nm diameter nanowires resulting from their decomposition for 6 minutes, and the 4.8 nm diameter nanowires resulting from their decomposition for 10 minutes in the presence of NH_3 are respectively shown in Figure 4a, b and c. From the Figure 4a-c, it can also be observed that the reduction in the diameters of the nanowires is uniform all along their lengths.

HR-TEM analysis of the nanowires indicated that the as-obtained nanowires are single-crystalline in nature (Figure 4d). The lattice spacing in the growth direction was observed to be 2.76 Å and indicated that they preferentially grew in the [100] growth direction (Figure 4d).[86] HR-TEM analysis also indicated that the growth direction of the nanowires remained unaltered during the decomposition process, and remained [100] (Figure 4e). No change in the growth direction of the wires is indicative of the fact that the nanowires undergo a partial decomposition, leading to a uniform reduction in the wire diameters. If this process occurred via complete decomposition, followed by regrowth of the nanowires, then there would be a change in the growth direction of the nanowires from [100] to [001].[86]

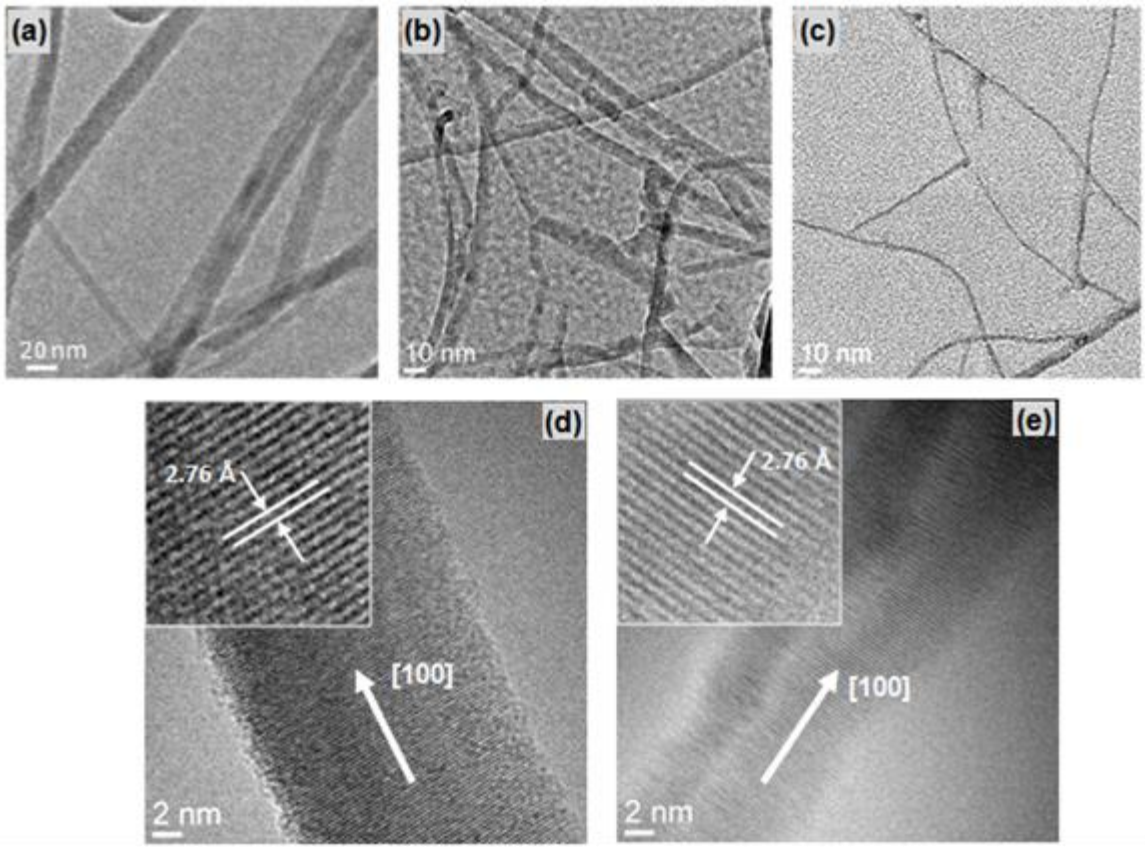

Figure 4. Transmission electron micrographs of (a) as-obtained GaN nanowires and nanowires observed after (b) 6 minutes and (c) 10 minutes of decomposition in NH_3. HR-TEM images of (d) an as-obtained nanowire and (e) a 3.2 nm GaN nanowire after decomposition indicating that the crystal structure and growth direction did not change.

Decomposition Mechanism and Kinetics

A plot showing the variation in the mean diameter of the nanowires with decomposition time is shown in Figure 5. It is essential to mention here that for each sample, the diameters of 25-50 nanowires were taken as a sample data set and measured for the determination of their mean diameter. The error in the measurement is no more than ± 0.5 nm. The diameter distributions of the as-synthesized nanowires, and nanowires decomposed for 3, 6 and 10 minutes are shown in the inset to Figure 5. The

mean diameter of the nanowires was found to decrease exponentially with decomposition time as shown in Figure 5 and Equation 1.

$$D = D_o e^{-kt} \tag{1}$$

From Equation 1, the decomposition rate (nm/min) can be determined to be

$$\frac{dD}{dt} = -kD_o e^{-kt} = -kD \tag{2}$$

where, D is the mean diameter of the nanowires (nm) at time t (min), D_o is the initial diameter of the nanowires, and k is a decomposition rate constant. This exponential rate of decomposition is proportional to the circumference (πD) due to monolayer step creation being the rate determining step. The decomposition rate constant is dependent on the experimental conditions employed: decomposition temperature, pressure and gas phase composition. From the plot in Figure 5, the value of k is determined to be 0.156 min^{-1} under our experimental conditions. This implies that duration of 4.44 minutes is required for halving the diameter of the nanowires. The rate of decomposition depends on the initial diameter of the nanowire, and is observed to have a maximum of 3.28 nm/min and an average of 1.66 nm/min. The maximum and average decomposition rates correspond to 13.12 and 6.64 monolayers per minute, respectively, assuming a thickness of 0.25 nm for one monolayer of GaN.[142] The rate of decomposition of GaN nanowires is observed to be higher than that of bulk GaN crystals. In a previous study, Grandjean *et al*. studied the decomposition of bulk GaN in the presence of an ammonia flux.[143] Using the correlation presented, the decomposition of bulk GaN under our experimental conditions (850 ^oC and 100 mTorr) was determined to be 0.36 nm /min. Assuming again

a thickness of 0.25 nm per monolayer for GaN,[142] the bulk decomposition of GaN was estimated to be 1.44 monolayers per minute. From the above analysis, the decomposition rate of bulk GaN is estimated to be approximately one-tenth of the maximum decomposition rate and one-fifth of the average decomposition rate of GaN nanowires observed in our experiments. It was also observed that the diameter distribution of the wires was reduced as the decomposition proceeded (Figure 5), resulting in a much more narrow distribution in the decomposed wires than was found in the as-synthesized nanowires.

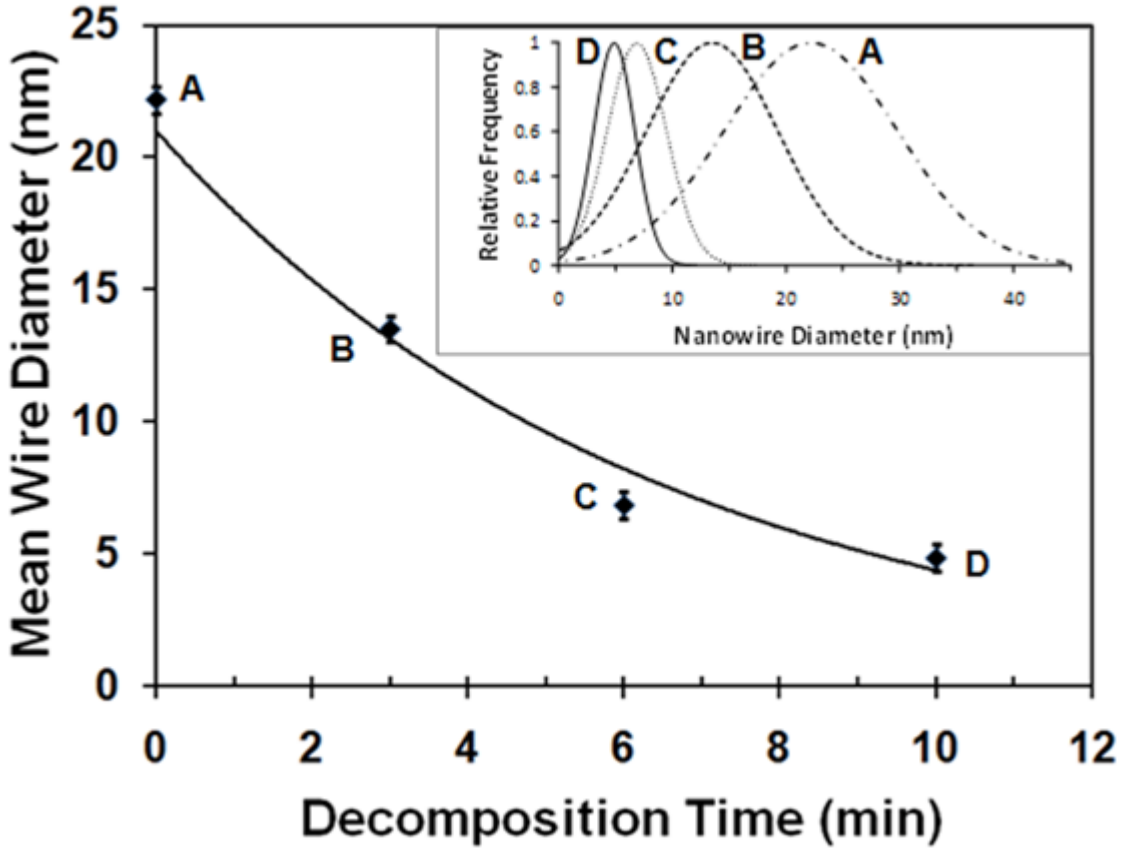

Figure 5. A plot showing the variation in the mean diameter of the GaN nanowires with decomposition time in the presence of ammonia at a temperature of 900 ºC. The mean nanowire diameter is observed to decrease exponentially with time. The error in the measurement is estimated to be ±0.5 nm. The histogram insert shows the diameter distribution of the GaN nanowires at various times.

Experiments performed to understand the effect of gas phase chemistry on decomposition of GaN indicated that the rate of decomposition of GaN nanowires is higher in the presence of hydrogen than in the presence of ammonia. These experiments were performed at a temperature of 900 ºC, a pressure of 100 mTorr, and under a hydrogen flow rate of 100 sccm. In the presence of hydrogen, the complete decomposition of GaN nanowires (23 nm in diameter) into gallium was observed after

duration of only 6 minutes (Figure 6). It is essential to recall here that in the presence of ammonia 4.8 nm thin quantum wires were observed after 10 minutes of decomposition.

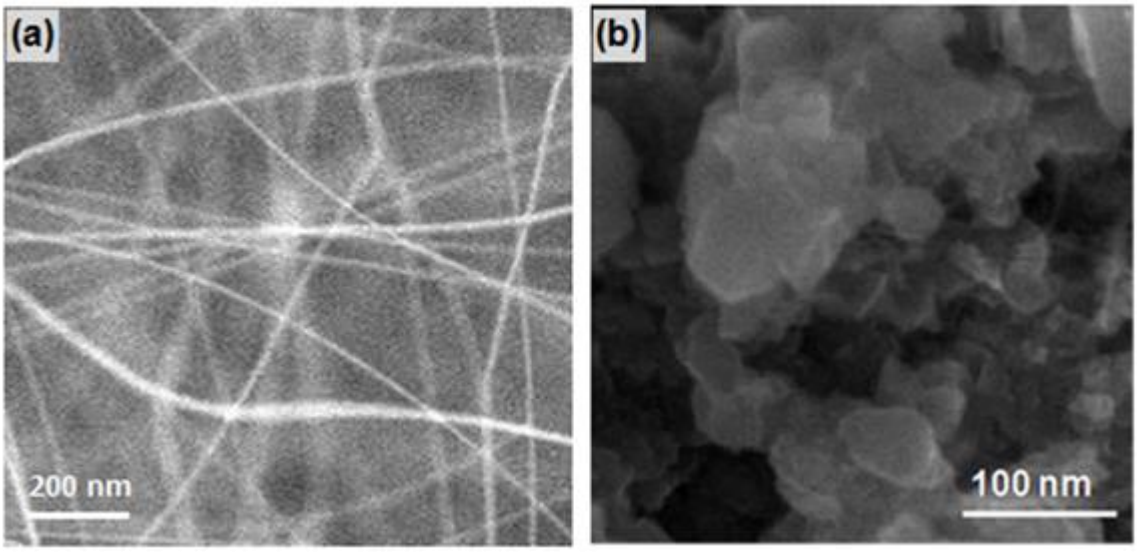

Figure 6. (a) Scanning electron micrograph of as-synthesized GaN nanowires. (b) Micrograph of polycrystalline GaN resulting from the decomposition of GaN nanowies for 6 minutes in the presence of hydrogen.

In order to understand whether the uniform reduction in the diameters of the nanowires is exclusive to nanoscale, the decomposition of bulk compound semiconductor wafers was also studied. Owing to the lack of single-crystal GaN wafers, these experiments were performed using GaAs wafers. As expected, the decomposition of a GaAs wafer led to the formation of etch pits along its surface (Figure 7). Similar behavior was previously observed and reported in GaN crystals by Pisch *et al.*[144]

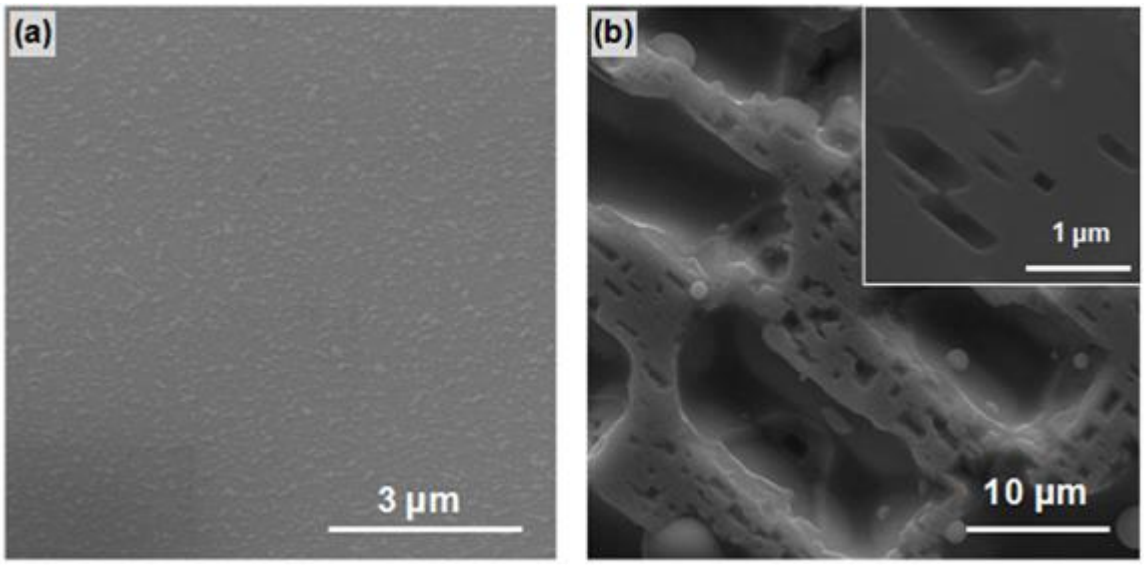

Figure 7. Scanning electron micrographs of a (100) oriented GaAs wafer surface, (a) before and (b) after thermal decomposition. The formation of etch pits upon decomposition is clearly observed in the images shown in (b).

In principle, the partial decomposition of GaN nanowires may follow three routes: (a) layer-by-layer decomposition if the diffusion of both decomposed Ga and N species can be fast over the length scales of nanowires, (b) creation of multiple etch steps and coalescence to remove a monolayer eventually leading to rough surfaces of the decomposed nanowires, and (c) creation of etch pits in nanowires ultimately leading to the breakdown of nanowires into individual crystals. The mode of decomposition is dependent on the gallium adatom diffusion lengths on the surfaces of GaN. If the diffusion lengths of gallium adatoms is ballistic, layer-by-layer decomposition on the surfaces of the nanowires occurs and leads to a uniform reduction in their diameters without changing their growth direction (Figure 8a and b). If the diffusion lengths of adatoms are smaller, then gallium droplets are formed all along the lengths of the

nanowires. The accelerated etching of GaN in the vicinity of the droplet breaks the nanowires into multiple crystals (Figure 8c). This leads to the formation of polycrystalline GaN.

The diffusion lengths of gallium adatoms on the surfaces of bulk GaN crystals are well known to be in the range of 10-80 nm.[145] Similarly, the diffusion lengths of gallium on GaAs crystal surfaces are also in the 10-100 nm range.[146] It is also documented that gallium droplets aid in accelerating the decomposition in their vicinity.[144] Hence, in the case of bulk crystals, the primary result of decomposition is the formation of etch pits all along the surfaces. These etch pits eventually break bulk crystals into a polycrystalline crust. Similar decomposition phenomena occur in thick nanowires (Figure 8c). In the case of thinner (sub-25 nm diameter) nanowires, ballistic diffusion of metal adatoms on the surfaces can occur with diffusion lengths on the order of tens of microns.[86, 147] Therefore, the formation of gallium droplets on the surfaces of nanowires does not occur unless desorption of gallium adatoms proceeds slowly to allow its accumulation on the nanowire surface. Thus, layer-by-layer decomposition leads to the uniform shrinking of the nanowires diameters.

In the case of layer-by-layer decomposition of nanowires, the monolayer etch rate can depend upon either the surface area of the nanowire or the circumference of the nanowire. In the case of slower kinetics, in the presence of ammonia, the rate of monolayer etching is limited by etch step creation which is proportional to the number of edge sites (or the circumference $\propto \pi D$). In this case, the decomposition is initiated at the edge of the nanowire and the step propagation occurs much faster than the next etch step

creation as seen in Figure 8a. In order for this mechanism to be operative, the gallium adatoms, resulting from the decomposition of GaN, diffuse away from the step edge and desorb quickly from the surface of the nanowire. Under these conditions, one can model the rate of monolayer etching as that proportional to the monolayer etch step creation, the rate determining step. In other words, the rate of monolayer etching is proportional to the diameter (or the circumference) of the nanowires and a rate constant as shown in Equation 2. Because the rate of decomposition is directly proportional to the diameter of the wire, larger nanowires (with larger circumferences) decompose faster than smaller nanowires. Consequently, the diameter distribution is expected to be narrowed as the decomposition proceeds. The above model is consistent with the experimental observations shown in Figure 5.

In the presence of hydrogen, the activation energy of nitrogen desorption can be reduced leading to multiple etch step creation along the length of nanowires instead of primarily at the edges as illustrated in Figure 8b. In this case, the time required for the complete decomposition of a GaN surface layer depends primarily on the etch step propagation and coalescence time and is consequently not limited by the etch step creation time. Therefore, the rate of decomposition of GaN nanowires is higher in the presence of hydrogen than in the presence of ammonia. In sharp contrast, the diffusion lengths of adatoms on bulk GaN crystal/thick GaN nanowires surfaces is smaller (10-80 nm).[145] These lower diffusion lengths of gallium adatoms lead to their accumulation and the formation of droplets all along the surface of the nanowire/crystal. The accelerated

etching of GaN [144] in the vicinity of the droplet essentially breaks a nanowire into multiple crystals (Figure 8c).

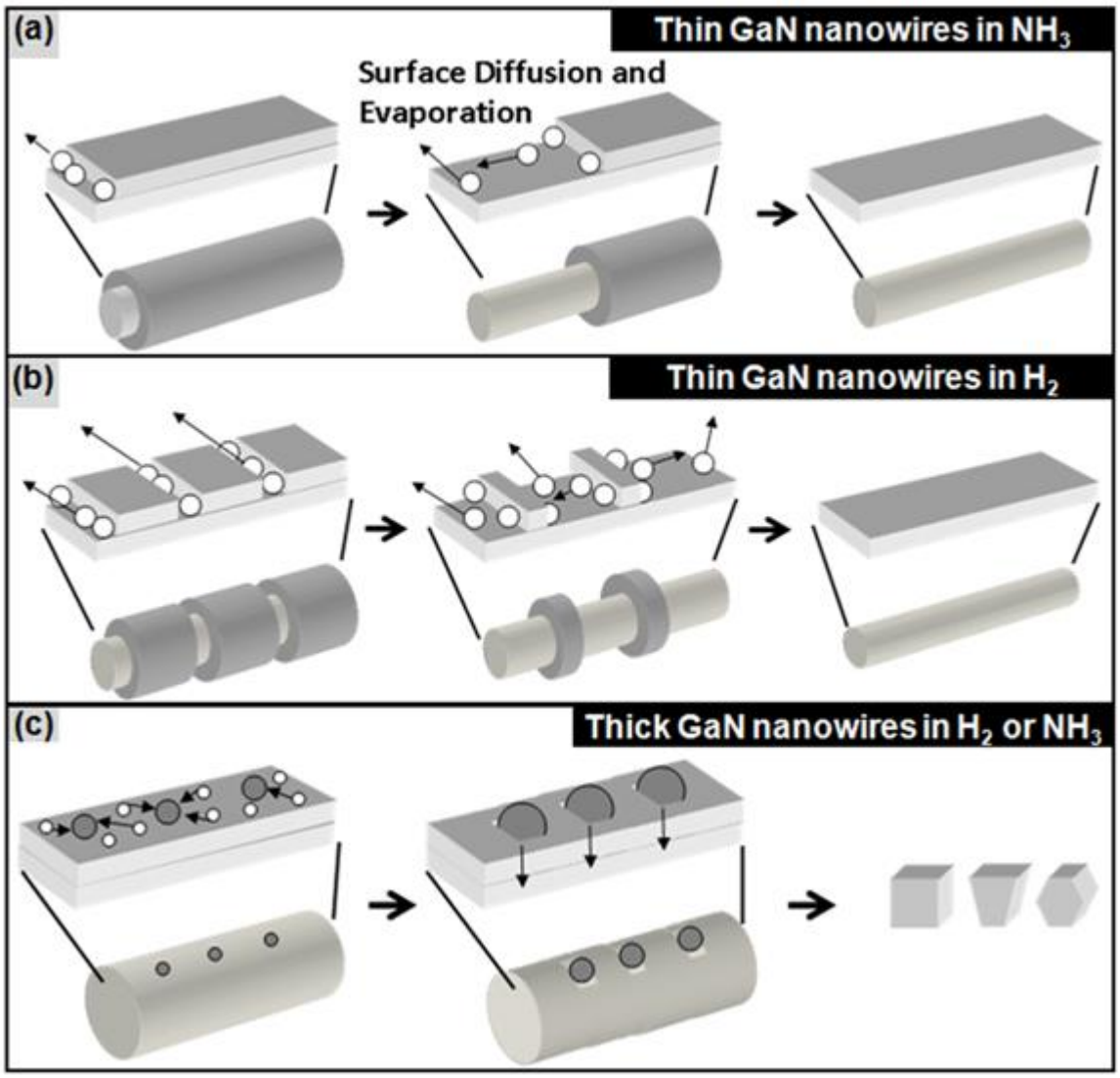

Figure 8. (a) A schematic illustrating the proposed mechanism of decomposition in thin GaN nanowires (diameters less than 25 nm) in the presence of (a) NH_3, and (b) H_2. (c) Mechanism of decomposition expected in thick GaN nanowires/bulk GaN crystals.

In situ TEM Decomposition

Decomposition of GaN nanowires was also performed inside a TEM (FEI Technai F20) equipped with a heating stage. These experiments were performed in vacuum at 10^{-7} Torr, without the supply of a nitrogen containing gas, such as ammonia. The decomposition of GaN nanowires in the absence of ammonia was observed to be similar to that expected in bulk GaN. During this process, voids begin to form in nanowires as the result of nitrogen evaporation and nitrogen vacancies accumulation (as indicated by the white arrows in Figure 9a). Simultaneously, the gallium resulting from the decomposition of GaN accumulated into droplets. The preferential decomposition of GaN in the vicinity of the gallium droplets leads to the formation of holes (Figure 9b). It is documented that in the presence of a nitrogen containing gas, the activation energy of nitrogen desorption is increased;[143] consequently, the amount of free gallium on the surface of the GaN nanowires is insufficient to accumulate into droplets. Therefore, controlled decomposition in the presence of ammonia is essential for uniformly thinning GaN nanowires. In contrast, the lower nitrogen desorption activation energy in absence of ammonia leads to the accumulation of gallium in the form of droplets, and hence the formation of etch pits in GaN nanowires. Additional experimentation on the *in-situ* decomposition of GaN nanowires inside a TEM are currently being performed, and will be reported later.

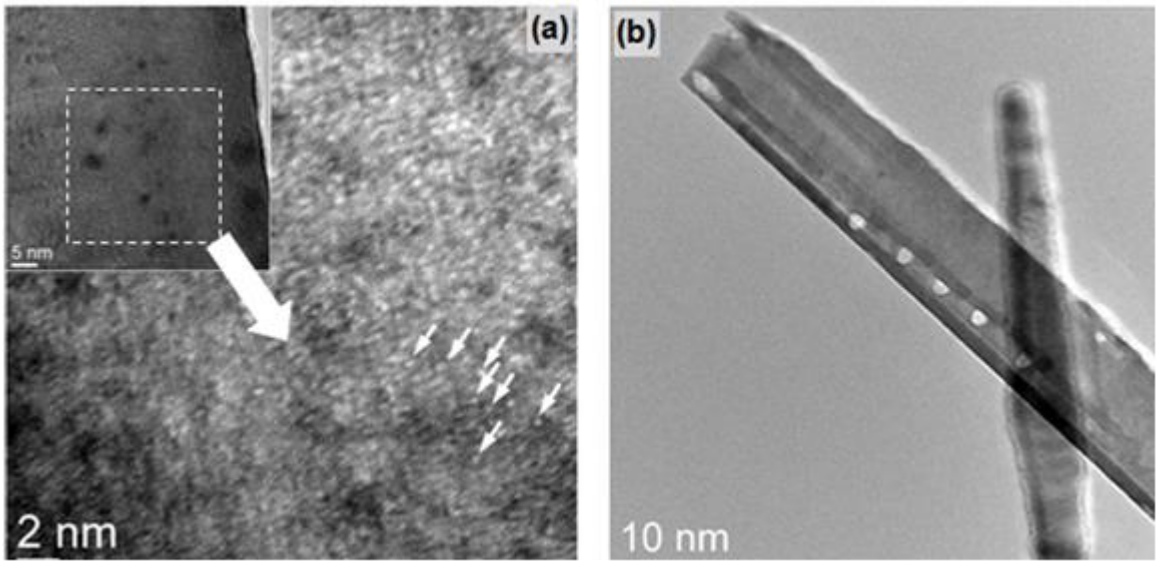

Figure 9. Micrographs of a GaN nanowire during decomposition as observed *in-situ* inside a transmission electron microscope equipped with a heating stage. (a) Voids formed due to nitrogen vacancies accumulation during the decomposition of the GaN nanowire (indicated by white arrows). The gallium adatoms resulting from the decomposition accumulate into gallium droplets. Preferential etching of the GaN in the vicinity of the droplets leads to the formation of holes within the GaN nanowires, as shown in (b). The *in-situ* decomposition experiments were performed in the absence of ammonia, and decomposition phenomenon observed is similar to that expected in bulk GaN crystals**.**

Bandgap Blue-Shift

In order to estimate the effect of diameter on the bandgap of GaN, UV-Vis absorption spectroscopic analysis of the as-synthesized GaN nanowires and the quantum wires resulting from their decomposition was performed. As-obtained nanowires and quantum wires on quartz substrates were directly employed for this purpose, without any additional sample preparation. A Tauc plot was also generated from the transmittance (T) vs. energy ($h\nu$) data obtained using UV-Vis spectroscopy (Figure 10).[140, 148] The Tauc relation is given by $\alpha h\nu = B\left(h\nu - E_g\right)^X$ where α is the absorption coefficient, h is

Planck's constant, v is the frequency of the incident wave, and B is a constant. The factor x is 0.5 for direct bandgap semiconductors (such as GaN) and 2 for indirect bandgap semiconductors. The absorption coefficient (α) was calculated from the transmittance (T) vs. energy (hv) data using the procedure described previously.[148-150]

The Tauc plot of GaN nanowires and quantum wires, showing the variation of $(\alpha hv)^2$ with energy (hv), is shown in Figure 10. The optical bandgap can be determined by the x-intercept of a tangent drawn through the linear portion of the plot. This technique confirmed that the bandgap of the as-synthesized 23 nm GaN wires is 3.4 eV.[92-94] The Tauc plot also indicated that the bandgaps of GaN nanowires with average diameters of 13.5 nm, 6.8 nm and 4.8 nm are respectively 3.4, 3.7 and 3.9 eV. A plot showing the variation of the bandgap of GaN with nanowire diameter is shown in the inset to Figure 10. As expected, the reduction in the diameter of GaN nanowires led to an increase in the bandgap.[92] A maximum blue-shift of 0.5 eV in the bandgap of GaN was observed in nanowires with an average diameter of 4.8 nm. The bandgaps estimated from the Tauc plots were observed to be close to those predicted by theoretical estimates.[94] For example, theoretical estimates predict a blue-shift of 0.5 eV is expected in GaN crystals with sizes of 4 nm.[92, 94] The average diameter of our nanowires observed from SEM and TEM analysis exhibiting a bandgap of 3.9 eV was observed to be 4.8 nm, close to that predicted by theory.

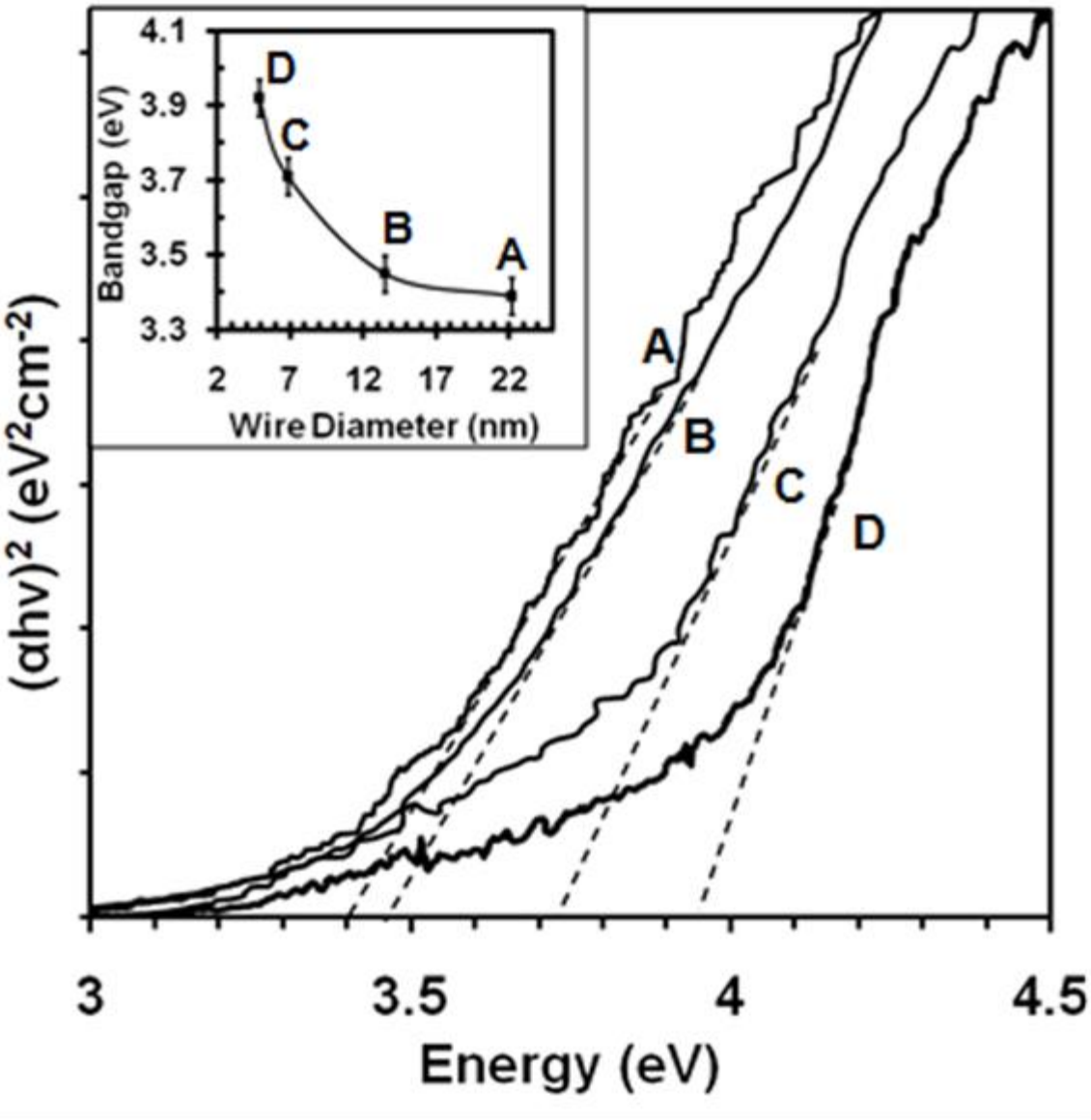

Figure 10. Tauc plots of (A) as-obtained GaN nanowires, nanowires observed after decomposition in NH_3 for (B) 3 minutes, (C) 6 minutes, and (D) 10 minutes showing a 0.5 eV blue-shift in the bandgap as the diameter was decreased from 23 nm to 4.8 nm. The insert shows the variation in the bandgap of GaN nanowires as a function of their average diameters.

Conclusion

In conclusion, a simple post-synthesis strategy for uniformly reducing the diameters of pre-synthesized nanowires and obtaining quantum wires is presented. The decomposition occurred in a layer-by-layer fashion in nanowires with sizes less than 25 nm and led to the formation of quantum wires with diameters as small as 4.8 nm on average. This layer-by-layer decomposition is a result of the ballistic diffusion of gallium adatoms (resulting from the decomposition of GaN) on GaN nanowire surfaces. Layer-by-layer decomposition is exclusive to GaN nanowires with diameters less than 50 nm and unlike that of bulk GaN crystals where decomposition leads to the formation of etch pits all along the surfaces. The rate of decomposition was also observed to be dependent on the gas phase chemistry, lower in the presence of ammonia and higher in the presence of hydrogen. A reduction in the diameter of the GaN nanowires resulted in an increase in their optical bandgap. A blue-shift in the bandgap of 0.5 eV is observed in the obtained GaN quantum wires with a mean diameter of 4.8 nm. This shift is attributed to quantum confinement resulting from the diameter reduction of the nanowires. This post-synthesis decomposition strategy for reducing the diameters of nanowires is expected to be applicable to other III-V compound semiconductor systems.

CHAPTER V

POST-SYNTHESIS NANOTUBE FORMATION

Introduction

Nanotube morphology has been shown to be a viable option for photovoltaic[19] and photocatalytic[151] cells. The absorption cross-section per unit volume of nanowires has been shown to be eight times that of nanoparticles,[152] and charge transfer in the photoactive layer has been demonstrated to be enhanced by using nanowire morphology.[38] Nanotubes have the same high external absorption area as nanowires, but also have smaller minority carrier radial diffusion distances,[6] and their performance as photoabsorbers should be enhanced relative to nanowires with the same external diameter.

State-of-the-art synthesis techniques for non-carbon nanotubes include various strategies involving anodic alumina (AAO) templates and oxide nanowire templates. AAO has been previously used to synthesize polycrystalline $LiMn_2O_4$ and $LiCoO_2$ using thermal decomposition of sol-gel precursors,[153] polycrystalline noble metal nanotubes using electroplating,[154] and various polycrystalline semiconducting oxides using sol-gel chemistry.[40] The "epitaxial casting" strategy has also been utilized to synthesize single-crystalline GaN nanotubes using ZnO nanowires as templates.[155] Also, α-Fe_2O_3,[1, 156] TiO2,[4] and Ta_2O_5[5] nanotubes have been created without the use of a template using electrochemical methods, but all nanotube synthesis techniques involving electrochemistry typically result in polycrystalline material.[7] To the best of the author's

knowledge, no template free method has previously been used to create single-crystalline non-carbon nanotubes. In this context, the template-free synthesis of single-crystalline nanotubes is presented via a reverse VLS decomposition mechanism. Zinc phosphide (Zn_3P_2), a p-type semiconductor with a bandgap of 1.5 eV, useful for the fabrication of photovoltaic cells,[28] will be used as an example system for this nanotube formation. The comprising elements of Zn_3P_2 are also earth abundant[29] and relatively inexpensive.

Decomposition Methods

The zinc phosphide nanowires were synthesized using the small scale synthesis technique as stated in Chapter II. After 30 minutes, the source heat is terminated, and the nanowires are allowed to sit for 30 minutes at 600 °C to controllably decompose into nanotubes.

The nanotubes were characterized for morphology, crystal structure, and chemical composition using scanning electron microscopy (SEM), transmission electron microscopy (TEM), scanning transmission electron microscopy (STEM), and energy disperse spectroscopy (EDS).

Results

This section contains all of the characterization of the nanowires, a proposed mechanism for their formation, and thermodynamic calculations to confirm that the mechanism is feasible.

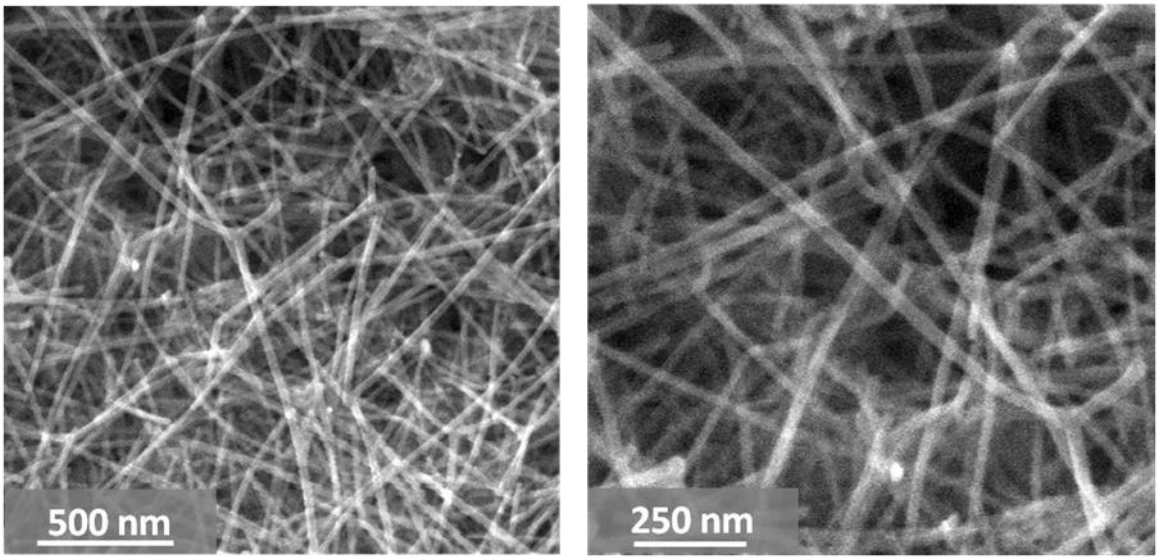

Figure 11. Scanning electron micrographs of Zn_3P_2 nanotubes formed after thermal decomposition of Zn_3P_2 nanowires with diameters of 40-50 nm and lengths of tens of microns.

Nanotube Characterization

SEM images in Figure 11 confirm the existence of nanotubes with diameters that range from 40 to 50 nm and lengths in excess of 10 microns, similar to the Zn_3P_2 nanowires previously reported using this technique.[11] Dark field STEM images are indicative that the formation of the nanotubes is initiated at the tip of the wire (Figure 12a). As time progresses, the amount of nanowire core is etched further from the tip (Figure 12b), and by the end of the experiment, the entirety of the wire has been transformed into a tube. High resolution TEM images illustrate that the walls of the nanotubes are single crystalline (Figure 12c), and selected area electron diffraction (SAED) of the wall of the nanotube also confirmed the single-crystalline structure as can be seen in Figure 12d. The lattice spacings are consistent with those reported previously for Zn_3P_2.[11]

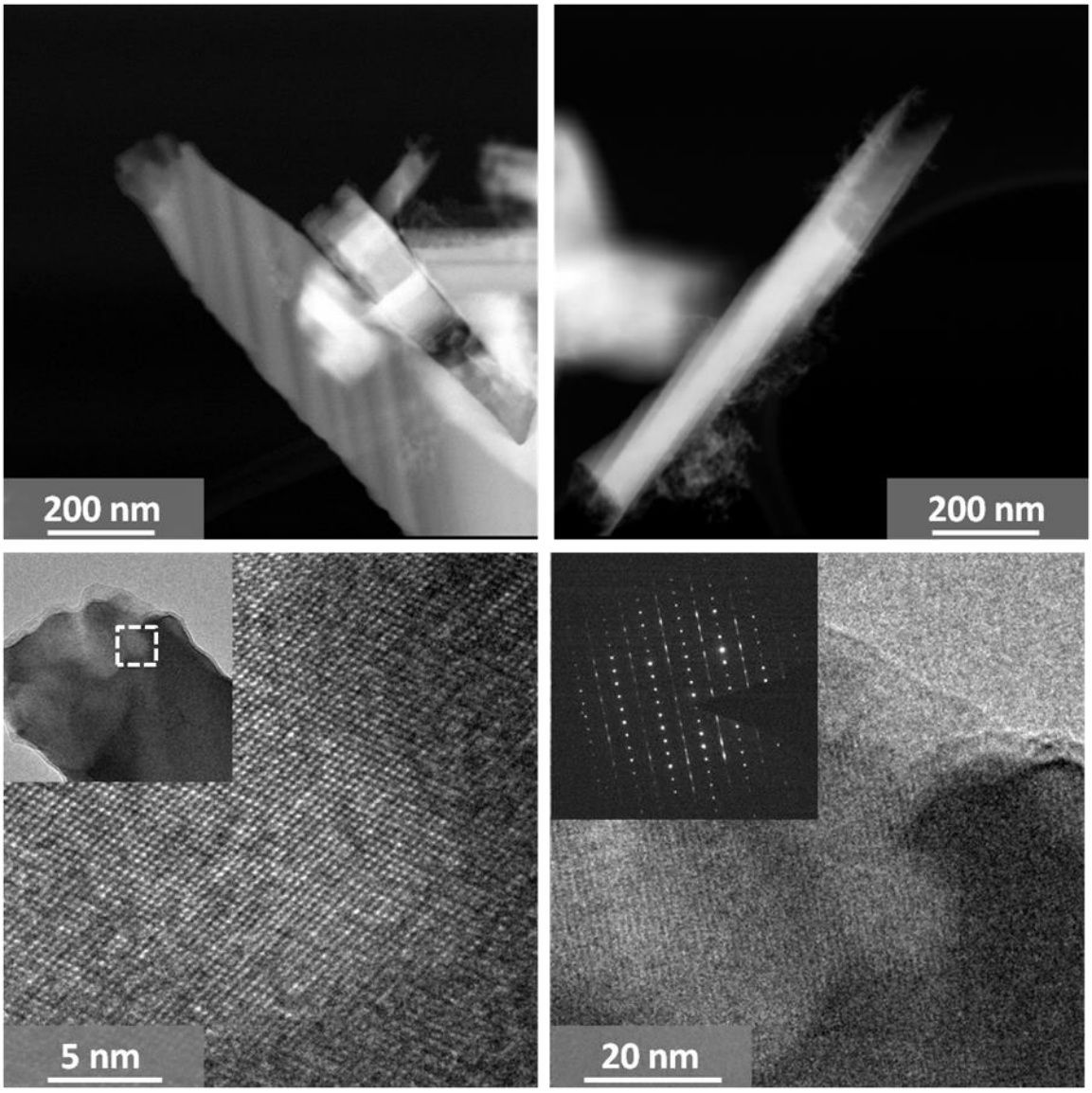

Figure 12. Dark field scanning transmission electron micrograph of (a) the initial stages Zn_3P_2 nanotube formation and (b) further progression of the decomposition and tube formation. (c) High resolution bright field transmission electron micrograph of the same wire as in (a) with the inset showing the area of the single-crystalline tube wall imaged and (d) a transmission electron micrograph and SAED of the nanotube further showing a single-crystalline wall.

Additionally, EDS analysis of the nanotubes confirms a uniform ratio of zinc to phosphorus across the diameter of the tube and a decrease in signal intensity in the center of the wire signifies its hollow structure (Figure 13). This is consistent with the idea that Zn_3P_2 decomposes congruently, as reported previously.

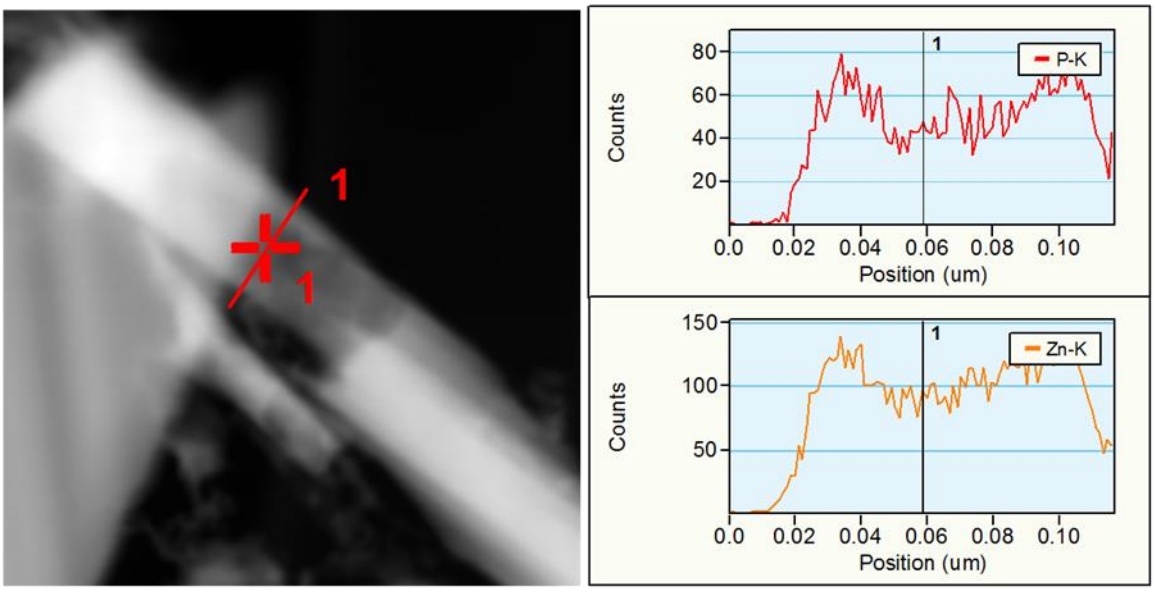

Figure 13. Energy dispersive spectrograph line profiles of Zn_3P_2 nanotubes indicating the tubes are hollow with uniform zinc to phosphorus ratio across the diameter of the tube.

Decomposition Mechanism

The mechanism believed to be responsible is the etching or "drilling" of the nanowires by the zinc droplet formed on the tip of the wire during vapor-liquid-solid (VLS) growth. Due to the termination of the source zinc phosphide, the equilibrium in Equation 3 shifts back to the left (i.e. nanowire decomposition) via Le Châtelier's principle. A schematic of this principle can be seen in Figure 14.

$$3Zn + \frac{1}{2}P_4 \underset{600\,^{\circ}C}{\Longleftrightarrow} Zn_3P_2 \qquad (3)$$

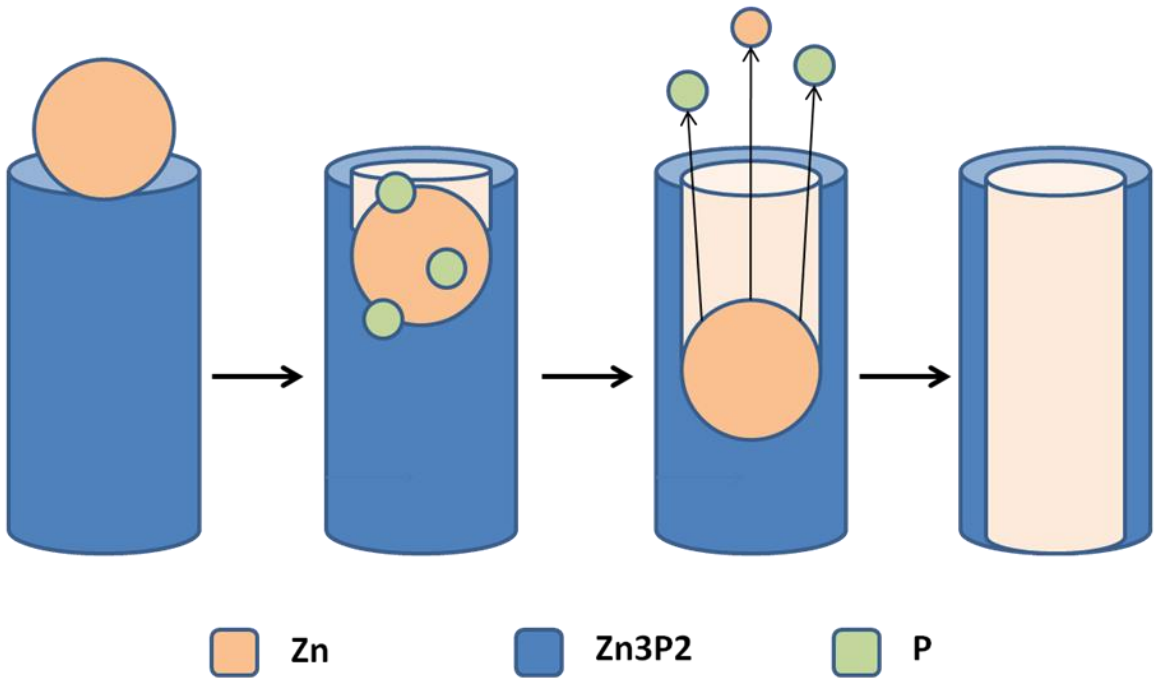

Figure 14. Schematic of the proposed solid-liquid-vapor (SLV) nanowire decomposition mechanism.

The most kinetically favorable pathway of decomposition is for the zinc phosphide to dissolve into the droplet, dissociate, and then evaporate, similar to the accelerated etching in the presence of metal droplets on bulk semiconductor surfaces.[144] This is essentially a solid-liquid-vapor (SLV), reverse VLS, mechanism in which the droplet is lowered through the nanowire forming the nanotubes. The observed hollowing of the single-crystalline nanowires results in single-crystalline nanotubes. The key to translate this mechanism into other material systems with uniform wall thicknesses is to determine the decomposition temperature and pressure that allows for the nanowire material to dissolve into the catalytic droplet at the same rate as it vaporizes. Due to the slow congruent decomposition rate of zinc phosphide at the reactor conditions of 1 Torr and 600 °C, the zinc formed from the decomposition on all surfaces but the droplet existing on the tip of the wire will vaporize before the critical droplet size can form. Likewise, the reasoning for the incomplete decomposition of some of the tubes is due to the zinc droplet evaporating faster than it can be replenished with the zinc from the zinc phosphide decomposition. Previous reports state that under similar decomposition conditions as presented in this work, the zinc droplet is replenished at a rate 1 order of magnitude more slowly than it vaporizes from the decomposition of Zn_3P_2.[44]

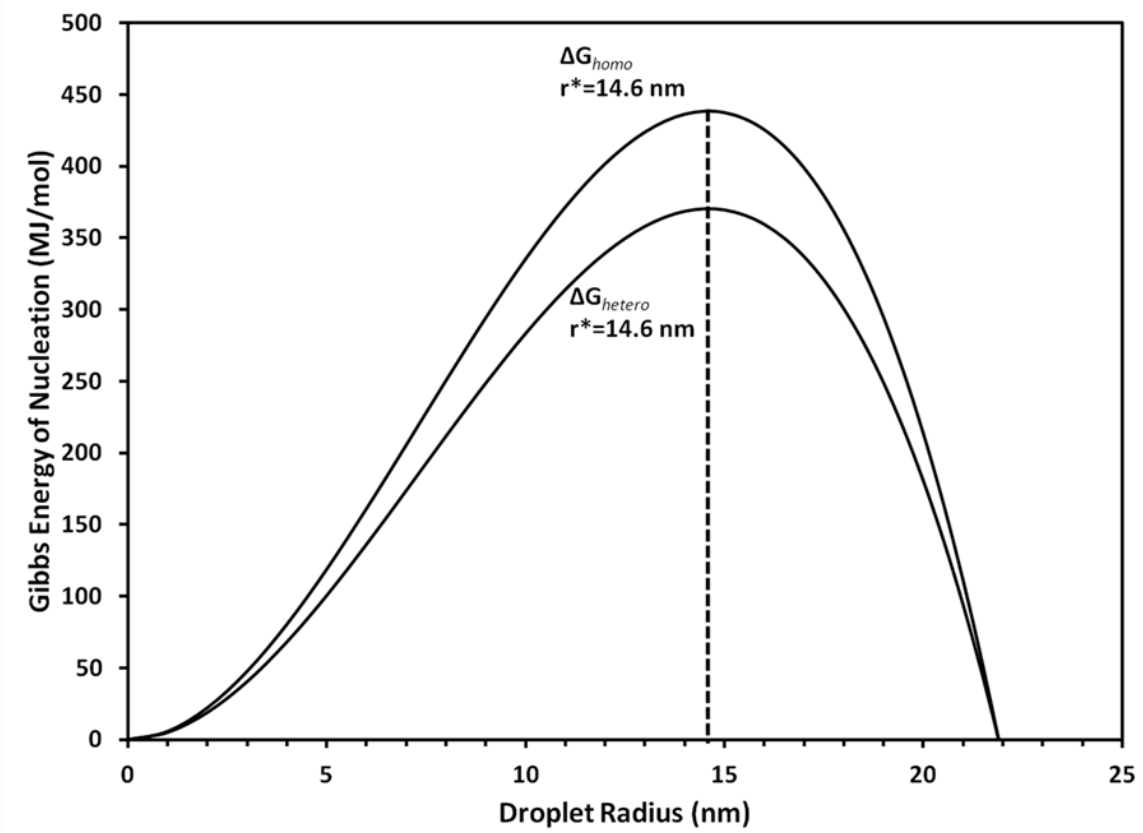

Figure 15. A plot of Gibbs energy of nucleation versus critical droplet radius demonstrating the minimum droplet size that can form under our reaction conditions (r*=14.6 nm), and consequently; the minimum tube external diameter that can be formed.

Thermodynamic Limitations

There are also limitations on the tube external diameter based on the critical radius of droplet formation at the desired decomposition conditions. For the Zn_3P_2 nanowire system catalyzed by zinc droplets at 600 °C and 1 Torr, the minimum droplet diameter that can form is 29 nm (Figure 15) as calculated by the change in the Gibbs free energy for nucleation. The changes in the Gibbs free energy of homogeneous and heterogeneous nucleation from the vapor phase were calculated as shown previously.[50]

The contact angle of zinc on zinc phosphide is unavailable in the literature; consequently the contact angle value of 122° for zinc on zinc oxide[51] was used instead for the calculation of heterogeneous nucleation energy. Any nanowire which has surfaces smaller than this critical diameter will not have droplets on any of its surfaces, and consequently, cannot form nanotubes. The decomposition of these smaller nanowires will result in a uniform reduction in the diameter of the nanowires via the ballistic diffusion of adatoms, as has been shown previously.[10] Also if the wire is too large, droplets will form on all surfaces of the nanowire resulting in the accelerated etching or "drilling" effect occurring on all surfaces of the nanowire, resulting in porous structures. Scanning electron micrographs of the quantum wires and porous nanowires can be seen in the supplementary information Figure 16. Furthermore, the high energies of nucleation determined from the calculations can be justified by the vapor pressure of zinc being an order of magnitude higher than its boiling point at a reactor pressure of 1 Torr.

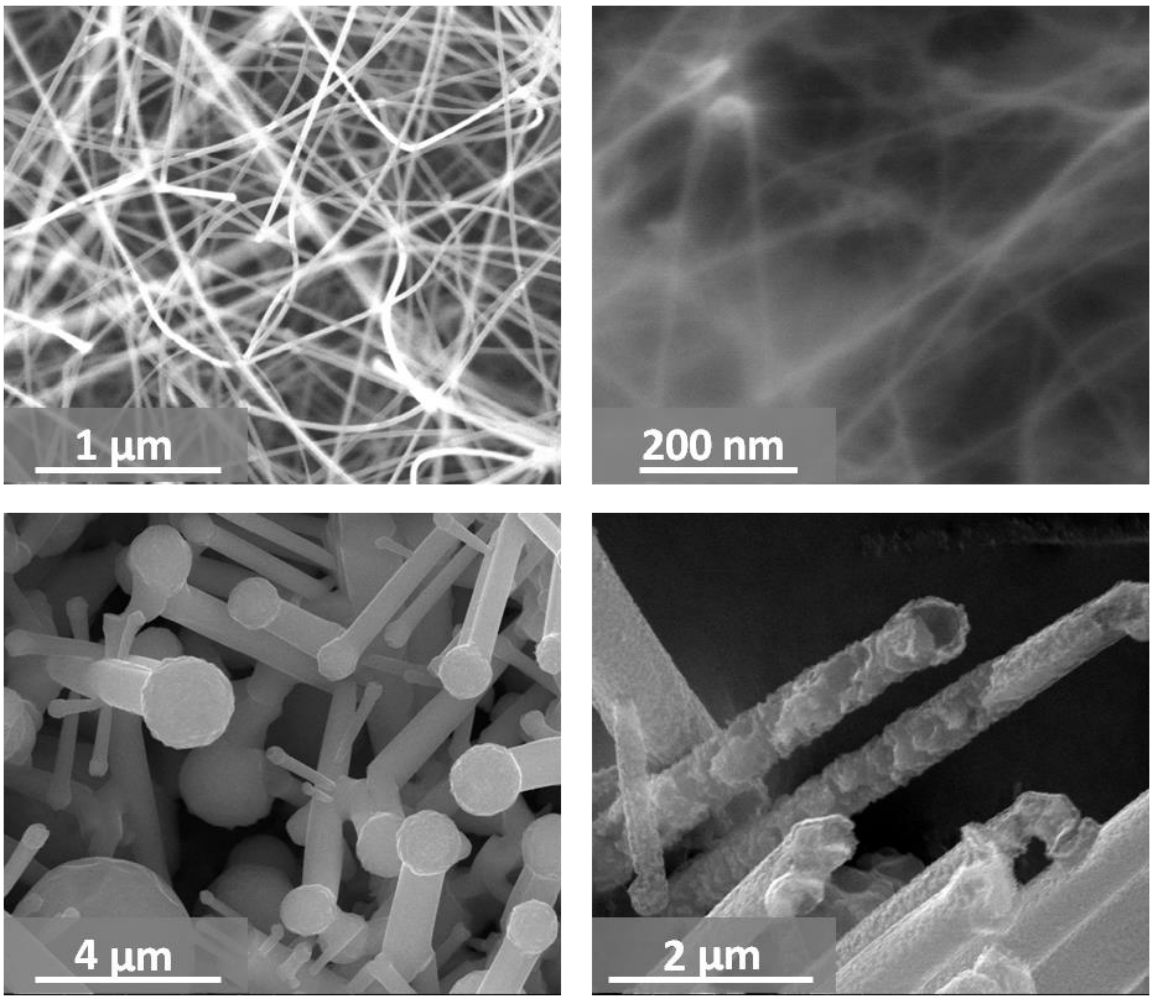

Figure 16. Nanowires small enough that droplets cannot form result in quantum wires upon their decomposition are shown (a) before and (b) after their decomposition. Very large nanowires where droplets can form on all surfaces result in porous nanowires after decomposition are shown (c) before and (d) after their decomposition.

Conclusions

Single-crystalline zinc phosphide nanotubes were synthesized using a reverse VLS decomposition mechanism after the synthesis of single-crystalline nanowires. This mechanism is believed to be a viable route for the nanotube synthesis of any material

system which nanowires can be grown by the VLS mechanism providing the catalyst droplet is energetically favorable at the decomposition conditions.

CHAPTER VI

NANOWIRE SURFACE PASSIVATION*

Introduction

The aim of this chapter is to demonstrate that the large-scale synthesis of Zn_3P_2 and Zn_4Sb_3 nanowire powders can be accomplished without the aid of any external templates and catalysts, and that *in-situ* vapor-phase functionalization, a one-step process involving the exposure of nanowires to a vapor of organic functional molecules immediately after their synthesis, can be utilized to enhance the surface stability of nanowires against air- and moisture-assisted degradation.

In-situ vapor phase functionalization is expected to offer many advantages over the current methods reported in the literature for the passivation of surfaces, in addition to making the surfaces resistant against air- and moisture-assisted degradation. The surfaces of the nanowires are never exposed to ambient atmosphere, unlike *ex-situ* functionalization techniques. This procedure eliminates the probability of oxidation of the surfaces of semiconductors that are highly hygroscopic in nature, such as Zn_3P_2. Unlike liquid-phase functionalization, vapor-phase functionalization does not leave any unreacted functional molecules on the surfaces of the nanowires. Unreacted functional molecules not bound to the nanowire surfaces will simply be pumped out in this procedure. The binding of the functional molecules onto the nanowire surfaces forms a

---

* Excerpts are taken from Physical Chemistry Chemical Physics **15** (17), 6260-6267 (2013) - Reproduced by permission of the PCCP Owner Societies.[11]

self-assembled monolayer (SAM) that acts as a diffusion barrier for moisture and oxygen. These SAMs have not only been shown to prevent corrosion and degradation through limiting the diffusion of molecules to the substrate,[157] but also to enhance charge transfer at interfaces through electron tunneling[158] or electron hopping.[159]

Functionalization Methods

In-situ functionalization of the synthesized Zn_3P_2 nanowires was accomplished by exposing the nanowires to a vapor of the organic functional molecules immediately after the conclusion of the nanowire synthesis. Experimentation for the *in-situ* functionalization of nanowires was executed by terminating the source material flow, cooling the substrates to a temperature of 85 ^oC, and subsequently supplying a vapor of organic functional molecules. Zn_3P_2 nanowires were functionalized using both 4-aminothiophenol (4-ATP) and 3-propanedithiol in this study. The bubbler was maintained at a temperature of 100 ^oC for the supply of 4-aminothiophenol and a temperature of 75 ^oC for the supply of 3-propanedithiol.

To compare the effect of the type of surface passivation on nanowire stability, liquid phase functionalization of Zn_3P_2 was also implemented. *Ex-situ* liquid phase functionalization of the nanowires was accomplished by mixing 5 mg of nanowires with 20 ml of a solution of 5mM 4-aminothiophenol or 3-propanedithiol in isopropanol. The solution was then heated at 80°C for 30 minutes under constant stirring.

The synthesized Zn_3P_2 and Zn_4Sb_3 nanowires, both functionalized and unfunctionalized, were characterized for morphology, crystal structure, and chemical

composition using scanning electron microscopy (SEM), transmission electron microscopy (TEM), X-ray diffraction (XRD) using a Cu Kα source, Fourier-transform infrared spectroscopy (FTIR), Energy Dispersive Spectroscopy (EDS), and X-ray photoelectron spectroscopy (XPS) using a polychromatic Al Kα source. A small piece of polished graphite placed adjacent to the sample served as the reference for standardizing the obtained XPS spectra.

Results

The nanowire characterization by both synthesis techniques for zinc phosphide nanowires, the zinc antimonide nanowires, the stability enhancement provided by the surface passivation, and the chemistry of the functional molecules binding to the nanowire surfaces is discussed thoroughly in this section.

Nanowire Characterization

The vapor transport of zinc and phosphorus (using Zn_3P_2 powder as source) onto substrates formed a green deposit on the substrate. SEM analysis of the deposit (Figure 17a) showed that it is comprised of nanowires approximately 25-40 nm in diameter and tens of microns long. XRD analysis of the nanowires indicated that they are α-Zn_3P_2 with a tetragonal unit cell and have lattice parameters of a = 8.095 Å and c = 11.47 Å. For comparison, an XRD spectrum of the Zn_3P_2 powder source (Sigma Aldrich) is also shown in Figure 17b. TEM analysis of the Zn_3P_2 nanowires indicated that they are single-crystalline with a growth direction of [101] and that there was an amorphous

oxide layer on the surfaces of the nanowires (Figure 17c). The amount of nanowire powder obtained using this experimental strategy is very small (~500 μg per run) and is limited by the area of the substrate employed for their deposition (~1 cm^2).

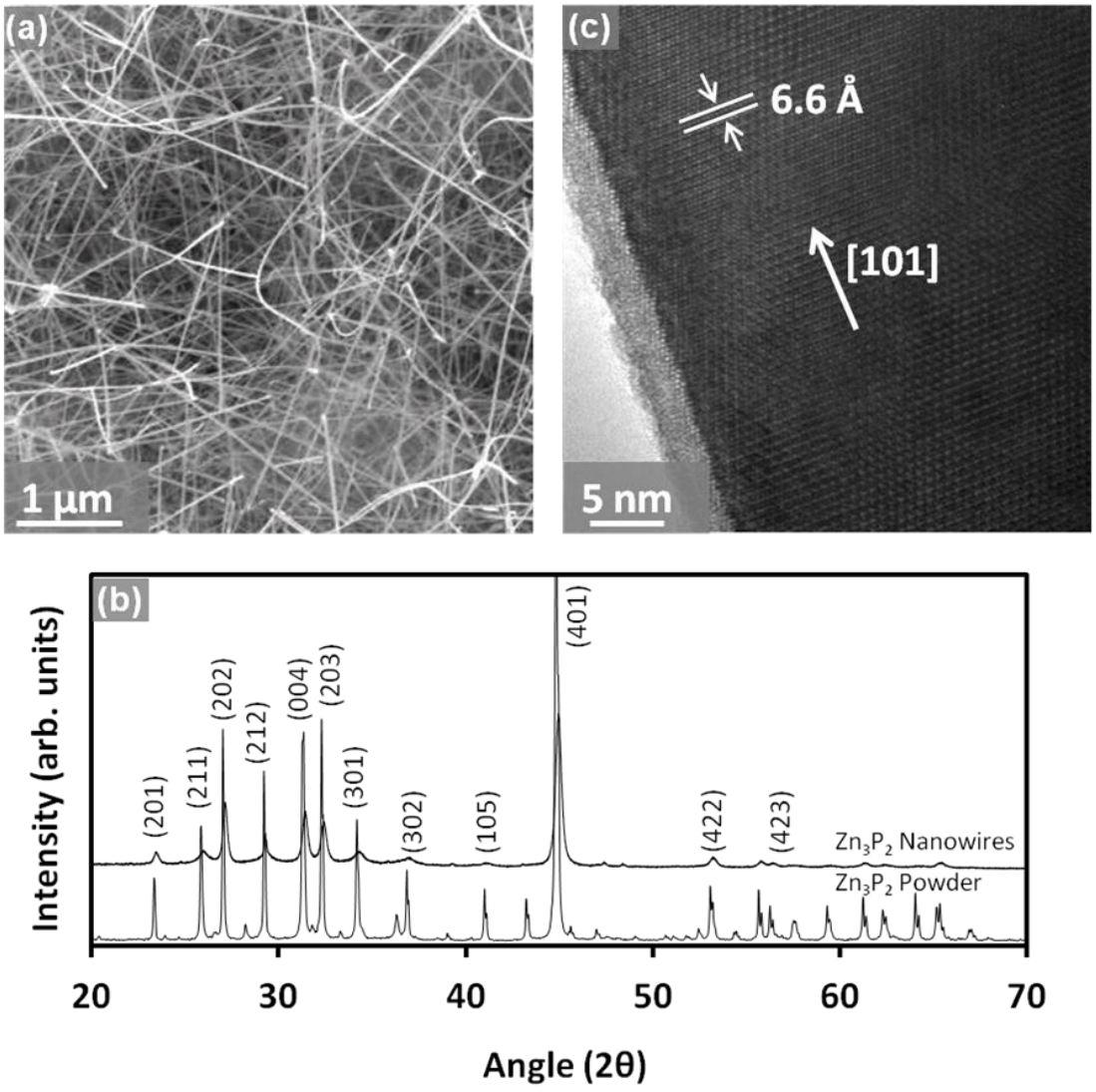

Figure 17. (a) Scanning electron micrograph of Zn_3P_2 nanowires synthesized by reactive vapor of transport of Zn and P from Zn_3P_2 powder source onto quartz substrates. (b) A spectrograph comparing the XRD spectrum of Zn_3P_2 nanowires synthesized using the above-mentioned approach with that of commercially-available Zn_3P_2 powder (Sigma Aldrich). (c) Transmission electron micrograph of a single-crystalline Zn_3P_2 nanowire indicating that the growth direction is [101].

A second experimental route was employed to circumvent this limitation and synthesize gram quantities of nanowire powder. Here, the vapor transport of phosphorus onto heated zinc foils was employed for the synthesis of Zn_3P_2 nanowires. To maximize the area of the foil over which nanowires can be obtained in one experimental run, a large 30 x 8 cm^2 foil was compacted by rolling it concentrically into a 1.5 inch diameter coil as shown in Figure 18a. Due to the high thermal conductivity of metallic zinc, no appreciable thermal gradients are expected across the length of the foil. Consequently, the entire foil is considered to be isothermal under the experimental conditions. The vapor transport of phosphorus onto the zinc foil resulted in the formation of Zn_3P_2 nanowires. A pictorial representation of the experimental setup can be seen in Figure 2b. Photographs of a coiled zinc foil before and after the reaction are shown in Figure 18a and b, respectively. SEM analysis of the green deposit obtained on top of the foils after the reaction (Figure 18b and f) indicated that it is comprised of Zn_3P_2 nanowires 30-50 nm in diameter and tens of microns long (Figure 18e). TEM analysis of these nanowires (Figure 18d) revealed that they are single crystalline and that their growth direction is along the [101] axis. This is consistent with the results observed in the small scale experiments. Following the synthesis, Zn_3P_2 nanowire powder was obtained by simply brushing the foils using the back side of a razor blade (Figure 18c). Using the second experimental route, approximately 250 mg of nanowire powder was produced per run; this is 500 times more per run relative to the small-scale synthesis method.

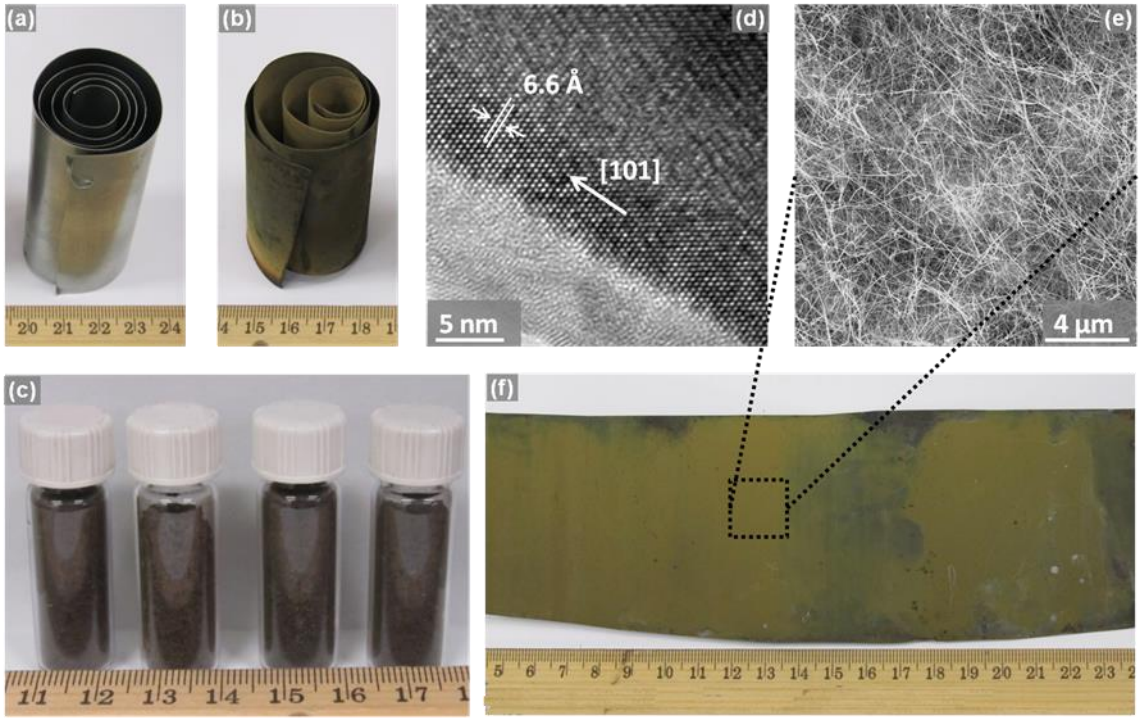

Figure 18. Photograph of a coiled zinc foil (a) before and (b) after the vapor transport of phosphorus. (c) Photograph of Zn_3P_2 nanowire powder obtained by brushing off the foils. (d) A transmission electron micrograph from a Zn_3P_2 nanowire indicating that the growth direction of the nanowires was not altered in the second experimental procedure and remained [101]. (e) A scanning electron micrograph of Zn_3P_2 nanowires obtained by the above-mentioned approach. (f) Photograph of the uncoiled zinc foil covered with Zn_3P_2 nanowires (green deposit) after the vapor transport of phosphorus onto its surface.

Short-term experiments lasting for duration of 5 minutes were performed to understand the mechanism underlying the growth of nanowires on zinc foils. These short term experiments indicated that the formation of Zn_3P_2 crystal nuclei preceded the growth of nanowires (Figure 19). This suggests that self-catalysis via zinc droplets is responsible for the growth of Zn_3P_2 nanowires. In self-catalysis, the reaction of zinc foils with phosphorus leads to the formation of Zn_3P_2 crystal nuclei on the zinc foil. Subsequent zinc adatoms diffuse to form droplets on top of the Zn_3P_2 nuclei. These zinc

adatoms could come from the condensation of vaporized zinc or from the surface diffusion of zinc from the underlying foil. Phosphorus dissolution into these zinc droplets and the ensuing liquid phase epitaxy through the zinc droplets leads to the one-dimensional growth of Zn_3P_2 nanowires.[88] No zinc droplets were observed at the tips in these experiments due to their evaporation or reaction with phosphorus during experimental shutdown. The zinc foils served not only as the substrate, but also as the source of zinc in the large-scale synthesis of Zn_3P_2 nanowires.

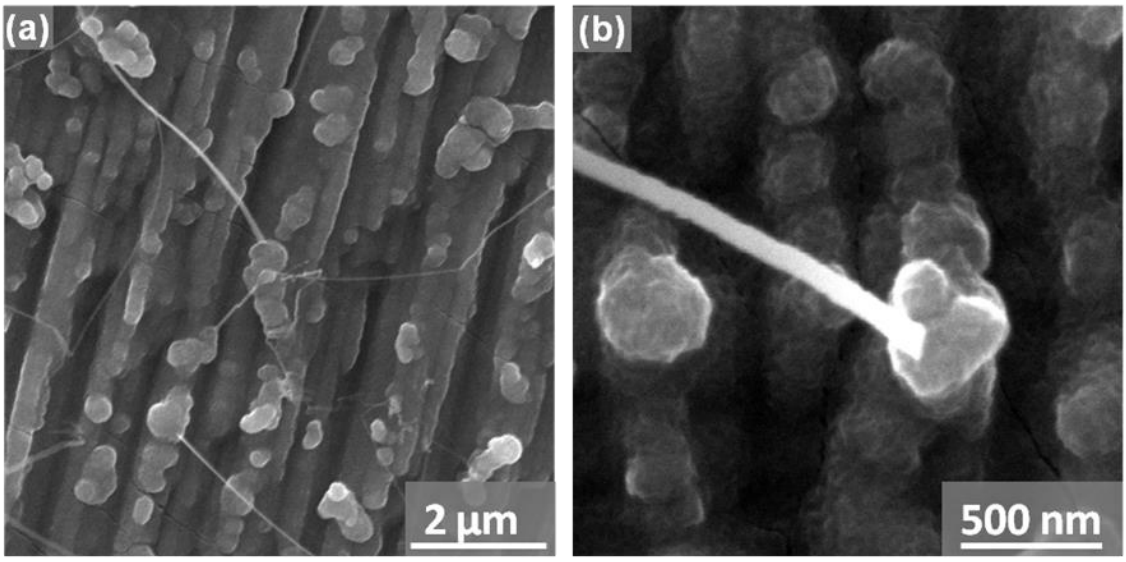

Figure 19. Scanning electron micrographs of a zinc foil after the vapor transport of phosphorus onto its surface for a short duration of 5 minutes. The formation of small Zn_3P_2 crystal nuclei preceded the formation of nanowires. This is indicative of the fact that self-catalysis via zinc droplets is responsible for the formation of nanowires.

The heavier zinc pnictide nanowires were synthesized via a similar route. The reaction of heated zinc foils with $SbCl_3$ supplied via the vapor phase formed 150 nm-thick Zn_4Sb_3 nanowires (Figure 20a). An XRD spectrograph (Figure 20b) shows the

formation of the $Zn_{5.92}Sb_5$ phase of zinc antimonide, nearly identical to that previously reported by Mozhrivskuj *et al.*[160] The variations in the stoichiometry of Zn_4Sb_3 have been previously attributed to a zinc void fraction or a zinc substitution at one of the antimony sites within the crystal lattice.[17] The dotted line displayed is the simulated XRD pattern of the crystallographic information file (COD ID: 4001474) by Mozharivskyj *et al.*[160] in the Crystallography Open Database.[161, 162] The extra peaks are attributed to the zinc substrate (*) and a small amount of ZnSb phase impurity (†). No processing was performed on the data and the Cu $K\alpha_2$ doublet peaks still remain. HR-TEM bright field imaging (Figure 20c) reveal that the nanowires grow along the [101] axis. Lattice fringes can be seen with d-spacings of 5.49 Å and 3.04 Å that are characteristic of the (201) and (104) planes of Zn_4Sb_3, respectively. The synthesis of both the phosphide and antimonide nanowires via self-catalysis results in the same [101] growth direction. Like the Zn_3P_2 nanowires, no droplets can be seen at the tip of the nanowires due to the excess zinc being vaporized or consumed during reaction shut down.

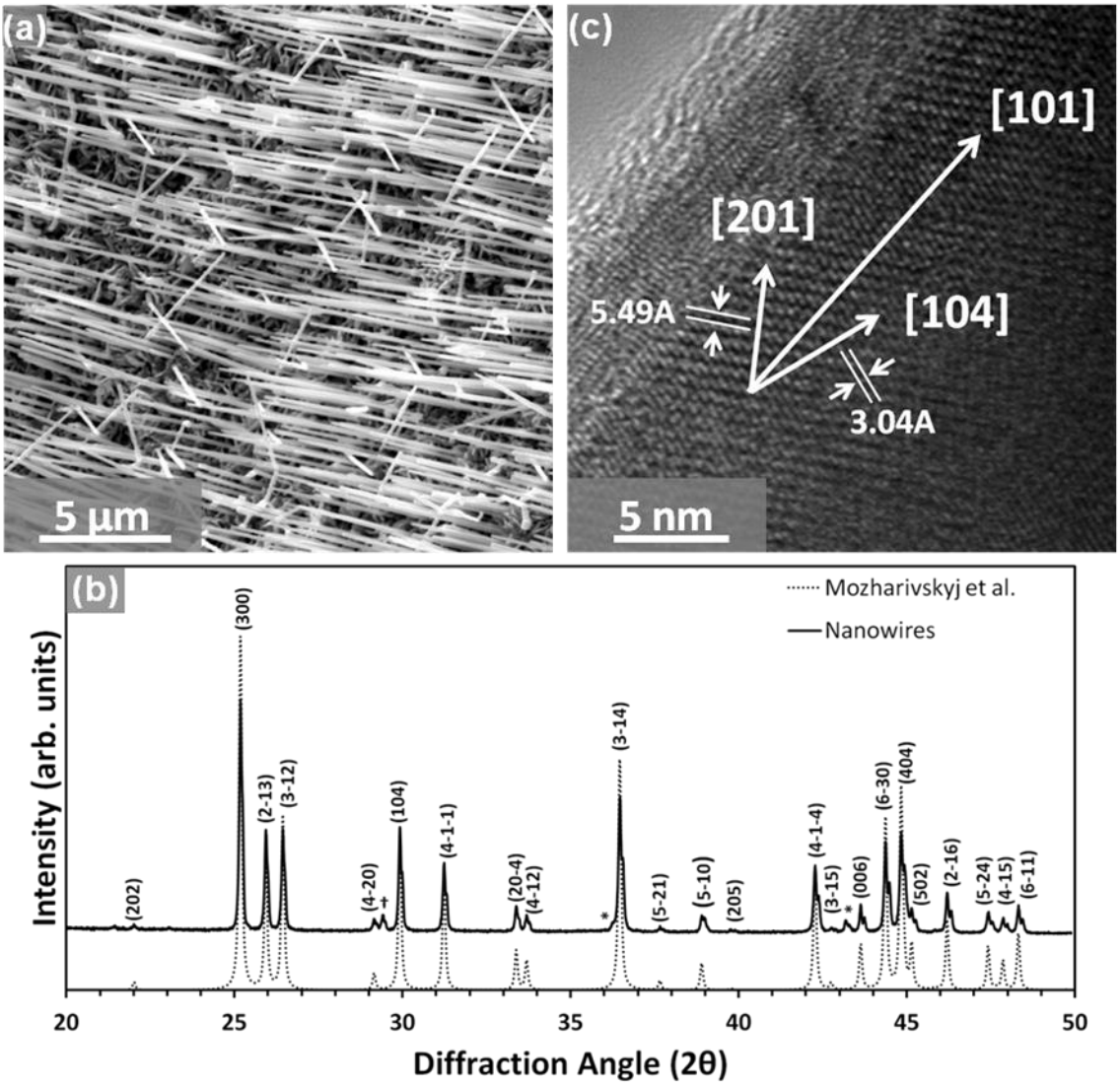

Figure 20. (a) Scanning electron micrographs of 150 nm-thick β-$Zn_{13}Sb_{10}$ nanowires synthesized using direct reaction of zinc foils with antimony chloride. (b) An XRD spectrograph of β-$Zn_{13}Sb_{10}$ nanowires on a zinc substrate (*) is shown. A small amount of the ZnSb phase impurity is also in the spectrograph as indicated by †. The dotted line data is from a simulated $Zn_{5.92}Sb_5$ structure (COD ID: 4001474) by Mozharivskyj *et al.*[160] in the Crystallography Open Database.[161, 162](c) HR-TEM bright field image of a nanowire growing in the [101] direction. Lattice fringes can be seen with d-spacings of 5.49 Å and 3.04 Å that are indicative of the (201)and (104) planes of Zn_4Sb_3, respectively.

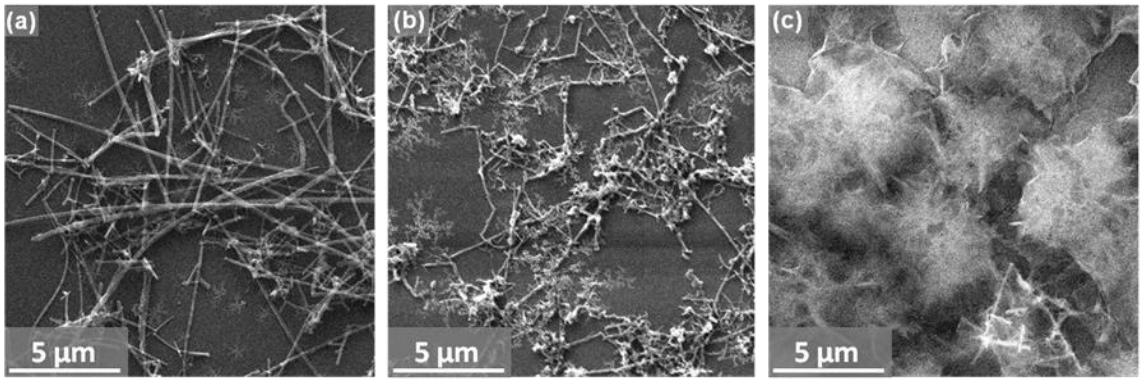

Figure 21. Scanning electron micrographs of (a) *in-situ* 4-aminothiophenol functionalized Zn_3P_2 nanowires, (b) *ex-situ* 4-aminothiophenol functionalized Zn_3P_2 nanowires, and (c) unfunctionalized Zn_3P_2 nanowires after being suspended in THF for 120 days. The *in-situ* functionalized nanowires show no signs of degradation, unlike the other samples.

The 4-aminothiophenol functionalized nanowires were suspended in tetrahydrofuran (THF) for a period of 120 days to determine the effect of *in-situ* functionalization on the stability of Zn_3P_2 nanowires. Afterward, changes to the morphologies of the nanowires were studied using SEM. Unfunctionalized and *ex-situ* functionalized nanowire suspensions were also studied for comparison. The samples for the SEM analysis were prepared by drop casting the nanowire suspension onto silicon wafers sputtered with 5 nm of gold. The SEM analysis indicated that the *in-situ* functionalized nanowires (Figure 21a) were unchanged while the *ex-situ* functionalized (Figure 21b) and unfunctionalized nanowires (Figure 21c) exhibited signs of degradation and agglomeration. Similar results were obtained with Zn_3P_2 nanowires functionalized with 3-propanedithiol (Figure 22).

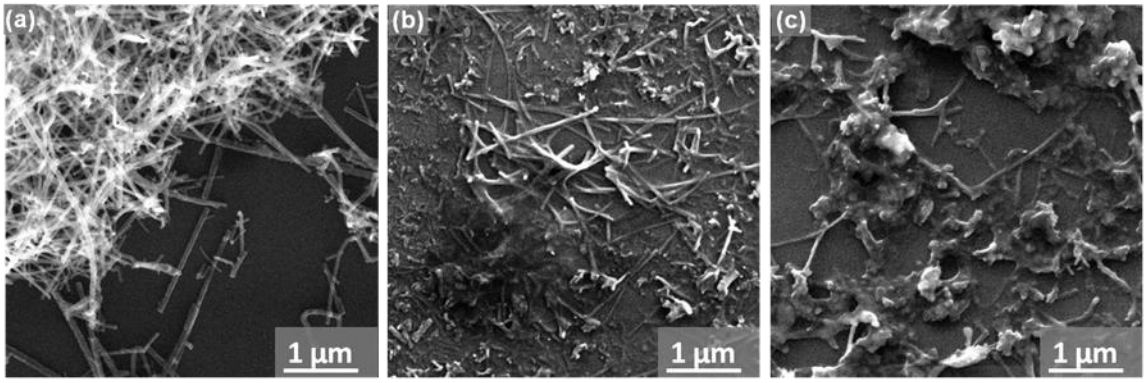

Figure 22. Scanning electron micrographs of Zn_3P_2 nanowires (a) *in-situ* functionalized with 3-propanedithiol, (b) *ex-situ* functionalized with 3-propanedithiol, and (c) unfunctionalized. These images were obtained after a period of 60 days. *In-situ* functionalized Zn_3P_2 nanowires did not exhibit signs of agglomeration and degradation, unlike *ex-situ* and unfunctionalized nanowires.

Interfacial Chemistry

XPS analysis performed to determine the effect of *in-situ* functionalization on the chemical composition of the nanowires indicated the formation of Zn-S bonds between the 4-aminothiophenol molecules and the Zn_3P_2 nanowire surfaces.[100] A comparison of the zinc, sulfur and phosphorus peaks in both the unfunctionalized and the 4-aminothiophenol functionalized Zn_3P_2 nanowires is presented in Figure 23a. Typically, the 3s valence band of zinc in phosphides appears at a binding energy of 140.8 eV. This peak was observed in both the unfunctionalized and 4-aminothiophenol functionalized nanowires. Additionally, the zinc 3s peak in 4-aminothiophenol functionalized nanowires exhibits a shoulder at a binding energy of 144.4 eV. This shoulder indicates that the zinc in Zn_3P_2 nanowires is not only bound to phosphorus, but also the sulfur of the 4-aminothiophenol molecules. The absence of a shift or broadening of the phosphorus 2s peak at a binding energy of 186.1 eV confirms that no bonding occurred

between phosphorus and sulfur.[163] The formation of thiolate bonds between the zinc atoms of Zn_3P_2 and the sulfur atoms of 4-aminothiophenol molecules is also evident from the sulfur $2p_{3/2}$ peak at a binding energy of 163.8 eV.[164, 165] As expected, these thiolate bonds are not found in the unfunctionalized nanowires in Figure 23a. The absence of a peak at higher binding energies (greater than 166 eV) in this region also rules out the formation of sulfone species.[106] The slight amount of asymmetry on the sulfur $2p_{3/2}$ peak can be attributed to the physisorption of the 4-aminothiophenol to the nanowire surfaces, which is considerably less than that observed in functionalized 4-aminothiophenol SAMs from solution based approaches.[165, 166] This further emphasizes the quality of the *in-situ* vapor phase functionalization technique. A sulfur 2s peak at 226.9 eV is also only present in the XPS spectrum of the 4-aminothiophenol functionalized nanowires in Figure 23a, consistent with that reported in the literature.[167] Phosphorus 2s peaks characteristic of phosphide bonds in Zn_3P_2 can also be observed at a binding energy of 186.1 eV in both the functionalized and unfunctionalized nanowire samples. These phosphorus 2s peaks are consistent with previously reported values of Zn_3P_2.[163, 168] A phosphorus 2s peak at a binding energy of 191.1 eV is also present in the unfunctionalized Zn_3P_2 sample. This peak is characteristic of phosphate formation[168, 169] due to the oxidation of the nanowires. The *in-situ* functionalized nanowires do not have this phosphate peak.

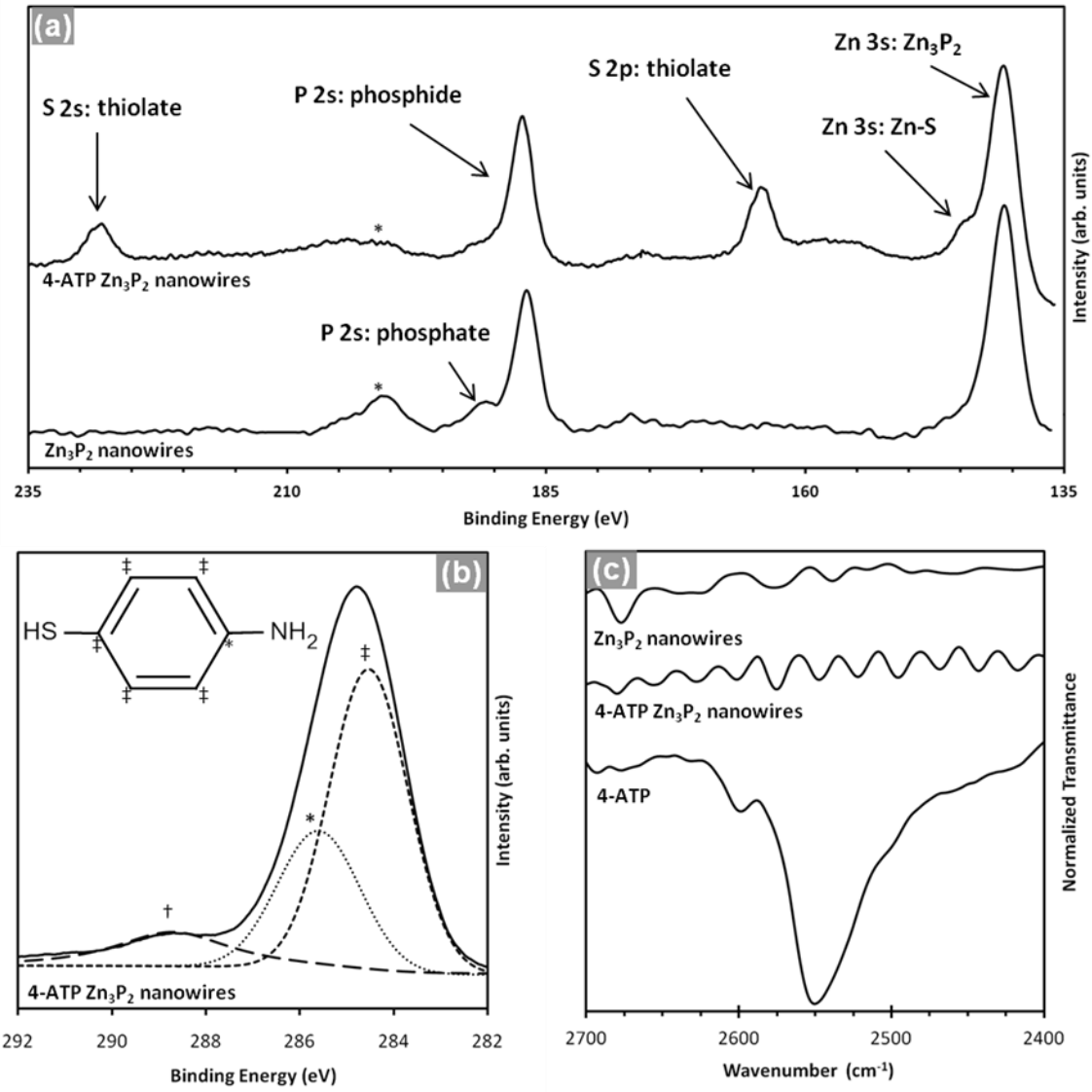

Figure 23. (a) High resolution X-ray photoelectron spectrographs of both the unfunctionalized and 4-aminothiophenol (4-ATP) functionalized Zn_3P_2 nanowires. (the * represents a chlorine peak in $ZnCl_2$ from the acid cleaning). (b) Deconvolution of the carbon 1s peak in the XPS spectrum of 4-ATP *in-situ* functionalized Zn_3P_2 nanowires using Voigt profiles indicated contributions from the 3 different types of carbon in the 4-ATP molecule, namely aromatic C-C/C-S bonding (‡), aromatic C-N bonding (*), and adsorbed CO (†). (c) FTIR spectrographs of the *in-situ* functionalized Zn_3P_2 nanowires showing the absence of the thiol peak characteristic of the thiolation of the nanowires. For comparison, spectra from both unfunctionalized Zn_3P_2 nanowires and 4-ATP molecules are presented.

Figure 23b shows the deconvolution of the carbon peak of the *in-situ* functionalized nanowires sample. The fit Voigt profiles include the three different types of carbon atoms in the 4-aminothiophenol molecule. Peaks at binding energies of 248.6 eV, 285.6 eV, and 288.6 eV are characteristic of aromatic carbon-carbon/carbon-sulfur bonding, aromatic carbon-nitrogen bonding, and carbon from surface adsorbed carbon monoxide (CO), respectively. This is consistent with data previously presented for 4-aminothiophenol[165] and for CO adsorption.[170] The presence of all three peaks is evidence that the phenyl ring remains intact with no bonding changes within the aromatic functional molecules. Therefore, both the Zn_3P_2 nanowires and 4-aminothiophenol molecules are still intact with the only bonding change being a thiolate formation between zinc of the nanowires and sulfur of the 4-aminothiophenol. The unfunctionalized sample also exhibits signs of phosphate formation due to the lack of oxidation protection from the *in-situ* surface passivation with the 4-aminothiophenol.

FTIR spectroscopy of both the unfunctionalized and functionalized nanowires (Figure 23c) confirmed the XPS results and indicated the formation of thiolate bonds between 4-aminothiophenol and Zn_3P_2 nanowires in the functionalized sample. An FTIR spectrograph showing the absence of a peak at 2550 cm^{-1}, characteristic of an S-H stretch,[171] in the *in-situ* functionalized nanowires agrees with the XPS result of complete deprotonation of the 4-aminothiophenol and bonding of the sulfur with zinc (Figure 23c). For comparison, FTIR spectrographs of 4-aminothiophenol, indicating a thiol stretch, and unfunctionalized nanowires with no stretch peak are also shown in Figure 23c.

Conclusions

Zinc phosphide and zinc antimonide nanowires were synthesized on a gram-quantity scale by using a direct reaction of the elements in a hot-walled CVD reactor. Additionally, the nanowire surfaces were passivated using an *in-situ* vapor phase technique to protect them from oxidation when exposed to atmosphere and prevented their agglomeration when suspended as a colloid. Not only is this all-dry technique simple to execute, but it is also prevents a native oxide layer from forming on the nanowires upon exposure to the atmosphere. The absence of this native oxide layer removes the need for chemical etching that could adversely affect the size, morphology, and composition of the nanowires before they are used in device fabrication. These strategies for the large-scale production and *in-situ* functionalization of nanowire powders open many opportunities for not only zinc pnictides, but a broader range of nanomaterials to be used in energy conversion devices, despite their surface reactivity and stability short-comings.

CHAPTER VII

Zn_3P_2 NANOWIRE THERMOELECTRIC PERFORMANCE*

Introduction

As waste heat scavenging using thermoelectrics is a bulk application requiring macro devices, it is essential to study whether the enhanced thermoelectric performances exhibited by individual nanowires are translatable to a bulk device composed of many nanowires. Accomplishing this task requires strategies for the mass production of nanowires and the large-scale assembly of the obtained nanowires. Such large-scale assembly of nanowires into bulk thermoelectrics has seldom been attempted. In sharp contrast, nanoparticles of materials have been employed for the fabrication of bulk thermoelectric modules. Typically, bulk thermoelectric modules from nanomaterials have been assembled using a combination of top-down and bottom up approaches.[172, 173] These strategies primarily involved ball milling bulk materials into nanoparticles followed by pressing the nanoparticles into pellets. Although this strategy is simple and cost effective, the complete effect of nanostructuring on the thermoelectric performance may not be fully realized due to the wide size distribution [174] of the nanopowders created in this way. Similarly, the possibility of grain growth, and hence destruction of nanostructuring, during the compaction of nanoparticles prevents the realization of enhanced thermoelectric performance expected from nanomaterials. The problem of

* Excerpts are taken with permission from Nanotechnology **25,** 145401 (2014) - Copyright (2014) IOP Publishing.[12]

compaction is more pronounced in nanowires as they are asymmetric in shape (unlike nanoparticles) with two distinct dimensions, the diameter and the length.

The material system chosen for this study, zinc phosphide (α-Zn_3P_2), has been predicted to be a viable option as a thermoelectric material due to its low cost, large component-element abundance in the earth's crust,[29] and complex tetragonal crystal structure.[175] The lattice of α-Zn_3P_2 is a distorted anti-fluorite structure with lowered symmetry to a tetragonal unit cell due to the partial filling of the lattice zinc sites resulting in a low lattice thermal conductivity[176] and p-type electrical conductivity.[177] Previous studies have indicated that Zn_3P_2 exhibits a low thermal conductivity of 1.2 $Wm^{-1}K^{-1}$,[178] making it a material of interest for thermoelectric module fabrication. However, Zn_3P_2 lacks the high electrical conductivity [178] and the surface stability [32, 11, 30] necessary for its widespread use in thermoelectric cells and modules. The high surface reactivity and instability of zinc phosphide makes it an ideal test material. It aids in understanding whether surface passivation of nanowires with conjugated organic molecules (e.g., 1,4-benzenedithiol, p-phenylenediamine etc.) prior to their assembly into pellets offers both enhanced interfacial electrical conductivity and stability necessary for their use in thermoelectric device fabrication. Specifically, consolidation of surface passivated (or functionalized) nanowires is expected to lead to interfaces that have different chemical compositions. This fact is expected to aid in determining the effect of interfacial chemical composition on the thermoelectric performance.

Nanowire Assembly Methods

α-Zn_3P_2 nanowires were synthesized on a gram-quantity scale using the reactive vapor transport of red phosphorus onto zinc foils in a hot-walled chemical vapor deposition (CVD) chamber, as previously reported.[11] The same process was employed for obtaining 1,4-benzenedithiol (BDT) functionalized nanowires, in addition to unfunctionalized Zn_3P_2 nanowires. Functionalized nanowires were simply obtained by exposing the Zn_3P_2 nanowires to a vapor of BDT organic functional molecules immediately after their synthesis, and before their removal from the vacuum chamber.[11] This surface functionalization was performed at a temperature of 85 °C.[11] Following the synthesis, the surfaces of both the functionalized and unfunctionalized foils were simply brushed off to obtain nanowire powders.[11] The nanowire powders obtained were characterized for morphology, phase and chemical composition using scanning electron microscopy (SEM), transmission electron microscopy (TEM), X-ray diffraction (XRD), X-ray photoelectron spectroscopy (XPS), energy dispersive spectroscopy (EDS), and Fourier-transform infrared spectroscopy (FTIR), and reported in a previous study emphasizing the synthesis and stability of the individual nanowires.[11]

Consolidation of the synthesized Zn_3P_2 nanowire powders into pellets was performed by hot uniaxial pressing performed at a temperature of 650 °C and a pressure of 120 MPa for 1 hour. The temperature and pressure profiles employed are depicted in Figure 24. Following hot uniaxial pressing, the flat faces of the cylindrical pellets were mechanically polished to reduce their surface roughnesses and make them parallel to each other. In reiteration, pellet densities were determined by measuring their respective

masses and volumes and confirmed using Archimedes principle. The morphology, grain structure, and composition of the polished nanowire pellets were obtained using back-scattered SEM, TEM and XRD. Finally, the heat capacity of the pellets was measured using differential scanning calorimetry (DSC), and the thermal diffusivity was determined by a laser flash apparatus (LFA). Electrical conductivity was measured using the Van der Pauw 4-point probe method, and the Seebeck coefficient was determined by varying the temperature gradient across the pellet cross-section and measuring the resulting voltage. All transport properties were measured from 300 K to 770 K.

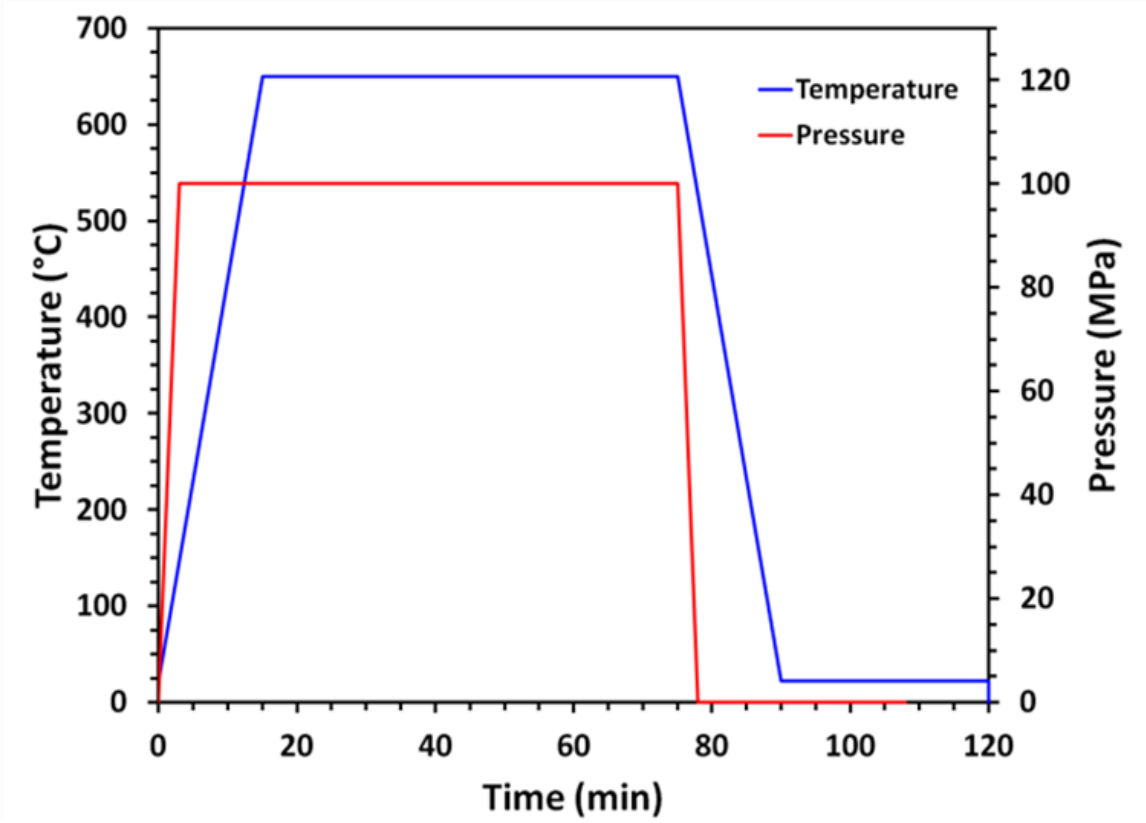

Figure 24. Temperature and pressure profiles employed for consolidating Zn_3P_2 nanowires into dense pellets.

Results

This section includes the results of the zinc phosphide nanowire compaction and physical property characterization. Additionally, the thermal and electrical transport properties of the pellets are included.

Physical Properties

Nanowire pellets 12 mm in diameter and 1 mm in thickness resulted from the uniaxial pressing of nanowire powders (inset of Figure 25). The densities of both the unfunctionalized and BDT functionalized nanowire pellets were determined to be ≥ 98% of the theoretical density of Zn_3P_2 (4550 kg/m^3).[49] XRD analysis of both the unfunctionalized and BDT functionalized nanowire pellets (Figure 25) indicated that the hot-pressing procedure employed for consolidating nanowire powders did not alter their composition, and that the pellets retained the α-Zn_3P_2 crystal structure. The XRD analysis also indicated that any reaction between the sulfur of the BDT molecules and the Zn of Zn_3P_2 during the hot pressing of functionalized nanowire powders did not result in the formation of crystalline ZnS. Morphological analysis of cleaved surfaces of both unfunctionalized and BDT functionalized nanowire pellets using back-scattered scanning electron microscopy indicated that the nanowire morphology remained intact within them (Figure 26b and d, respectively), despite the high packing densities achieved. The average diameter of the nanowires also remained the same after the compaction implying that minimal grain growth occurred throughout the nanowire pellet (for comparison, micrographs of as-synthesized unfunctionalized and BDT

functionalized nanowires are respectively depicted in Figure 26a and c). To further confirm that the pellets are composed of only nanowires, destructive testing was also employed. This testing involved grinding the pellets into small pieces, followed by morphological analysis of the pieces using a TEM. Selected area electron diffraction (SAED) patterns of the Zn_3P_2 nanowires extracted from the pellets confirmed that their crystal structures remained unchanged after their consolidation. This was observed to be true for both functionalized and unfunctionalized nanowires (Figure 27).

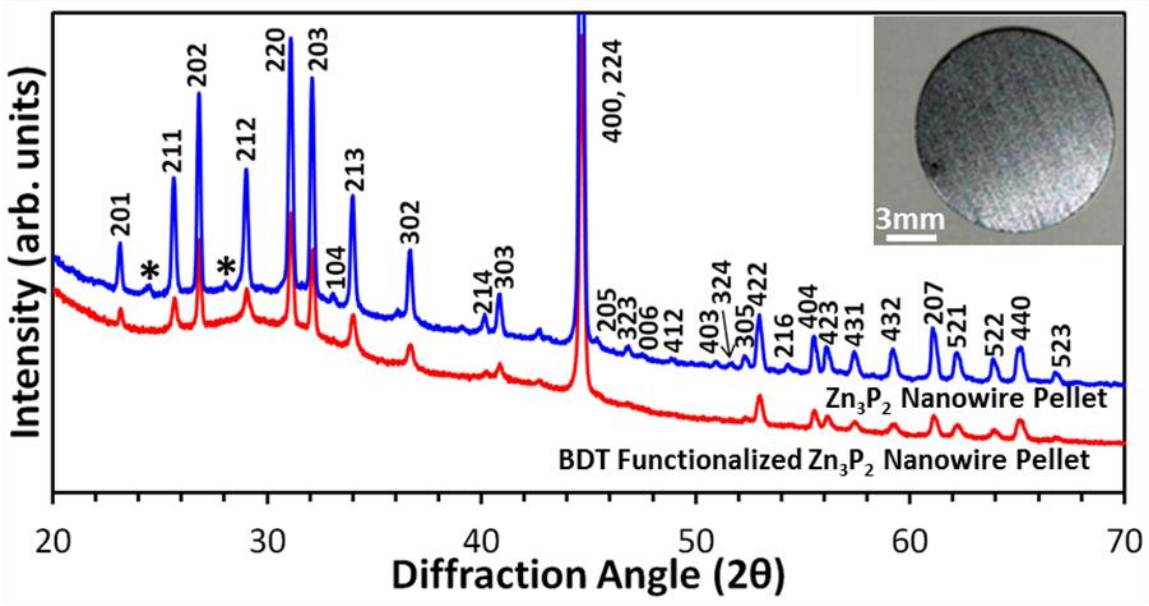

Figure 25. X-ray diffraction spectrographs of nanowire pellets indicating that they retain the Zn_3P_2 crystal structure of the orginal nanowires employed in their fabrication. While the unfunctionalized nanowire pellet indicated the presence of a contaminant $Zn_3(PO_4)_2$ phase (($Zn_3(PO_4)_2$ peaks are indicated with a '*'), BDT functonalized nanowire pellets indicated the presence of no contaminant crystalline phase. A photograph of a 12 mm wide Zn_3P_2 pellet obtained by hot pressing nanowire powders is included in the inset.

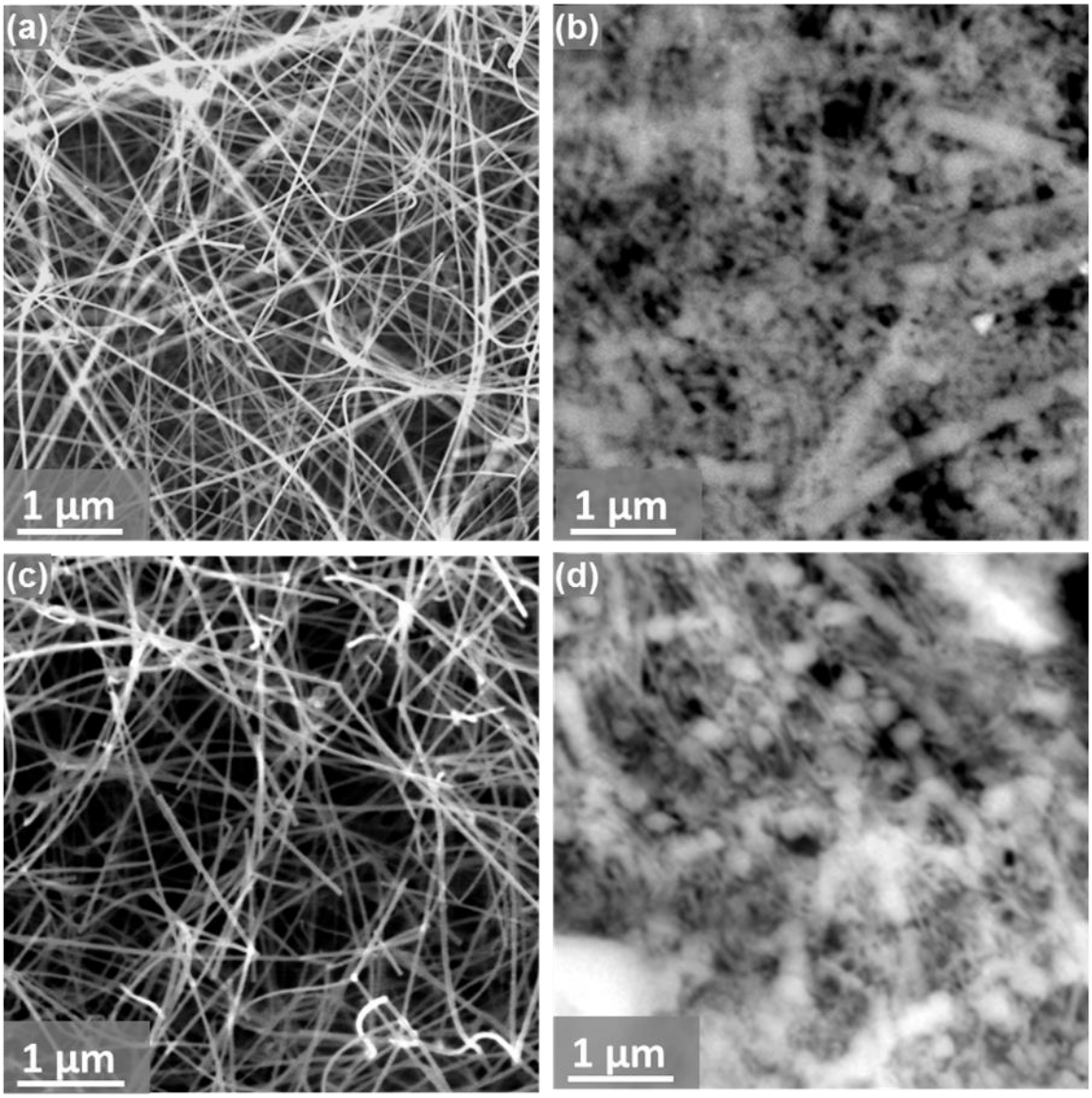

Figure 26. Scanning electron micrograph of (a) as-synthesized Zn_3P_2 nanowires, and (c) functionalized Zn_3P_2 nanowires. Scanning electron micrographs of cleaved surfaces of (b) unfunctionalized and (d) BDT functionalized nanowire pellets obtained using the back- scatter detector. The micrographs in (b) and (d) clearly indicate that nanowire morphology is retained within the pellet, despite the fact that consolidation resulted in highly dense pellets.

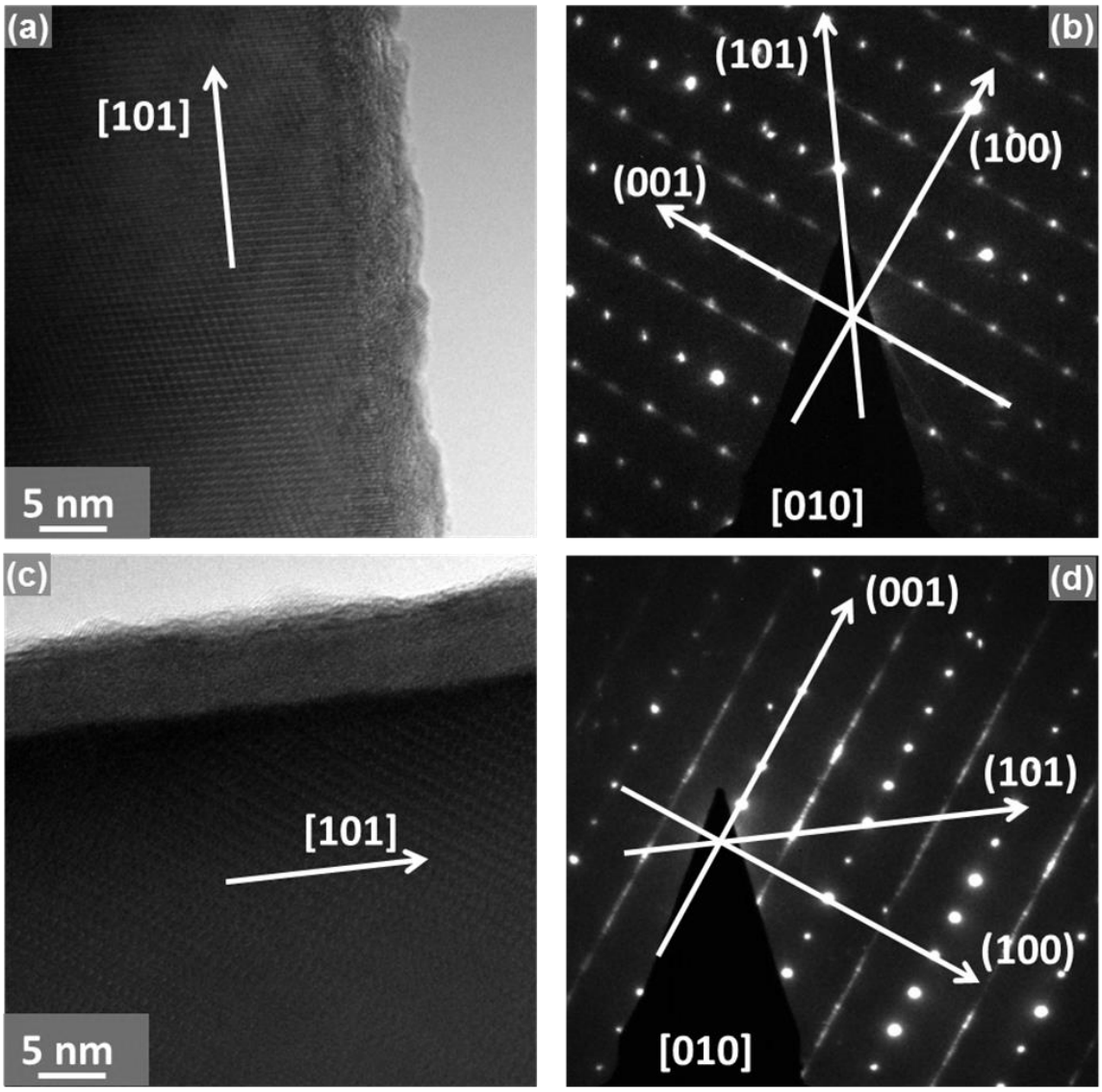

Figure 27. TEM micrographs of (a) unfunctionalized and (c) 1,4-benzenedithiol functionalized nanowires extracted from pellets by grinding. The analysis indicated that the nanowires still remain in the pellet despite the high densities of packing achieved in them. SAED micrographs of the (b) unfunctionalized and (d) 1,4-benzenedithiol functionalized nanowires, indicating that the nanowires retained their original Zn_3P_2 crystal phase after hot uniaxial pressing.

Nanowire Bending

Typically, the packing of randomly oriented rigid rods results in highly porous pellets. Monte Carlo simulations by Abreu *et al*. indicated that the mean porosity in monodispersed beds of rigid spherocylinders with aspect ratios of 3.5 is approximately 47%.[179] Any attempts to increase the packing densities of nanowires through the application of high pressures and temperatures will lead to the breaking of nanowires along their lengths. However, the packing density of randomly oriented nanowires can be increased, without breaking them along their lengths, if the nanowires are mechanically flexible. Such flexibility was recently observed and reported in silicon nanowires of various sizes.[180-183] This enhanced flexibility was attributed to nanowires having fewer defects per unit volume, compared to their bulk counterparts.[181] To confirm that enhanced flexibility is responsible for the high packing density of Zn_3P_2 nanowires in the pellets with the simultaneously retention of their morphology, mechanical characterization of nanowires was performed using a TEM equipped with a Nanofactory SA 2000 in situ STM-TEM Stage. This in situ STM-TEM stage consists of an STM tip held on one-side, while the other end of the holder has a metal wire substrate on which the nanowires are mounted. The STM tip is mounted on top of a piezo-driven stage, capable of precise movements in x-, y- and z- direction with a resolution of 1 nm. For the determination of the mechanical robustness of the nanowires, different Zn_3P_2 nanowires were mounted on a gold wire using silver paste and subjected to cycles of bending and relaxation by moving the STM tip relative to the gold wire (Figure 28a). Simultaneously, images of the nanowires under various stages of bending (Figure 28b-g)

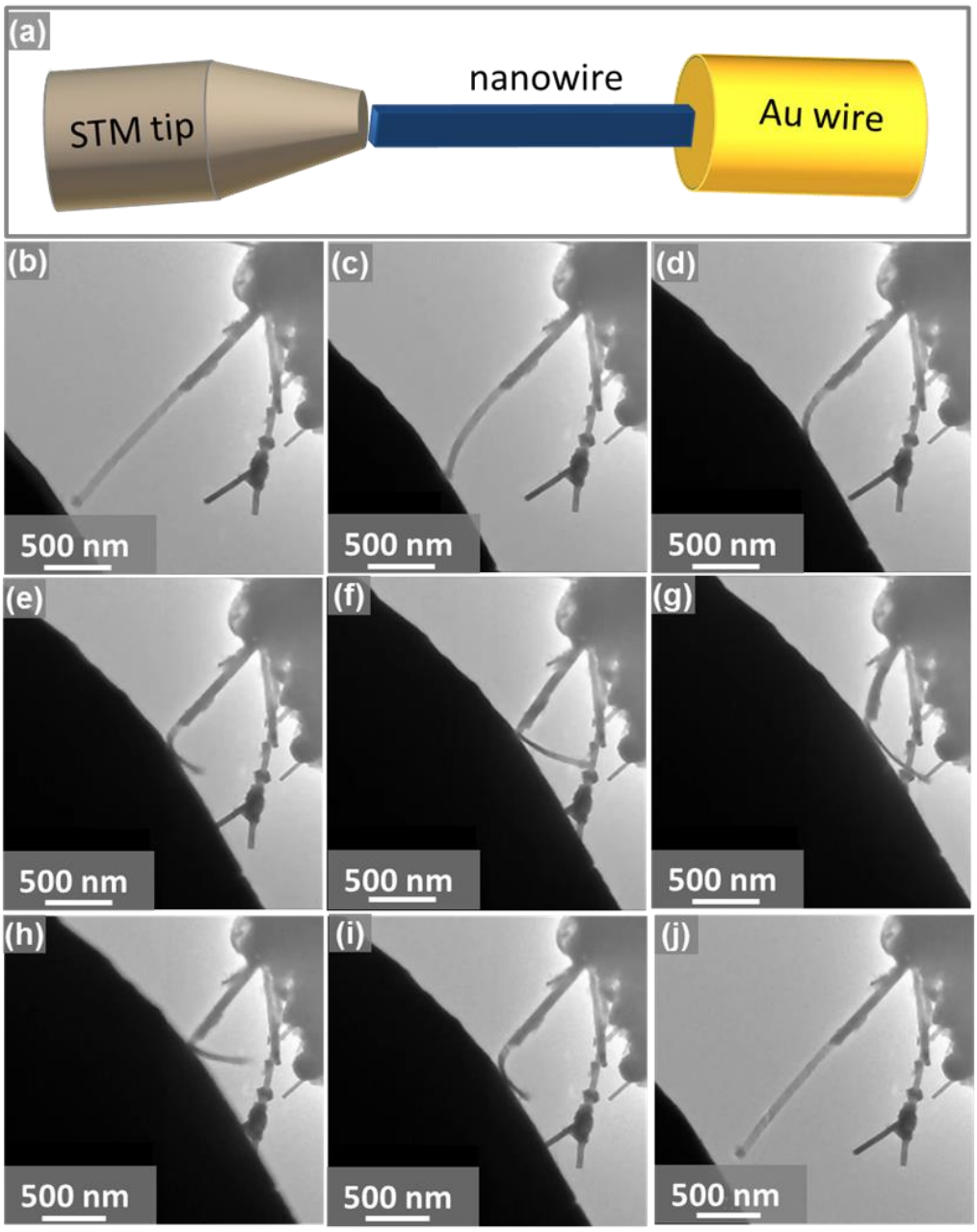

Figure 28. (a) A schematic representing the experimental setup employed for testing the mechanical properties of the nanowires. This setup is mounted inside a TEM for determining the mechanical properties of the nanowires. The movement of the STM tip relative to the nanowire mounted on a metal wire is employed to determine whether the nanowires are mechanically flexible or rigid. (b-g) TEM images of a 50 nm-thick nanowire under various stages of bending. On application of stress, the nanowire was observed to bend at angles exceeding 90^{o}. (h-j) The nanowire was observed to elastically return to its original state after the removal of the applied stress.

and relaxation (Figure 28h-j) were obtained using the TEM. Multiple nanowires were tested using the TEM, and the experimentation indicated that sub-50 nm thick Zn_3P_2 nanowires are mechanically flexible and recover elastically back to their original shape, even after multiple bending cycles. No change in the morphology of the nanowires was observed after repeated bending/relaxation cycles. Overall, these results indicate that the nanowire morphology can remain intact in a dense pellet if the nanowires are flexible.

Thermal Transport Properties

The thermal conductivity of the Zn_3P_2 nanowire pellets was calculated from experimentally measured heat capacities and thermal diffusivities using the following relationship: $\kappa = \alpha\rho C_P$.[184] Here, κ is the thermal conductivity, α is the thermal diffusivity, ρ is the density, and C_p is the heat capacity of the material. The variation of thermal conductivities with temperature of both the unfunctionalized and functionalized Zn_3P_2 nanowire pellets is plotted in Figure 29. For comparison, the thermal conductivity of spark plasma sintered Zn_3P_2 microparticles previously reported by Nagamoto *et al.*[178] is also plotted in Figure 29. Examination of this data shows that at low temperatures (up to ~ 420 K) the thermal conductivities of both unfunctionalized and BDT functionalized Zn_3P_2 nanowires and the Zn_3P_2 microparticles are generally close to each other. However, at higher temperatures, the thermal conductivities of the nanowires were observed to be lower than that of the microparticles. A maximum reduction of 28% in thermal conductivity of Zn_3P_2 nanowire pellets relative to the Zn_3P_2 microparticles was observed at a temperature of 770 K. The enhanced phonon scattering resulting from the

presence of more interfaces per unit volume in Zn_3P_2 nanowires pellets relative to Zn_3P_2 microparticle pellets employed by Nagamoto *et al*., is responsible for lower thermal conductivities. Such phonon scattering has been previously shown theoretically [185, 186] and experimentally.[187] There was virtually no difference in thermal transport between the unfunctionalized and the BDT functionalized nanowire pellets. This is attributed to the fact that both pellets have similar grain size and consequently the same number boundaries and interfaces to scatter phonons.

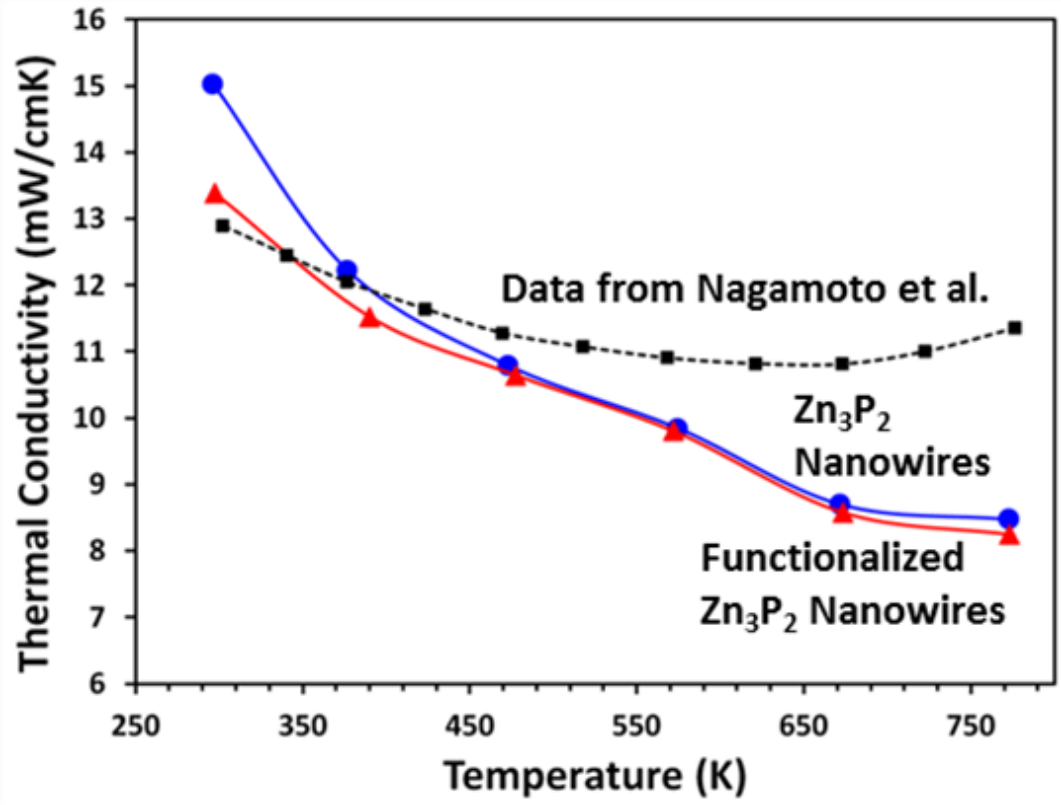

Figure 29. Variation of the thermal conductivities of both unfunctionalized and BDT functionalized Zn_3P_2 nanowire pellets with temperature. For comparison, thermal conductivity of spark plasma sintered Zn_3P_2 microparticles, previously published by Nagamoto *et al*., is also included. As expected, nanostructuring reduced the thermal conductivity of Zn_3P_2 by 28% at 750 K, when compared to that reported by Nagamoto *et al*.

Electrical Transport Properties

Variation of the electrical conductivities of both unfunctionalized and BDT functionalized nanowire pellets with temperature, along with that obtained from Zn_3P_2 microcrystals by Nagamoto *et al*., is presented in Figure 30a. At low temperatures, the electrical conductivity of BDT functionalized nanowire pellets was observed to be orders of magnitude higher than that observed from unfunctionalized nanowire pellets. As the temperature increases, the conductivity values of both unfunctionalized and BDT functionalized nanowire pellets equalize. The thermal activation energy for electrical conduction is estimated to be 0.72 eV for both the samples at high temperatures. This indicates that the bandgap of the material, twice the activation energy of conduction for intrinsic semiconductors,[65] is 1.44 eV. This estimated value is very close to the previously reported bandgap of Zn_3P_2 ~ 1.5 eV,[35] especially when energy gap reduction of semiconductors at high temperatures is taken into consideration.[64] The activation energy value of 0.72 eV is lower than the 1.10 eV reported previously by Nagamoto *et al*.[178] This could be the result of poor interfacial charge transfer in spark plasma sintered Zn_3P_2 microparticles, unlike the dense Zn_3P_2 nanowire pellets obtained in this study. The differences in interfacial conductivities is also believed to be responsible for the large difference between the electrical conductivities of functionalized and unfunctionalized Zn_3P_2 nanowire pellets in the temperature range of 300-600 K (Figure 30a). The lower interfacial conductivity in unfunctionalized Zn_3P_2 nanowire pellets is believed to result of the presence of insulating $Zn_3(PO_4)_2$ at the interfaces. In fact, XPS analysis of the unfunctionalized nanowire reported in a previous study clearly indicated that

unfunctionalized nanowires have a relatively thick $Zn_3(PO_4)_2$ layer on their surfaces.[11] The average thickness of this layer is in the 3-5 nm range (Figure 27a). In sharp contrast, as-obtained functionalized nanowires have conjugated molecules bound to the surface through the formation of Zn-S bonds. During consolidation at high temperatures, these molecules decompose and are ultimately expected to lead to the formation of a relatively thin (relative to unfunctionalized nanowires) amorphous layer composed of Zn, P, S and C. The average thickness of this layer is in 1-2 nm range (Figure 27c). Both TEM (Figure 27a and c) and XRD analyses (Figure 25) prove this fact, by clearly indicating that no other crystalline phases were observed in the BDT nanowire pellets. As a result of the differences in the thicknesses and the chemical compositions of the interfaces, the number of charge carriers crossing the nanowire interfaces in the functionalized pellet is much larger than that observed in the unfunctionalized nanowires at low temperatures.[66] As the temperature increases to about 770K, the carriers have enough thermal energy to surmount the barrier at the nanowire interfaces. Hence, interfacial resistance only plays a minor role in the overall electrical conductivity of the pellets at high temperatures. Consequently, both the unfunctionalized and BDT functionalized nanowire pellets have similar electrical conductivities at high temperatures.

The Seebeck coefficient as a function of temperature for both the BDT functionalized and unfunctionalized pellets are shown in Figure 30b. Both samples show the same p-type semiconducting trend in the temperature range of 400-770K range, with the functionalized sample showing a higher Seebeck coefficient. The Seebeck coefficients obtained in this study were found to be lower than that reported previously

by Nagamoto *et al*. However, BDT functionalization of Zn_3P_2 nanowires not only led to an increase in the electrical conductivity, but also the Seebeck coefficient, when compared to unfunctionalized nanowire pellets. This behavior is counter-intuitive to that expected of typical semiconductors. The semi-classical band theory predicts an inverse relationship between Seebeck coefficient and electrical conductivity for semiconductors.[188] Recently, a few concepts have been proposed to decouple the anti-correlation of the Seebeck coefficient and electrical conductivity to improve the thermoelectric efficiency of a material via power factor enhancement, in conjunction with the traditional approach of thermal conductivity reduction via enhanced phonon scattering at grain boundaries in nanobulk materials.[189] One of the methods to decouple S and σ is to create a material in which energy-independent scattering mechanisms dominate in the desired temperature range;[61] however, no evidence of this occurring in the Zn_3P_2 system exists.[178] Another possible explanation of this apparent contradiction employs the use of energy filtering in heterostructures, where carrier scattering is energy-dependent and low energy charge carriers are selectively scattered at the nanomaterial interfaces.[58-60] This filtering mechanism requires there be a band offset, usually on the order of $\Delta E < 0.2$ eV, to obtain an enhancement in the power factor of the heterostructure material. Carrier filtering requires there be precise control over the energy gap between the Fermi level of the nanowire surface and that of the core to achieve the optimum power factor enhancement.[21, 62] If the band offset between the materials is too low, then the low energy carriers can cross the barrier, and if the offset is too large, the net transport of the majority carriers will be drastically reduced.[62]

Consequently, it is required to have an optimized system in which the interfacial material is chosen in conjunction with a thermoelectric material with a predetermined doping level to maximize these effects. In the case of Zn_3P_2 unfunctionalized and BDT functionalized nanowires, the interfacial properties are governed by the energy barrier between similar Zn_3P_2 nanowire cores, but differing amorphous surface layers at the nanowire interfaces. It is believed that functionalization of nanowires and the subsequent formation of thin amorphous layers composed of Zn, P, S and C at the nanowire interfaces allowed for the formation of low energy barrier ($\Delta E < 0.2$ eV) at the interfaces, and further led to the simultaneous increase in both σ and s. Although the energy barrier at the interfacial layers in these nanowire pellets could be calculated given carrier mobility measurements as a function of temperature for each pellet as given by Seto,[62] the low electrical conductivity of the undoped samples [62, 63] prevented the generation of a coherent mobility plot for testing the carrier filtering hypothesis. Overall, the thermoelectric power factors of both unfunctionalized and BDT functionalized Zn_3P_2 nanowire pellets (Figure 30c) are higher than those reported for bulk Zn_3P_2 by Babu *et al*.[190] Also, the overall thermoelectric performance of BDT functionalized nanowires is on par with that observed in Zn_3P_2 microparticles by Nagamoto *et al*.

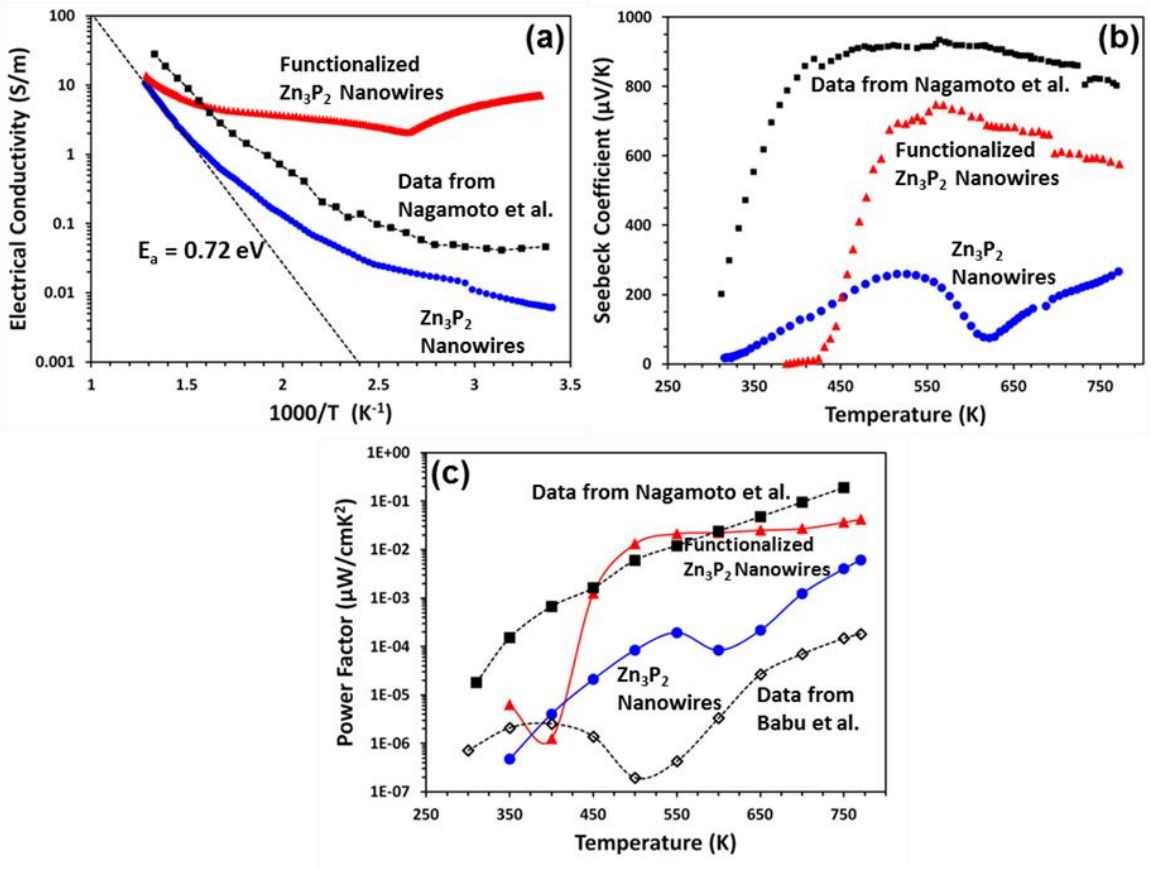

Figure 30. Plots showing the variation of (a) the electrical conductivity and (b) the Seebeck coefficient with temperature for both unfunctionalized and BDT functionalized Zn_3P_2 nanowire pellets. For comparison, data previously reported by Nagamoto *et al*. is also included. (c) Thermoelectric power factors of both unfunctionalized and BDT functionalized nanowire pellets, along with those obtained for bulk Zn_3P_2 by Babu *et al*. and for Zn_3P_2 microparticles by Nagamoto *et al*.

Conclusions

In summary, mass produced Zn_3P_2 nanowires, both unfunctionalized and BDT functionalized, were hot-pressed into dense pellets (densities ≥98% of the theoretical density) without altering their morphologies in the process. The intent here was to deduce the effect of nanostructuring, if any, on the thermoelectric performance of bulk assemblies of Zn_3P_2 nanowires. It was observed that the mechanical flexibility of the

nanowires, specifically observed when their thicknesses are 50 nm or less, afforded their consolidation into highly dense pellets. Thermoelectric performance of the consolidated nanowire pellets indicated that nanostructuring has a positive impact on their thermoelectric performance, as expected. The Zn_3P_2 nanowire pellets not only exhibited higher thermoelectric power factor compared to their bulk counterparts, but also lower thermal conductivities compared to Zn_3P_2 microparticles. BDT functionalization of Zn_3P_2 nanowires allowed for the formation of interfaces that filtered low energy carriers and allowed for the simultaneous increase in both the Seebeck coefficients and electrical conductivities, previously never observed in the Zn_3P_2 material system. It is believed that a further reduction of the nanowire diameters, coupled with doping them using copper,[178] will enhance the zT values of Zn_3P_2 further and make it a viable thermoelectric material.

CHAPTER VIII

ZnO NANOWIRE THERMOELECTRIC PERFORMANCE

Introduction

Over the past two decades oxides have become viable thermoelectric materials due to their low cost, elemental abundance in the earth's crust,[29] low toxicity,[40] and high stability relative to other state-of-the-art thermoelectric materials in oxidizing environments.[40, 41] Many p-type oxide semiconductor materials have been shown to have thermoelectric performance on par with current commercial materials. Some of these polycrystalline materials include layered cobaltites such as $Ca_3Co_4O_9$[42-47] with a high zT of 0.61[45] and Na_xCoO_2[48-51] with a high zT of 0.92.[51] Contrarily, many n-type oxides have yet to exhibit such performance. The state-of-the-art n-type oxide thermoelectrics are $SrTiO_3$[52-57] with a maximum zT of 0.37[57] and ZnO alloy ceramics. Attempts to increase the efficiency of ZnO-based thermoelectrics using homologous compounds of ZnO-In_2O_3 resulted in small efficiency increases.[58-61] Doping[62-65] and co-doping[66-69] of ZnO with aluminum has shown to give the highest n-type zT of 0.65 in $Zn_{1-x-y}Al_xGa_yO$ alloys.[69] The samples with the high zTs were bulk materials with very high thermal conductivities. Consequently, the scope of this chapter is to combine the superior thermoelectric properties of the dually-alloyed samples with nanowire morphology to further increase the zT of the alloy. Ideally, this can be done by retaining the electrical conductivity of the nanobulk material via single-crystalline nanowire conduction

pathways while further reducing the thermal conductivity of the sample by scattering phonons at the nanowire interfaces.

Results

This section includes the physical properties characterization along with the electrical and thermal transport properties of the ZnO alloy nanowire-bulk pellets.

Physical Properties

XRD analysis (Figure 31) indicates that the formation of both aluminum and gallium spinels occur when attempts to dually-doped ZnO with them are performed. The analysis indicated no presence of unreacted gallium and aluminum oxide phases in the samples, and that alumina and the gallium oxide reacted with ZnO. Subsequently, some of the aluminum and gallium supplied precipitated as spinel from the alloy with compositions of $(ZnO)_x(Al_2O_3)_y$ and $(ZnO)_x(Ga_2O_3)_y$, respectively, at all the concentrations studied. These solubility limits are less than the independent solubility limit of both aluminum and gallium in zinc oxide,[191] and contradicts a previous claim that dual doping can increase the solubility limit of Group-III metals in zinc oxide.[69] It is more likely in the previous report that peak broadening due to lattice distortions by Ga doping[192] were responsible for engulfing the precipitant peaks. It has also been shown that as the temperature increases, spinel formation will be much faster due to faster diffusion kinetics.[193] Despite the relatively low temperature of 1200 °C used during pressing, the local temperature at the nanowire grain boundaries will be very high when

using SPS due to their high resistivity and consequential Joule heating.[194] Therefore, more spinel compound will form than would be expected at 1200 °C in 5 minutes. Representative, scanning electron micrographs of the nanowires before pressing (Figure 32a) and the pellet after pressing (Figure 32b) indicate that the pellets are phase pure up to the maximum resolution of the back-scattered electron detector. Furthermore, HR-TEM images of the nanowires before pressing (Figure 32c) indicate that they are single crystalline and grow in the [001] direction. Destructive analysis on the pellets was performed to determine if the same single-crystalline nanowire morphology still exists in the pellet. Although the nanowires were broken into pieces, anisotropic crystalline pieces of ZnO were still recovered in HR-TEM (Figure 32d).

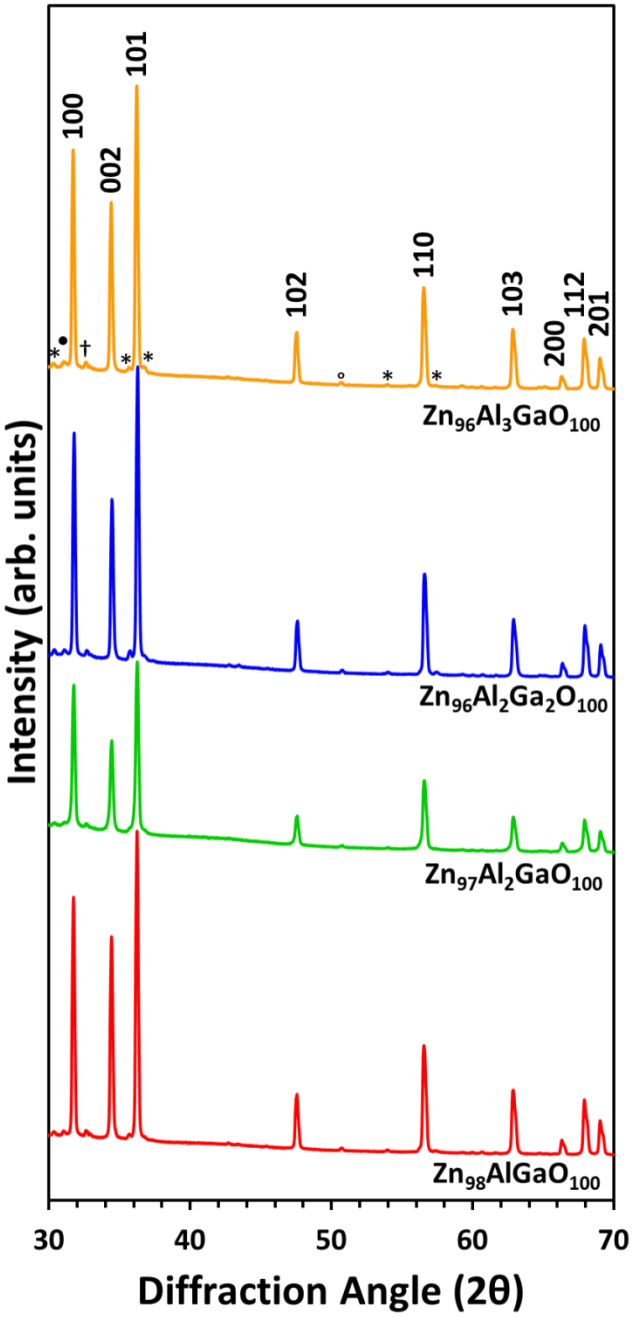

Figure 31. XRD spectrograph of the dually-doped zinc oxide nanowire pellets of various compositions. As expected, the primary phase found was ZnO. The samples containing gallium indicated the formation of $ZnGa_2O_4$ (∗) spinel and $(ZnO)_{13}(Ga_2O_3)_2$ (•) in increasing quantities as more gallium was added. Additionally smaller amounts $ZnAl_2O_4$ (◦) spinel and $(ZnO)_3(Al_2O_3)$ (†) are present.

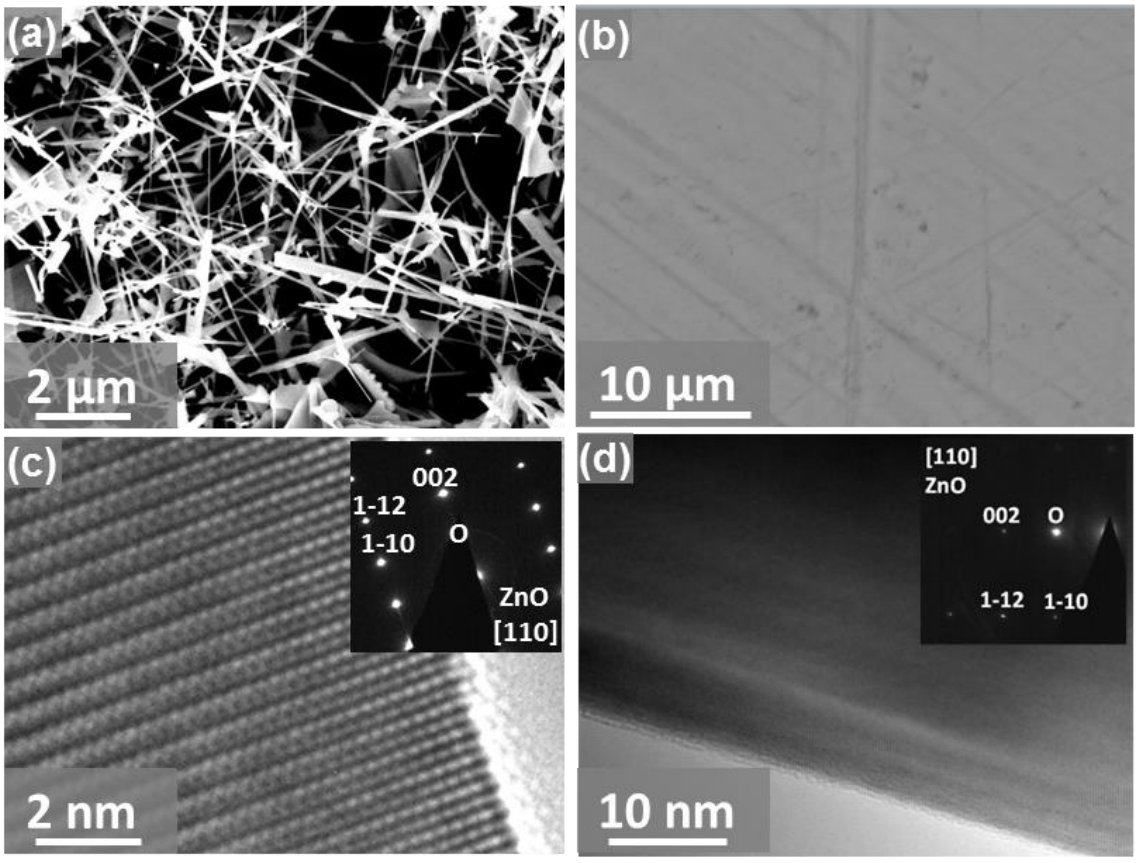

Figure 32. (a) A scanning electron micrograph of the as-synthesized ZnO nanowires employed in this study. (b) A back-scatter SEM image of the nanowire pellet after densification in the SPS indicating phase purity on the macroscale. (c) HR-TEM of an individual ZnO nanowire showing that it is single crystalline and grew along the [001] direction. (d) HR-TEM of a piece of a ZnO nanowire obtained by crushing the nanowire pellet. This analysis indicated that single-crystalline nanowire-shaped anisotropic grains are still present within pellet after compaction.

Further inspection of the grains in the TEM led to the discovery of precipitates in the homologous series[192] $Zn_mGa_2O_{m+3}$ (Figure 33). These precipitates were on the order of 10-20 nm in size depending on the sample concentrations of Al and Ga and nucleated on the nanowire surfaces in an epitaxic manner. As the concentrations of Al and Ga increase in the samples, more nuclei could form during sintering resulting from inverse

proportionality between Group-III element diffusion lengths and concentration. Therefore, the precipitate nuclei could grow much faster in higher concentration samples resulting in larger precipitates. Analysis of the precipitates in HR-TEM (Figure 33a) viewing down the ZnO [110] and $(Ga_2O_3)_2(ZnO)_{13}$ [100] result in 2 ZnO planes per 1 precipitate plane with a lattice mismatch of 1.25% as calculated from Equation 1.

$$\%\Delta = \frac{\mathbf{2[ZnO]_{110}} - \mathbf{[(Ga_2O_3)_2(ZnO)_{13}]_{010}}}{\mathbf{2[ZnO]_{110}}} \times \mathbf{100}$$

Simulated electron diffraction using Fast Fourier Transform (FFT) of the corner of the nanowire (Figure 33b) shows the epitaxic alignment of the 2 phases relative to the wurtzite ZnO background pattern (Figure 33c). The small size of the precipitate ternary phase (<10 nm) can be attributed to the short pressing times preventing the samples to reach thermodynamic equilibrium.

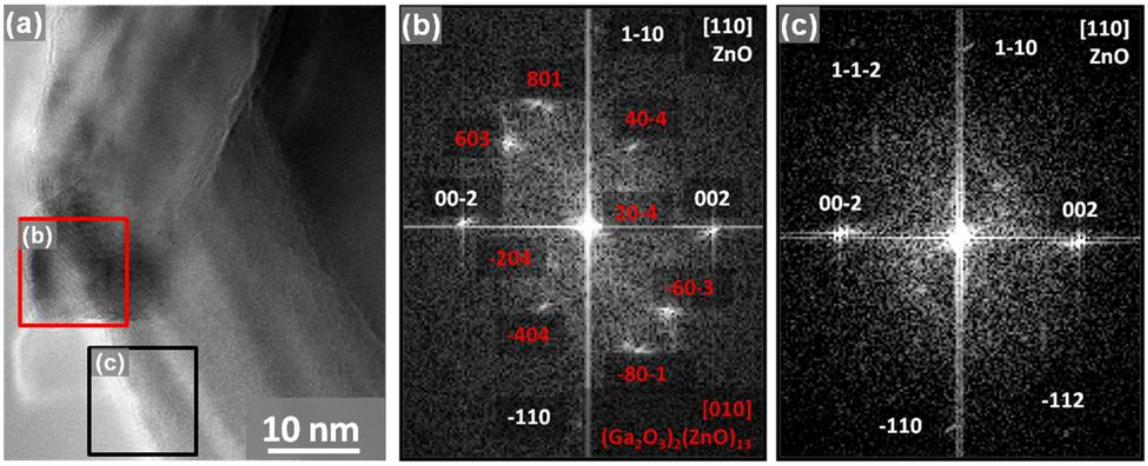

Figure 33. (a)HRTEM image of a broken $Zn_{96}Al_2Ga_2O_{100}$ pellet indicating that the grains retained the single crystal morphology. Fast Fourier Transform (FFT) electron diffraction images of (b) the phase $(Ga_2O_3)_2(ZnO)_{13}$ precipitating out in crystalline format at the edge of a nanowire and (b) background single-crystalline ZnO beneath the precipitant phase.

Electronic Transport

Both aluminum and gallium have previously been utilized as electron donors in ZnO. n-type conductivity is achieved by substituting Al or Ga with 3 valence electrons for Zn with 2 valence electrons in the wurtzite lattice. For every Zn atom replaced with a Group-III element, 1 electron is donated into the conduction band as can be seen in the charge balance (Equation 2).

$$\mathbf{Zn^{2+} = III^{3+}\ e^{-}}$$

The known self-compensation of n-type carriers by zinc vacancies does not occur before the solubility limits of Al or Ga resulting in the maximum solubility of the dopants to solely determine the carrier concentration of the samples.[195] The temperature dependence of electron mobility (μ_H) calculated from the resistivity (ρ) and Hall

coefficient (R_H) can be seen in Figure 34a. For materials where mobility is limited by phonon scattering, $\mu_H \propto T^{-x}$, where x is 1 for degenerate semiconductors and 1.5 for non-degenerate semicondcutors. A power law fit to the curves yields a trend with x slightly larger than 1, consistent with a degenerate semiconductor. This deviation from theory can be attributed to other scattering mechanisms playing a minor role in the electron transport. Carrier concentration (n_H) was also calculated from the Hall coefficient and plotted versus temperature (Figure 34b). The resulting plots indicate that carrier concentration is independent of temperature and constant throughout the entire measurement, further confirming the degenerate semiconductor behavior. The calculated carrier concentrations at the pressing conditions are consistent with the phase diagram in this region which indicates that the equilibrium solubility of Al in ZnO is 0.2% at 1250 °C and 0.5% at 1400 °C.[196] Therefore, most of the dopant added to the ZnO is inactive and must have precipitated out from the alloy as spinel phases as can be seen in the XRD (Figure 31). Additionally, all carrier concentrations were less than the maximum values reported of 8×10^{20} cm^{-3} and 3.7×10^{20} cm^{-3} for aluminum[197] and gallium[198] doped ZnO, respectively.

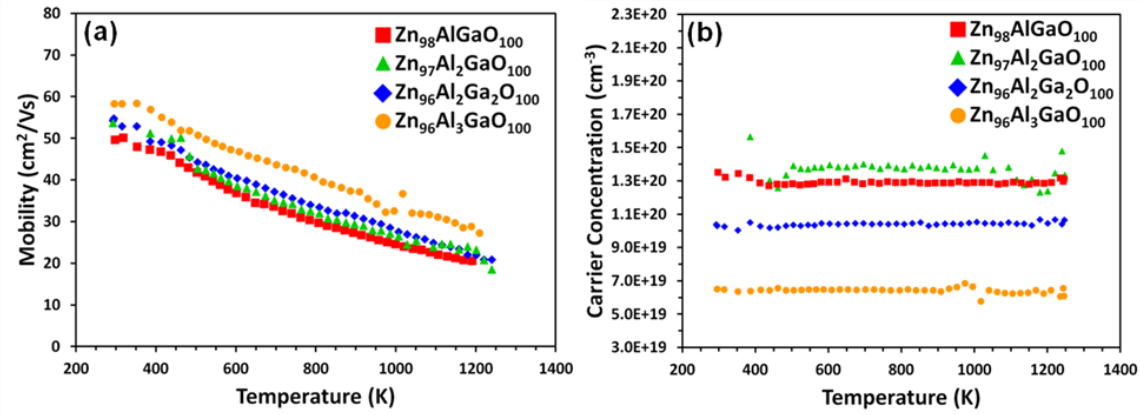

Figure 34. Variation of the (a) carrier mobility and (b) carrier concentration with temperature for dually-doped zinc oxide nanowire pellets. The decay in the mobility is proportional to T^{-1}, consistent with a degenerate semiconductor, in which acoustic phonon scattering limits mobility. The carrier concentration is independent of temperature for each sample, characteristic of degeneracy in the samples.

Electrical resistivity measurements were performed simultaneously with the Hall coefficient measurements and the resistivity increases linearly with an increase in temperature (Figure 35a). The Seebeck coefficient was also measured up to 1000 °C and with all samples has approximately linear temperature dependence (Figure 35b). All samples have a Seebeck coefficient that is inversely proportional to their carrier concentration and follow normal band-behavior except $Zn_{97}Al_2GaO_{100}$. This seems to violate the classical band transport theory which predicts an inverse proportionality between carrier concentration and Seebeck coefficient for a given material. Such a behavior is expected due to resonant electron scattering.[199-201] It has previously been reported that as the concentration of aluminum increases, the impurity band moves from a donor state with an ionization energy of 120 meV[202] to well within the conduction band.[203] Additionally the gallium impurity band has been predicted to always be inside

the conduction band.[204] These impurity energy levels in the conduction band alone could potentially resonantly scatter the host semiconductors electrons, but would have weak effects above ~300K due to acoustic phonon scattering dominating transport. The Seebeck coefficient of the 2% Al, 1% Ga sample is enhanced independent of temperature, and makes the temperature-dependent scattering of electrons by the impurity band improbable. This mechanism also has never been seen before for ZnO and could be further eliminated by performing low temperature mobility measurements. Contrarily, another mechanism that could cause resonant scattering and is more dependent on the band-structure and less on temperature involves the hybridization of the host band-structure with that of the impurity band. In this case, the impurity bands have plane-wave-like wave functions that correspond with those of the host structure and allow the impurity electrons to enhance the power factor.[201] The degree of hybridization between the bands must be balanced to achieve maximum resonance. If the degree of overlap is too much, then the impurity band will behave like the host, and no power factor enhancement will be observed. On the other hand, too little overlap will result in high-Seebeck localized states that do not contribute to the overall performance of the material.[201] When this theory is applied to the dually doped ZnO system, the Group-III valence s-bands could hybridize with the ZnO conduction band resulting in an increased effective electron mass. This resonant phenomenon has not previously been observed in individually Al or Ga doped ZnO systems, but unexplainable Seebeck enhancements have been seen previously in other dually-doped samples[69] in addition to this study. Resonance donor states have also been observed in many other transition metal-doped

II-VI compounds.[205] If the conduction band is hybridized a changed effective mass would be observed; these values can be approximated using the single parabolic band model.[206, 207] Effective mass calculations result in the lowest and highest nominally doped samples having an effective mass of $0.29m_e$ and $0.26m_e$, respectively, similar to that of pure ZnO ($0.29m_e$).[208] Contrarily, the samples with the two middle amounts of dopant added had effective masses of $0.41m_e$ and $0.90m_e$. Table 1 summarizes the properties of the samples at 1073K for direct comparison. The large increase in the effective mass results in a much larger Seebeck coefficient, and consequently, larger power factor of the optimally performing sample ($Zn_{97}Al_2GaO_{100}$). Therefore the hybridization of the impurity states with the conduction band is a very probable scenario to explain the enhanced thermopower, but further work both theoretically and experimentally must be performed to prove that these dually-doped samples can actually catalyze the excess DOS.

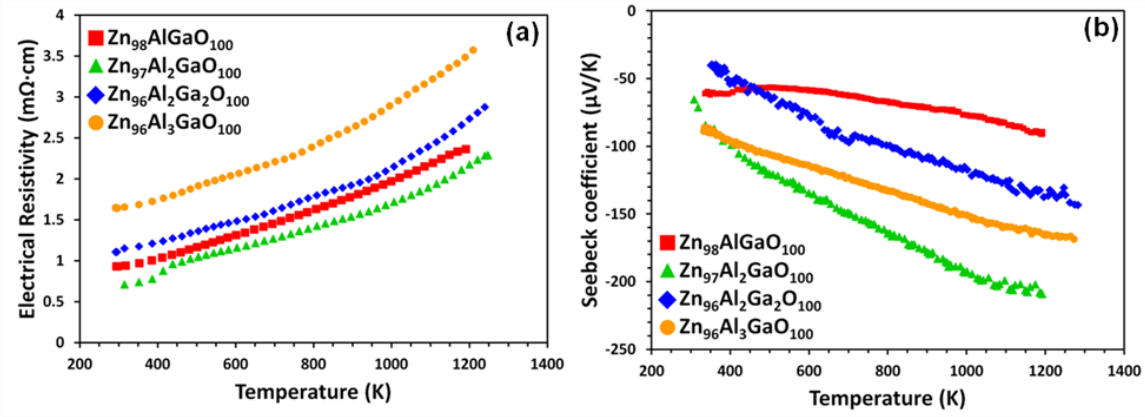

Figure 35. Plots indicating the variation of (a) electrical resistivity and (b) Seebeck coefficient of the dually-doped ZnO samples with temperature. All samples, except $Zn_{97}Al_2GaO_{100}$, exhibited an inverse proportionality between the Seebeck coefficient and electrical resistivity, characteristic of classical degenerate semiconductors. The lone discrepancy is attributed to resonant-level scattering of electrons in optimally-doped samples of $Zn_{97}Al_2GaO_{100}$.

Table 1. Properties of each $Zn_{100-x-y}Al_xGa_yO_{100}$ sample at 1073K including the carrier concentration (n), thermal conductivity (κ), electrical resistivity (ρ), Seebeck coefficient (S), and effective electron mass (m*).

Sample x,y	n (10^{20} cm^{-3})	κ (mW cm^{-1} K^{-1})	ρ (mΩ cm)	S (μV K^{-1})	m*/m_e
1,1	1.29	66.3	2.15	81	0.29
2,1	1.39	54.8	1.84	188	0.90
2,2	1.04	53.2	2.33	125	0.41
3,1	0.60	51.8	3.09	113	0.26

Thermal Transport

The thermal conductivity of the pellets was calculated from the values of thermal diffusivity (α), density (ρ), and specific heat (C_p) using the following relationship: $\kappa = \alpha\rho C_p$. It was observed that as the amount of Group-III dopant increased in the sample, the thermal conductivity was lowered (Figure 36a). A maximum 4-fold decrease in thermal conductivity at 300 K relative to single-crystalline ZnO is observed in these dually doped samples.[156] In addition, it was observed that nanostructuring as expected led to a decrease in the thermal conductivity. Use of nanostructures in the fabrication of the pellets led to at least 25% reduction in the thermal conductivity relative to their bulk counterparts at 1073 K.[69] Overall, alloy scattering, coupled with boundary scattering at the nanowire interfaces within the consolidated sample, can be attributed to these large decreases in thermal conductivity. The precipitated spinel phases also provide more interfaces and increase the phonon scattering within the samples as can be seen in the XRD (Figure 31) and TEM (Figure 33) analyses, thereby contributing to a reduction in the thermal conductivity of the samples. From these results, it can be concluded that this strategy for making ZnO alloy nanostructured thermoelectrics results in the lowest thermal conductivity reported to date for ZnO-based systems. The electronic thermal conductivity, κ_e, was calculated using the Wiedemann-Franz law, $\kappa_e = LT/\rho$, where L is the Lorenz number, T is the absolute temperature, and ρ is the electrical resistivity. For degenerate semiconductors, the Lorenz number varies as a function of the Fermi level resulting in values often orders of magnitude less than the free electron value of 2.44×10^{-8} $W\Omega K^{-2}$ for metals.[207] Therefore, it is necessary to calculate these values for each

composition due to varying chemical potentials. Assuming Umklapp scattering as the dominant process for this material system, the single parabolic band model can be used to calculate the Lorenz numbers as shown previously.[1, 207, 209] This results in values of L ranging from 1.66×10^{-8} to 2.08×10^{-8} $W\Omega K^{-2}$, much less than that for metals. The lattice thermal conductivity, κ_L, can be calculated from $\kappa = \kappa_e + \kappa_L$ and is plotted in Figure 36b as a function of temperature. U-processes are confirmed as the dominant phonon scattering mechanism as the lattice thermal conductivities are proportional to T^{-1} for all carrier concentrations. The slight deviations from this value can be attributed to alloy and interfacial scattering, specifically at lower temperatures where U-processes are not as dominant.

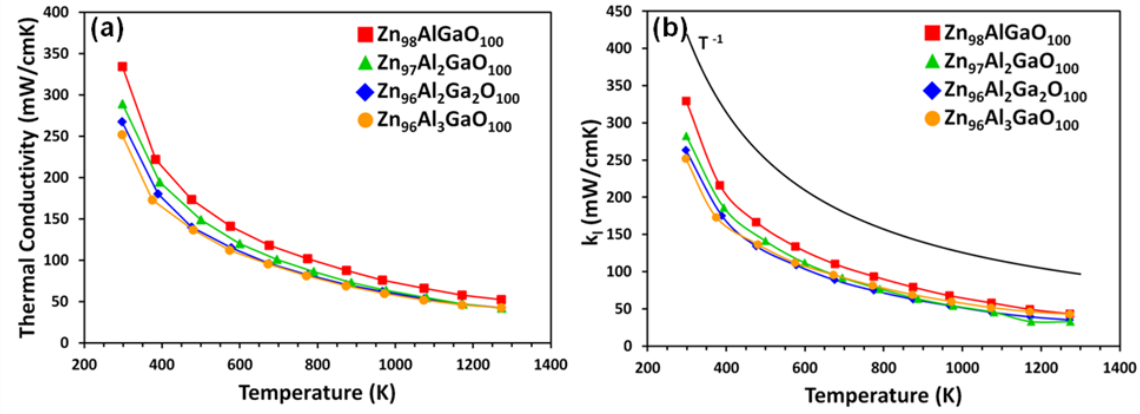

Figure 36. (a) A plot indicating the variation of the thermal conductivity of the dually doped ZnO nanowires pellets with temperature. The data indicated a reduction in the thermal conductivity with an increase in the dopant concentration. This is attributed to the creation of more phonon scattering centers with increasing dopant concentration. (b) A plot indicating the variation of the lattice thermal conductivity, k_L, with temperature. The lattice thermal conductivities of all the samples decayed with temperature proportional to T^{-1}, as expected in a degenerate semiconductor where U-processes dominate phonon scattering.

Total Efficiency

Plots indicating the variation of the zT values with temperature are shown in Figure 37. The zT of all samples increased with increasing temperature, as expected. The largest zT value measured was 0.60 at 1273 K for the sample with the composition with the largest effective mass, $Zn_{97}Al_2GaO_{100}$. This value is consistent with that previously reported,[69] and is the highest value experimentally reported to-date for ZnO alloys. Unfortunately, the previous report did not measure high temperature thermal conductivity or publish carrier concentration data to determine the differences in the amount of dopant added relative to the amount actually incorporated into the lattice. Due to the variations in pressing conditions, different amounts of the dopants could be incorporated relative to the reported work resulting in a slightly different composition with maximum zT. Nevertheless, the apparent anomalous result can be explained through band resonance that exists in both studies with similar amounts of dopant added to give the maximum zT of ~0.6. Overall, the results imply that a reduction in the lattice thermal conductivity by nanostructuring and alloying has a large effect on the overall thermoelectric performance. This in conjunction with resonant scattering enabled this high zT in the ZnO alloys.

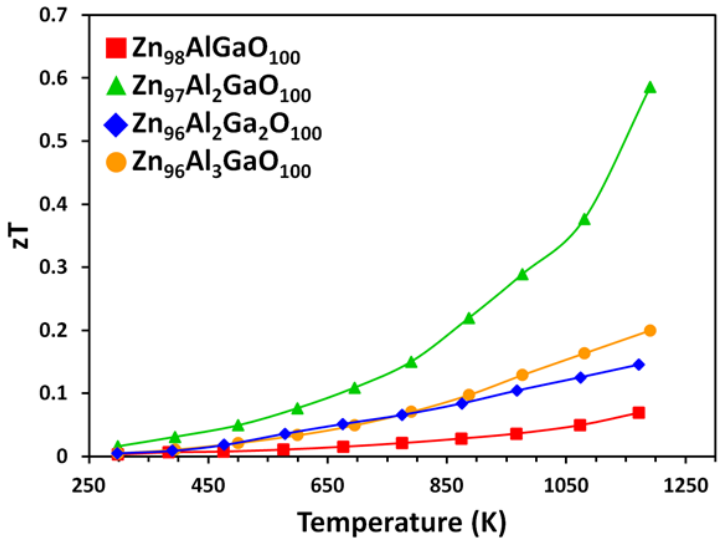

Figure 37. Plot indicating the zT variation with temperature of the dually-doped ZnO samples. A peak zT of 0.6 at 1273 K was achieved at an optimal doping composition of $Zn_{97}Al_2GaO_{100}$.

Conclusions

ZnO nanowire dually-doped alloys with aluminum and gallium were synthesized using spark plasma sintering. These nanobulk alloys were characterized for their thermoelectric properties, and a peak zT of 0.6 was observed at temperature of 1273 K in one of the compositions employed in this study, $Zn_{97}Al_2GaO_{100}$. This zT value is the highest experimentally reported to-date for any n-type oxide. The enhanced zT value of the $Zn_{97}Al_2GaO_{100}$ composition is attributed to resonance scattering, coupled with the effects of nanostructuring. Although oxide materials are still behind the state-of-the-art thermoelectric materials in terms of thermoelectric performance, they can be synthesized into modules at a much lower cost per Watt. Consequently, despite their lower

performance, these ZnO alloy thermoelectrics can be cost-competitive in the terrestrial market for waste-heat recovery.

CHAPTER IX

SUMMARY AND FUTURE WORK

Summary

Bulk assemblies of nanowires composed exclusively of earth abundant semiconductors with controlled diameters and surface chemistries were shown to greatly increase the thermoelectric performance of materials, especially when compared to their bulk counterparts. The performance increases shown for each of the material systems (Zn_3P_2 and ZnO) make them viable for future use in energy conversion devices, specifically thermoelectric modules (Table 2). In short, the prediction by Hicks and Dresselhaus that use of nanomorphology, specifically nanowires, results in an increase in the thermoelectric figure of merit was experimentally shown to be true. It was also realized that this performance increase is due to the preservation of nanowire morphology in these large-scale nanowire assemblies. It was postulated and experimentally verified that the mechanical flexible nature of the nanowires afforded their assembly into highly dense pellets, while also allowing for the retention of their morphologies within the pellets. Additionally, the increased reactivity of the nanowire surfaces, relative to the bulk, was combated by using an *in situ* vapor-phase functionalization technique to passivate the surfaces of the nanowires. This technique also allowed for tuning the interfacial chemistry of the nanowires within the pellets after their consolidation into bulk pellets. Such tuning of the interfacial chemistry further allowed for tuning the thermal and electrical transport through the nanowire pellets. By

completely maintaining the nanowire morphology in the nanobulk samples, higher thermoelectric performance was able to be realized. It was also confirmed that the gains observed in single nanowire devices also translate to the bulk scale.

The thermoelectric performance of the Zn_3P_2 nanowire system was shown to surpass that of previous published in bulk samples. Despite its lower zT-value, higher performance is possible with the selection of the ideal dopant to optimally tune its carrier concentration. Additionally, the large-scale nanowire synthesis procedure described is scalable to the industrial level, resulting in a potentially commercial process. The thermoelectric performance for the dually-doped ZnO nanowire system was compared against state-of-the-art thermoelectric materials and found to be comparable to them in efficiency. When factoring in cost specific power and weight specific power, it was shown that the ZnO alloy nanowire system was superior. The high zT of 0.65 at 1273 K is the highest ever achieved for an n-type oxide, and now can be a viable option to go along with the current p-type oxide materials to make a complete thermoelectric couple.

Table 2. Thermoelectric performance (zT) summary of materials in this dissertation

Nanowire Material	**zT**
Zn_3P_2	3.6×10^{-4}
BDT-Zn_3P_2	3.3×10^{-3}
ZnO	0.6

Future Work

Based on the conclusion of this work, it is believed that the future work should focus on improving the thermoelectric performance of the Zn_3P_2 nanowires further by optimally doping them to the degenerate state. Secondly, use of organic molecule functionalized, the optimally-doped ZnO nanowires for the fabrication of thermoelectrics should be performed to further reduce the thermal conductivity of the nanobulk pellet and increase the zT. Thirdly, the quantitative effect of nanowire diameter on the thermoelectric performance should be deduced. Deducing this effect for a given material system will be beneficial for future nanowire thermoelectric research. Finally, the application of these nanowire synthesis and assembly techniques to other material systems that are known to be good thermoelectric materials, such as $CoSb_3$[210] and Mg_2Si[1] could result in a large increase in their thermoelectric performance. If the trends of the materials utilized in this dissertation hold, it should be possible to see zTs on the order of 1.5 out of more well-known thermoelectric earth abundant semiconductors in the near future.

REFERENCES

1. Bux, S. K.; Yeung, M. T.; Toberer, E. S.; Snyder, G. J.; Kaner, R. B.; Fleurial, J.-P., Mechanochemical synthesis and thermoelectric properties of high quality magnesium silicide. *Journal of Materials Chemistry* **2011,** *21*, 12259-12266.

2. Vining, C. B., An inconvenient truth about thermoelectrics. *Nat. Mater.* **2009,** *8*, 83-85.

3. Caillat, T.; Fleurial, J. P.; Borshchevsky, A., Preparation and thermoelectric properties of semiconducting Zn_4Sb_3. *Journal of Physics and Chemistry of Solids* **1997,** *58*, 1119-1125.

4. Min, G.; Rowe, D. M., "Symbiotic" application of thermoelectric conversion for fluid preheating/power generation. *Energy Conversion and Management* **2002,** *43*, 221-228.

5. Qiu, K.; Hayden, A. C. S., A natural-gas-fired thermoelectric power generation system. *Journal of Electronic Materials* **2009,** *38*, 1315-1319.

6. Knowles, C. B.; Lee, H., Optimized working conditions for a thermoelectric generator as a topping cycle for gas turbines. *Journal of Applied Physics* **2012,** *112*, 073515-8.

7. Yazawa, K.; Koh, Y. R.; Shakouri, A., Optimization of thermoelectric topping combined steam turbine cycles for energy economy. *Applied Energy* **2013,** *109*, 1-9.

8. Hicks, L. D.; Dresselhaus, M. S., Thermoelectric figure of merit of a one-dimensional conductor. *Phys. Rev. B* **1993,** *47*, 16631-16634.

9. Mingo, N., Calculation of Si nanowire thermal conductivity using complete phonon dispersion relations. *Phys. Rev. B* **2003,** *68*, 113308.

10. Brockway, L.; Pendyala, C.; Jasinski, J.; Sunkara, M. K.; Vaddiraju, S., A postsynthesis decomposition strategy for Group III-nitride quantum wires. *Cryst. Growth Des.* **2011,** *11*, 4559-4564.

11. Brockway, L.; Van Laer, M.; Kang, Y.; Vaddiraju, S., Large-scale synthesis and in situ functionalization of Zn_3P_2 and Zn_4Sb_3 nanowire powders. *Physical Chemistry Chemical Physics* **2013,** *15*, 6260-6267.

12. Lance, B.; Venkata, V.; Hasti, A.-A.; Reza, S.-Y.; Sreeram, V., Thermoelectric properties of large-scale Zn_3P_2 nanowire assemblies. *Nanotechnology* **2014,** *25*, 145401.

13. Briggs, C. K.; Borg, I. Y. *US energy flow, 1982*; UCID-19227-82.

14. LLNL; USDoE, Estimated U.S. energy use in 2011: ~97.3 Quads. **October 2012**, LLNL-MI-410527.

15. Snyder, G. J.; Toberer, E. S., Complex thermoelectric materials. *Nat. Mater.* **2008,** *7*, 105-114.

16. Nolas, G. S.; Morelli, D. T.; Tritt, T. M., Skutterudites: A phonon-glass-electron crystal approach to advanced thermoelectric energy conversion applications. *Annu. Rev. Mater. Sci.* **1999,** *29*, 89-116.

17. Snyder, G. J.; Christensen, M.; Nishibori, E.; Caillat, T.; Iversen, B. B., Disordered zinc in Zn_4Sb_3 with phonon-glass and electron-crystal thermoelectric properties. *Nat. Mater.* **2004,** *3*, 458-463.

18. Dresselhaus, M. S.; Chen, G.; Tang, M. Y.; Yang, R. G.; Lee, H.; Wang, D. Z.; Ren, Z. F.; Fleurial, J. P.; Gogna, P., New directions for low-dimensional thermoelectric materials. *Adv. Mater.* **2007,** *19*, 1043-1053.

19. Ren, S.; Zhao, N.; Crawford, S. C.; Tambe, M.; Bulović, V.; Gradečak, S., Heterojunction photovoltaics using GaAs nanowires and conjugated polymers. *Nano Letters* **2010,** *11*, 408-413.

20. Kanatzidis, M. G., Nanostructured thermoelectrics: the new paradigm?. *Chemistry of Materials* **2009,** *22*, 648-659.

21. Shakouri, A., Recent developments in semiconductor thermoelectric physics and materials. *Annual Review of Materials Research* **2011,** *41*, 399-431.

22. Boukai, A. I.; Bunimovich, Y.; Tahir-Kheli, J.; Yu, J. K.; Goddard, W. A.; Heath, J. R., Silicon nanowires as efficient thermoelectric materials. *Nature* **2008,** *451*, 168-171.

23. Hochbaum, A. I.; Chen, R. K.; Delgado, R. D.; Liang, W. J.; Garnett, E. C.; Najarian, M.; Majumdar, A.; Yang, P. D., Enhanced thermoelectric performance of rough silicon nanowires. *Nature* **2008,** *451*, 163-U5.

24. Zhou, J.; Jin, C.; Seol, J. H.; Li, X.; Shi, L., Thermoelectric properties of individual electrodeposited bismuth telluride nanowires. *Applied Physics Letters* **2005,** *87*, 133109.

25. Li, L.; Yang, Y. W.; Huang, X. H.; Li, G. H.; Ang, R.; Zhang, L. D., Fabrication and electronic transport properties of Bi nanotube arrays. *Applied Physics Letters* **2006,** *88*, 103119.

26. Boukai, A.; Xu, K.; Heath, J. R., Size-dependent transport and thermoelectric properties of individual polycrystalline bismuth nanowires. *Adv. Mater.* **2006,** *18*, 864-869.

27. Zdanowicz, T.; Rodziewicz, T.; Zabkowska-Waclawek, M., Theoretical analysis of the optimum energy band gap of semiconductors for fabrication of solar cells for applications in higher latitudes locations. *Solar Energy Materials and Solar Cells* **2005,** *87*, 757-769.

28. Shockley, W.; Queisser, H. J., Detailed balance limit of efficiency of P-N junction solar cells. *Journal of Applied Physics* **1961,** *32*, 510.

29. Taylor, S. R., Abundance of chemical elements in the continental crust - a new table. *Geochim. Cosmochim. Acta* **1964,** *28*, 1273-1285.

30. Hsu, C. H.; Han, B. C.; Liu, M. Y.; Yeh, C. Y.; Casida, J. E., Phosphine-induced oxidative damage in rats: Attenuation by melatonin. *Free Radic. Biol. Med.* **2000,** *28*, 636-642.

31. Chen, G.; Visbeck, S. B.; Law, D. C.; Hicks, R. F., Structure-sensitive oxidation of the indium phosphide (001) surface. *Journal of Applied Physics* **2002,** *91*, 9362-9367.

32. Soukiassian, P.; Bakshi, M. H.; Starnberg, H. I.; Bommannavar, A. S.; Hurych, Z., Precursor molecular-oxygen state in the initial catalytic oxidation of the InP(110) surface modified by alkali metals. *Phys. Rev. B* **1988,** *37*, 6496.

33. Bashouti, M. Y.; Stelzner, T.; Berger, A.; Christiansen, S.; Haick, H., Chemical passivation of silicon nanowires with C-1-C-6 alkyl chains through covalent Si-C bonds. *J. Phys. Chem. C* **2008,** *112*, 19168-19172.

34. Hanrath, T.; Korgel, B. A., Chemical surface passivation of Ge nanowires. *J. Am. Chem. Soc.* **2004,** *126*, 15466-15472.

35. Bhushan, M.; Catalano, A., Polycrystalline Zn_3P_2 Schottky-barrier solar-cells. *Applied Physics Letters* **1981,** *38*, 39-41.

36. Savadogo, O., Chemically and electrochemically deposited thin films for solar energy materials. *Solar Energy Materials and Solar Cells* **1998,** *52*, 361-388.

37. Baxter, J. B.; Aydil, E. S., Nanowire-based dye-sensitized solar cells. *Applied Physics Letters* **2005,** *86*.

38. Law, M.; Greene, L. E.; Johnson, J. C.; Saykally, R.; Yang, P. D., Nanowire dye-sensitized solar cells. *Nat. Mater.* **2005,** *4*, 455-459.

39. Toberer, E. S.; Sasaki, K. A.; Chisholm, C. R. I.; Haile, S. M.; Goddard, W. A.; Snyder, G. J., Local structure of interstitial Zn in β-Zn_4Sb_3. *physica status solidi (RRL) – Rapid Research Letters* **2007,** *1*, 253-255.

40. Fergus, J. W., Oxide materials for high temperature thermoelectric energy conversion. *Journal of the European Ceramic Society* **2012,** *32*, 525-540.

41. Ohtaki, M.; Tsubota, T.; Eguchi, K.; Arai, H., High-temperature thermoelectric properties of $(Zn_{1-x}Al_x)O$. *Journal of Applied Physics* **1996,** *79*, 1816-1818.

42. Kwon, O. J.; Jo, W.; Ko, K.-E.; Kim, J.-Y.; Bae, S.-H.; Koo, H.; Jeong, S.-M.; Kim, J.-S.; Park, C., Thermoelectric properties and texture evaluation of $Ca_3Co_4O_9$ prepared by a cost-effective multisheet cofiring technique. *J Mater Sci* **2011,** *46*, 2887-2894.

43. Lu, Q. M.; Zhang, J. X.; Zhang, Q. Y.; Liu, Y. Q.; Liu, D. M. In *Improved thermoelectric properties of $Ca_{3-x}Ba_xCo_4O_9$ (x=0~0.4) bulks by sol-gel and SPS method*, Thermoelectrics, 2006. ICT '06. 25th International Conference on, 6-10 Aug. 2006, 2006; pp 66-69.

44. Wang, Y.; Sui, Y.; Cheng, J.; Wang, X.; Su, W., Comparison of the high temperature thermoelectric properties for Ag-doped and Ag-added $Ca_3Co_4O_9$. *Journal of Alloys and Compounds* **2009,** *477*, 817-821.

45. Van Nong, N.; Pryds, N.; Linderoth, S.; Ohtaki, M., Enhancement of the thermoelectric performance of p-type layered oxide $Ca_3Co_4O_{9+\delta}$ through heavy doping and metallic nanoinclusions. *Adv. Mater.* **2011,** *23*, 2484-2490.

46. Zhang, F. P.; Lu, Q. M.; Zhang, J. X., Synthesis and high temperature thermoelectric properties of $Ba_xAg_yCa_{3-x-y}Co_4O_9$ compounds. *Journal of Alloys and Compounds* **2009,** *484*, 550-554.

47. Wang, Y.; Sui, Y.; Wang, X.; Su, W.; Liu, X., Enhanced high temperature thermoelectric characteristics of transition metals doped $Ca_3Co_4O_{9+\delta}$ by cold high-pressure fabrication. *Journal of Applied Physics* **2010,** *107*, 033708-9.

48. Wang, L.; Wang, M.; Zhao, D., Thermoelectric properties of c-axis oriented Ni-substituted $NaCoO_2$ thermoelectric oxide by the citric acid complex method. *Journal of Alloys and Compounds* **2009,** *471*, 519-523.

49. Tsai, P. H.; Norby, T.; Tan, T. T.; Donelson, R.; Chen, Z. D.; Li, S., Correlation of oxygen vacancy concentration and thermoelectric properties in $Na_{0.73}CoO_{2-\delta}$. *Applied Physics Letters* **2010,** *96*, 141905-3.

50. Nagira, T.; Ito, M.; Katsuyama, S.; Majima, K.; Nagai, H., Thermoelectric properties of $(Na_{1-y}M_y)_xCo_2O_4$ (M=K, Sr, Y, Nd, Sm and Yb; y=0.01∼0.35). *Journal of Alloys and Compounds* **2003,** *348*, 263-269.

51. Ito, M.; Furumoto, D., Microstructure and thermoelectric properties of $Na_xCo_2O_4$/Ag composite synthesized by the polymerized complex method. *Journal of Alloys and Compounds* **2008,** *450*, 517-520.

52. Wang, Y.; Lee, K. H.; Ohta, H.; Koumoto, K., Thermoelectric properties of electron doped $SrO(SrTiO_3)_n$ (n = 1,2) ceramics. *Journal of Applied Physics* **2009,** *105*, 103701-6.

53. Wang, N.; He, H.; Ba, Y.; Wan, C.; Koumoto, K., Thermoelectric properties of Nb-doped $SrTiO_3$ ceramics enhanced by potassium titanate nanowires addition. *Journal of the Ceramic Society of Japan* **2010,** *118*, 1098-1101.

54. Kato, K.; Yamamoto, M.; Ohta, S.; Muta, H.; Kurosaki, K.; Yamanaka, S.; Iwasaki, H.; Ohta, H.; Koumoto, K., The effect of Eu substitution on thermoelectric properties of $SrTi_{0.8}Nb_{0.2}O_3$. *Journal of Applied Physics* **2007,** *102*, 116107-3.

55. Ravichandran, J.; Siemons, W.; Oh, D. W.; Kardel, J. T.; Chari, A.; Heijmerikx, H.; Scullin, M. L.; Majumdar, A.; Ramesh, R.; Cahill, D. G., High-temperature thermoelectric response of double-doped $SrTiO_3$ epitaxial films. *Physical Review B* **2010,** *82*, 165126.

56. Shang, P.-P.; Zhang, B.-P.; Liu, Y.; Li, J.-F.; Zhu, H.-M., Preparation and thermoelectric properties of La-Doped $SrTiO_3$ ceramics. *Journal of Electronic Materials* **2011,** *40*, 926-931.

57. Kikuchi, A.; Okinaka, N.; Akiyama, T., A large thermoelectric figure of merit of La-doped $SrTiO_3$ prepared by combustion synthesis with post-spark plasma sintering. *Scripta Materialia* **2010,** *63*, 407-410.

58. Isobe, S.; Tani, T.; Masuda, Y.; Seo, W. S.; Koumoto, K., Thermoelectric performance of yttrium-substituted $(ZnO)_5In_2O_3$ improved through ceramic texturing. *Japanese Journal of Applied Physics Part 1-Regular Papers Short Notes & Review Papers* **2002,** *41*, 731-732.

59. Masuda, Y.; Ohta, M.; Seo, W. S.; Pitschke, W.; Koumoto, K., Structure and thermoelectric transport properties of isoelectronically substituted $(ZnO)_5In_2O_3$. *Journal of Solid State Chemistry* **2000,** *150*, 221-227.

60. Kazeoka, M.; Hiramatsu, H.; Seo, W. S.; Koumoto, K., Improvement in thermoelectric properties of $(ZnO)_5In_2O_3$ through partial substitution of yttrium for indium. *Journal of Materials Research* **1998,** *13*, 523-526.

61. Ohta, H.; Seo, W. S.; Koumoto, K., Thermoelectric properties of homologous compounds in the ZnO-In2O3 system. *Journal of the American Ceramic Society* **1996,** *79*, 2193-2196.

62. Cai, K. F.; Muller, E.; Drasar, C.; Mrotzek, A., Preparation and thermoelectric properties of Al-doped ZnO ceramics. *Materials Science and Engineering B-Solid State Materials for Advanced Technology* **2003,** *104*, 45-48.

63. Tsubota, T.; Ohtaki, M.; Eguchi, K.; Arai, H., Thermoelectric properties of Al-doped ZnO as a promising oxide material for high-temperature thermoelectric conversion. *Journal of Materials Chemistry* **1997,** *7*, 85-90.

64. Qu, X.; Wang, W.; Lv, S.; Jia, D., Thermoelectric properties and electronic structure of Al-doped ZnO. *Solid State Communications* **2011,** *151*, 332-336.

65. Ohtaki, M.; Tsubota, T.; Eguchi, K.; Arai, H., High-temperature thermoelectric properties of $(Zn_{1-x}Al_x)O$. *Journal of Applied Physics* **1996,** *79*, 1816-1818.

66. Tsubota, T.; Ohtaki, M.; Eguchi, K.; Arai, H., Transport properties and thermoelectric performance of $(Zn_{1-y}Mg_y)_{(1-x)}Al_xO$. *Journal of Materials Chemistry* **1998,** *8*, 409-412.

67. Katsuyama, S.; Takagi, Y.; Ito, M.; Majima, K.; Nagai, H.; Sakai, H.; Yoshimura, K.; Kosuge, K., Thermoelectric properties of $(Zn_{1-y}Mg_y)_{(1-x)}Al_xO$ ceramics prepared by the polymerized complex method. *Journal of Applied Physics* **2002,** *92*, 1391-1398.

68. Yamaguchi, H.; Chonan, Y.; Oda, M.; Komiyama, T.; Aoyama, T.; Sugiyama, S., Thermoelectric properties of ZnO ceramics co-doped with Al and transition metals. *Journal of Electronic Materials* **2011,** *40*, 723-727.

69. Ohtaki, M.; Araki, K.; Yamamoto, K., High thermoelectric performance of dually doped ZnO ceramics. *Journal of Electronic Materials* **2009,** *38*, 1234-1238.

70. Shen, G. Z.; Bando, Y.; Hu, J. Q.; Golberg, D., Single-crystalline trumpetlike zinc phosphide nanostructures. *Applied Physics Letters* **2006,** *88*.

71. Yang, R. S.; Chueh, Y. L.; Morber, J. R.; Snyder, R.; Chou, L. J.; Wang, Z. L., Single-crystalline branched zinc phosphide nanostructures: synthesis, properties, and optoelectronic devices. *Nano Letters* **2007,** *7*, 269-275.

72. Wu, P. C.; Sun, T.; Dai, Y.; Sun, Y. H.; Ye, Y.; Dai, L., Novel type-II Zn_3P_2/ZnO core/shell nanowires: synthesis, characteristic, and photoluminescence properties. *Cryst. Growth Des.* **2011,** *11*, 1417-1421.

73. Sun, T.; Wu, P. C.; Guo, Z. D.; Dai, Y.; Meng, H.; Fang, X. L.; Shi, Z. J.; Dai, L.; Qin, G. G., Synthesis and characterization of Zn_3P_2/ZnS core/shell nanowires. *Phys. Lett. A* **2011,** *375*, 2118-2121.

74. Liu, Y.-B.; Zhou, S.-M.; Yuan, X.-Y.; Lou, S.-Y.; Gao, T.; Shi, X.-J.; Wu, X.-P., Synthesis and high-performance thermoelectric properties of β-Zn_4Sb_3 nanowires. *Materials Letters* **2012,** *84*, 116-119.

75. Agarwal, R.; Lieber, C. M., Semiconductor nanowires: optics and optoelectronics. *Appl. Phys. A-Mater. Sci. Process.* **2006,** *85*, 209-215.

76. Chen, C. C.; Yeh, C. C., Large-scale catalytic synthesis of crystalline gallium nitride nanowires. *Adv. Mater.* **2000,** *12*, 738.

77. Duan, X. F.; Lieber, C. M., Laser-assisted catalytic growth of single crystal GaN nanowires. *J. Am. Chem. Soc.* **2000,** *122*, 188-189.

78. Duan, X. F.; Lieber, C. M., General synthesis of compound semiconductor nanowires. *Adv. Mater.* **2000,** *12*, 298-302.

79. Wang, D.; Qian, F.; Yang, C.; Zhong, Z. H.; Lieber, C. M., Rational growth of branched and hyperbranched nanowire structures. *Nano Letters* **2004,** *4*, 871-874.

80. Zhong, Z. H.; Qian, F.; Wang, D. L.; Lieber, C. M., Synthesis of p-type gallium nitride nanowires for electronic and photonic nanodevices. *Nano Letters* **2003,** *3*, 343-346.

81. Goldberger, J.; He, R. R.; Zhang, Y. F.; Lee, S. W.; Yan, H. Q.; Choi, H. J.; Yang, P. D., Single-crystal gallium nitride nanotubes. *Nature* **2003,** *422*, 599-602.

82. Shi, W. S.; Zheng, Y. F.; Wang, N.; Lee, C. S.; Lee, S. T., A general synthetic route to III-V compound semiconductor nanowires. *Adv. Mater.* **2001,** *13*, 591.

83. Shi, W. S.; Zheng, Y. F.; Wang, N.; Lee, C. S.; Lee, S. T., Microstructures of gallium nitride nanowires synthesized by oxide-assisted method. *Chem. Phys. Lett.* **2001,** *345*, 377-380.

84. Chandrasekaran, H.; Sunkara, M. K., Growth of gallium nitride textured films and nanowires on polycrystalline substrates at sub-atmospheric pressures. In *Gan and Related Alloys-2001*, Northrup, J. E.; Neugebauer, J.; Look, D. C.; Chichibu, S. F.; Riechert, H., Eds. Materials Research Society: Warrendale, 2002; Vol. 693, pp 159-164.

85. Chin, A. H.; Vaddiraju, S.; Maslov, A. V.; Ning, C. Z.; Sunkara, M. K.; Meyyappan, M., Near-infrared semiconductor subwavelength-wire lasers. *Applied Physics Letters* **2006,** *88*.

86. Li, H. W.; Chin, A. H.; Sunkara, M. K., Direction-dependent homoepitaxial growth of GaN nanowires. *Adv. Mater.* **2006,** *18*, 216.

87. Stach, E. A.; Pauzauskie, P. J.; Kuykendall, T.; Goldberger, J.; He, R. R.; Yang, P. D., Watching GaN nanowires grow. *Nano Letters* **2003,** *3*, 867-869.

88. Vaddiraju, S.; Mohite, A.; Chin, A.; Meyyappan, M.; Sumanasekera, G.; Alphenaar, B. W.; Sunkara, M. K., Mechanisms of 1D crystal growth in reactive vapor transport: indium nitride nanowires. *Nano Letters* **2005,** *5*, 1625-1631.

89. Vaddiraju, S.; Sunkara, M. K.; Chin, A. H.; Ning, C. Z.; Dholakia, G. R., Synthesis of Group-III antimonide nanowires. *J. Phys. Chem. C* **2007,** *111*, 7339-7347.

90. Allen, J. E.; Hemesath, E. R.; Perea, D. E.; Lensch-Falk, J. L.; Li, Z. Y.; Yin, F.; Gass, M. H.; Wang, P.; Bleloch, A. L.; Palmer, R. E.; Lauhon, L. J., High-resolution detection of Au catalyst atoms in Si nanowires. *Nature Nanotechnology* **2008,** *3*, 168-173.

91. Hannon, J. B.; Kodambaka, S.; Ross, F. M.; Tromp, R. M., The influence of the surface migration of gold on the growth of silicon nanowires. *Nature* **2006,** *440*, 69-71.

92. Brus, L., Electronic wave-functions in semiconductor clusters - experiment and theory. *Journal of Physical Chemistry* **1986,** *90*, 2555-2560.

93. Preschilla, N.; Major, S.; Kumar, N.; Samajdar, I.; Srinivasa, R. S., Nanocrystalline gallium nitride thin films. *Applied Physics Letters* **2000,** *77*, 1861-1863.

94. Yoon, J. W.; Sasaki, T.; Roh, C. H.; Shim, S. H.; Shim, K. B.; Koshizaki, N., Quantum confinement effect of nanocrystalline GaN films prepared by pulsed-laser ablation under various Ar pressures. *Thin Solid Films* **2005,** *471*, 273-276.

95. Hong, S.; Reifenberger, R.; Tian, W.; Datta, S.; Henderson, J. I.; Kubiak, C. P., Molecular conductance spectroscopy of conjugated, phenyl-based molecules on Au(111): the effect of end groups on molecular conduction. *Superlattices and Microstructures* **2000,** *28*, 289-303.

96. Larsson, J. A.; Nolan, M.; Greer, J. C., Interactions between thiol molecular linkers and the Au-13 nanoparticle. *J. Phys. Chem. B* **2002,** *106*, 5931-5937.

97. Li, Z. Y.; Chang, S. C.; Williams, R. S., Self-assembly of alkanethiol molecules onto platinum and platinum oxide surfaces. *Langmuir* **2003,** *19*, 6744-6749.

98. Murty, K.; Venkataramanan, M.; Pradeep, T., Self-assembled monolayers of 1,4-benzenedimethanethiol on polycrystalline silver and gold films: An investigation of structure, stability, dynamics, and reactivity. *Langmuir* **1998,** *14*, 5446-5456.

99. Thomas, K. G.; Barazzouk, S.; Ipe, B. I.; Joseph, S. T. S.; Kamat, P. V., Uniaxial plasmon coupling through longitudinal self-assembly of gold nanorods. *J. Phys. Chem. B* **2004,** *108*, 13066-13068.

100. Sadik, P. W.; Pearton, S. J.; Norton, D. P.; Lambers, E.; Ren, F., Functionalizing Zn- and O-terminated ZnO with thiols. *Journal of Applied Physics* **2007,** *101*.

101. Singh, J.; Im, J.; Whitten, J. E.; Soares, J. W.; Steeves, D. M., Chemisorption of a thiol-functionalized ruthenium dye on zinc oxide nanoparticles: implications for dye-sensitized solar cells. *Chem. Phys. Lett.* **2010,** *497*, 196-199.

102. Singh, J.; Im, J.; Whitten, J. E.; Soares, J. W.; Meehan, A. M.; Steeves, D. M., Adsorption of mercaptosilanes on nanocrystalline and single crystal zinc oxide surfaces. In *Nanophotonic Materials V*, Gaburro, Z.; Cabrini, S.; Talapin, D., Eds. Spie-Int Soc Optical Engineering: Bellingham, 2008; Vol. 7030, pp T300-T300.

103. Budz, H. A.; Biesinger, M. C.; LaPierre, R. R., Passivation of GaAs by octadecanethiol self-assembled monolayers deposited from liquid and vapor phases. *Journal of Vacuum Science & Technology B* **2009,** *27*, 637-648.

104. Budz, H. A.; LaPierre, R. R., Properties of octadecanethiol self-assembled monolayers deposited on GaAs from liquid and vapor phases. *Journal of Vacuum Science & Technology A* **2008,** *26*, 1425-1431.

105. Sarigiannidis, C.; Koutsona, M.; Petrou, A.; Mountziaris, T. J., Vapor-phase synthesis and surface passivation of ZnSe nanocrystals. *J. Nanopart. Res.* **2006,** *8*, 533-542.

106. Holmberg, V. C.; Korgel, B. A., Corrosion Resistance of Thiol- and Alkene-Passivated Germanium Nanowires. *Chemistry of Materials* **2010,** *22*, 3698-3703.

107. Bux, S. K.; Blair, R. G.; Gogna, P. K.; Lee, H.; Chen, G.; Dresselhaus, M. S.; Kaner, R. B.; Fleurial, J.-P., Nanostructured bulk silicon as an effective thermoelectric material. *Advanced Functional Materials* **2009,** *19*, 2445-2452.

108. Ikeda, T.; Haile, S. M.; Ravi, V. A.; Azizgolshani, H.; Gascoin, F.; Snyder, G. J., Solidification processing of alloys in the pseudo-binary PbTe–Sb_2Te_3 system. *Acta Materialia* **2007,** *55*, 1227-1239.

109. Ikeda, T.; Collins, L. A.; Ravi, V. A.; Gascoin, F. S.; Haile, S. M.; Snyder, G. J., Self-assembled nanometer lamellae of thermoelectric PbTe and Sb_2Te_3 with epitaxy-like interfaces. *Chemistry of Materials* **2007,** *19*, 763-767.

110. Ikeda, T.; Ravi, V. A.; Snyder, G. J., Formation of Sb_2Te_3 Widmanstätten precipitates in thermoelectric PbTe. *Acta Materialia* **2009,** *57*, 666-672.

111. Lin, H. T.; Katoh, Y.; Fox, K. M.; Belharouak, I., *Ceramic Materials for Energy Applications: Ceramic Engineering and Science Proceedings*. Wiley 2011.

112. Upadhyaya, G. S., *Powder Metallurgy Technology*. Cambridge International Science Publishing 1997.

113. Sopicka-Lizer, M., *High-Energy Ball Milling: Mechanochemical Processing of Nanopowders*. Elsevier Science 2010.

114. Euler, F., Simple geometric model for the effect of porosity on material constants. *Journal of Applied Physics* **1957,** *28*, 1342-1345.

115. Takashiri, M.; Miyazaki, K.; Tanaka, S.; Kurosaki, J.; Nagai, D.; Tsukamoto, H., Effect of grain size on thermoelectric properties of n-type nanocrystalline bismuth-telluride based thin films. *Journal of Applied Physics* **2008,** *104*.

116. Fang, H.; Feng, T.; Yang, H.; Ruan, X.; Wu, Y., Synthesis and thermoelectric properties of compositional-modulated lead telluride–bismuth telluride nanowire heterostructures. *Nano Letters* **2013,** *13*, 2058-2063.

117. Zhang, G.; Fang, H.; Yang, H.; Jauregui, L. A.; Chen, Y. P.; Wu, Y., Design principle of telluride-based nanowire heterostructures for potential thermoelectric applications. *Nano Letters* **2012,** *12*, 3627-3633.

118. Kumar, V.; Kim, J. H.; Pendyala, C.; Chernomordik, B.; Sunkara, M. K., Gas-Phase, Bulk production of metal oxide nanowires and nanoparticles using a

microwave plasma jet reactor. *The Journal of Physical Chemistry C* **2008,** *112*, 17750-17754.

119. Silverstein, R. R. M.; Webster, F. X.; Kiemle, D. J., *The Spectrometric Identification of Organic Compounds*. John Wiley & Sons Australia, Limited 2005.

120. van der Heide, P., *X-ray Photoelectron Spectroscopy: An Introduction to Principles and Practices*. Wiley 2011.

121. Thomas, G.; Fulrath, R. M.; Fisher, R. M., *Electron Microscopy and Structure of Materials: Proceedings*. University of California Press 1972.

122. Williams, D. B.; Carter, C. B., *Transmission Electron Microscopy: A Textbook for Materials Science*. Springer 2009.

123. Cullity, B. D.; Stock, S. R., *Elements of X-Ray Diffraction*. Prentice Hall 2001.

124. Tkachenko, N. V., *Optical Spectroscopy: Methods and Instrumentations*. Elsevier Science 2006.

125. Rowe, D. M., *CRC Handbook of Thermoelectrics*. Taylor & Francis 1995.

126. Rowe, D. M., *Thermoelectrics Handbook: Macro to Nano*. Taylor & Francis 2010.

127. Wood, C.; Lockwood, A.; Chmielewski, A.; Parker, J.; Zoltan, A., High temperature Hall-effect apparatus. *Review of Scientific Instruments* **1984,** *55*, 110-113.

128. Wood, C.; Zoltan, D.; Stapfer, G., Measurement of Seebeck coefficient using a light pulse. *Review of Scientific Instruments* **1985,** *56*, 719-722.

129. Morales, A. M.; Lieber, C. M., A laser ablation method for the synthesis of crystalline semiconductor nanowires. *Science* **1998,** *279*, 208.

130. Guichard, A. R.; Barsic, D. N.; Sharma, S.; Kamins, T. I.; Brongersma, M. L., Tunable light emission from quantum-confined excitons in $TiSi_2$-catalyzed silicon nanowires. *Nano Letters* **2006,** *6*, 2140-2144.

131. Ahrenkiel, S. P.; Micic, O. I.; Miedaner, A.; Curtis, C. J.; Nedeljkovic, J. M.; Nozik, A. J., Synthesis and characterization of colloidal InP quantum rods. *Nano Letters* **2003,** *3*, 833-837.

132. Holmes, J. D.; Johnston, K. P.; Doty, R. C.; Korgel, B. A., Control of thickness and orientation of solution-grown silicon nanowires. *Science* **2000,** *287*, 1471.

133. Hanrath, T.; Korgel, B. A., Quantum confinement effects in germanium nanowires studied by electron energy loss spectroscopy (EELS). In *Physical Chemistry of Interfaces and Nanomaterials Iii*, Hartland, G. V.; Zhu, X. Y., Eds.2004; Vol. 5513, pp 40-47.

134. Hanrath, T.; Korgel, B. A., A comprehensive study of electron energy losses in Ge nanowires. *Nano Letters* **2004,** *4*, 1455-1461.

135. Grebinski, J. W.; Hull, K. L.; Zhang, J.; Kosel, T. H.; Kuno, M., Solution-based straight and branched CdSe nanowires. *Chemistry of Materials* **2004,** *16*, 5260-5272.

136. Yu, H.; Li, J.; Loomis, R. A.; Wang, L.-W.; Buhro, W. E., Two- versus three-dimensional quantum confinement in indium phosphide wires and dots. *Nat Mater* **2003,** *2*, 517-520.

137. Yu, H.; Li, J.; Loomis, R. A.; Gibbons, P. C.; Wang; Buhro, W. E., Cadmium selenide quantum wires and the transition from 3D to 2D confinement. *J. Am. Chem. Soc.* **2003,** *125*, 16168-16169.

138. Dong, A. G.; Wang, F. D.; Daulton, T. L.; Buhro, W. E., Solution-liquid-solid (SLS) growth of ZnSe-ZnTe quantum wires having axial heterojunctions. *Nano Letters* **2007,** *7*, 1308-1313.

139. Wang, F. D.; Yu, H.; Jeong, S. H.; Pietryga, J. M.; Hollingsworth, J. A.; Gibbons, P. C.; Buhro, W. E., The scaling of the effective band gaps in indium arsenide quantum dots and wires. *ACS Nano* **2008,** *2*, 1903-1913.

140. Xi, G.; Ye, J., Ultrathin SnO_2 nanorods: template- and surfactant-free solution phase synthesis, growth mechanism, optical, gas-sensing, and surface adsorption properties. *Inorganic Chemistry* **2010,** *49*, 2302-2309.

141. Wang, F.; Dong, A.; Sun, J.; Tang, R.; Yu, H.; Buhro, W. E., Solution−liquid−solid growth of semiconductor nanowires. *Inorganic Chemistry* **2006,** *45*, 7511-7521.

142. Erenburg, S. B.; et al., Quantum dots microstructure by XAFS spectroscopy: GaN/AlN system depending on preparation conditions. *Journal of Physics: Conference Series* **2006,** *41*, 261.

143. Grandjean, N.; Massies, J.; Semond, F.; Karpov, S. Y.; Talalaev, R. A., GaN evaporation in molecular beam epitaxy environment (vol 74, pg 1854, 1999). *Applied Physics Letters* **1999,** *75*, 3035-3035.

144. Pisch, A.; Schmid-Fetzer, R., In situ decomposition study of GaN thin films. *J. Cryst. Growth* **1998,** *187*, 329-332.

145. Kukushkin, S. A.; Bessolov, V. N.; Osipov, A. V.; Luk'yanov, A. V., Mechanism and kinetics of early growth stages of a GaN film. *Phys. Solid State* **2002,** *44*, 1399-1405.

146. Shitara, T.; Nishinaga, T., Surface-diffusion length of gallium during MBE growth on the various misoriented GaAs(001) substrates. *Japanese Journal of Applied Physics Part 1-Regular Papers Short Notes & Review Papers* **1989,** *28*, 1212-1216.

147. Jensen, L. E.; Bjork, M. T.; Jeppesen, S.; Persson, A. I.; Ohlsson, B. J.; Samuelson, L., Role of surface diffusion in chemical beam epitaxy of InAs nanowires. *Nano Letters* **2004,** *4*, 1961-1964.

148. Chakrapani, V.; Thangala, J.; Sunkara, M. K., WO_3 and W_2N nanowire arrays for photoelectrochemical hydrogen production. *International Journal of Hydrogen Energy* **2009,** *34*, 9050-9059.

149. Hiramatsu, H.; Seo, W. S.; Koumoto, K., Electrical and optical properties of radio-frequency-sputtered thin films of $(ZnO)_5In2O3$. *Chemistry of Materials* **1998,** *10*, 3033-3039.

150. Ong, C. H.; Gong, H., Effects of aluminum on the properties of p-type Cu-Al-O transparent oxide semiconductor prepared by reactive co-sputtering. *Thin Solid Films* **2003,** *445*, 299-303.

151. Zhou, J. H.; Jin, C. G.; Seol, J. H.; Li, X. G.; Shi, L., Thermoelectric properties of individual electrodeposited bismuth telluride nanowires. *Applied Physics Letters* **2005,** *87*.

152. Protasenko, V.; Bacinello, D.; Kuno, M., Experimental determination of the absorption cross-section and molar extinction coefficient of CdSe and CdTe nanowires. *J. Phys. Chem. B* **2006,** *110*, 25322-25331.

153. Wang, W.; Jia, F. L.; Huang, Q. H.; Zhang, J. Z., A new type of low power thermoelectric micro-generator fabricated by nanowire array thermoelectric material. *Microelectron. Eng.* **2005,** *77*, 223-229.

154. Rao, A. M.; Ji, X. H.; Tritt, T. M., Properties of nanostructured one-dimensional and composite thermoelectric materials. *MRS Bull.* **2006,** *31*, 218-223.

155. Law, M.; Goldberger, J.; Yang, P. D., Semiconductor nanowires and nanotubes. *Annual Review of Materials Research* **2004,** *34*, 83-122.

156. Alvarez-Quintana, J.; Martinez, E.; Perez-Tijerina, E.; Perez-Garcia, S. A.; Rodriguez-Viejo, J., Temperature dependent thermal conductivity of polycrystalline ZnO films. *Journal of Applied Physics* **2010,** *107*, 063713-4.

157. Love, J. C.; Estroff, L. A.; Kriebel, J. K.; Nuzzo, R. G.; Whitesides, G. M., Self-assembled monolayers of thiolates on metals as a form of nanotechnology. *Chem. Rev.* **2005,** *105*, 1103-1169.

158. Wang, W.; Lee, T.; Reed, M. A., Mechanism of electron conduction in self-assembled alkanethiol monolayer devices. *Phys. Rev. B* **2003,** *68*, 035416.

159. Morita, T.; Kimura, S., Long-Range Electron Transfer over 4 nm governed by an inelastic hopping mechanism in self-assembled monolayers of helical peptides. *J. Am. Chem. Soc.* **2003,** *125*, 8732-8733.

160. Mozharivskyj, Y.; Janssen, Y.; Harringa, J. L.; Kracher, A.; Tsokol, A. O.; Miller, G. J., $Zn_{13}Sb_{10}$: a structural and Landau theoretical analysis of its phase transitions. *Chemistry of Materials* **2006,** *18*, 822-831.

161. Grazulis, S.; Chateigner, D.; Downs, R. T.; Yokochi, A. F. T.; Quiros, M.; Lutterotti, L.; Manakova, E.; Butkus, J.; Moeck, P.; Le Bail, A., Crystallography Open Database - an open-access collection of crystal structures. *Journal of Applied Crystallography* **2009,** *42*, 726-729.

162. Gražulis, S.; Daškevič, A.; Merkys, A.; Chateigner, D.; Lutterotti, L.; Quirós, M.; Serebryanaya, N. R.; Moeck, P.; Downs, R. T.; Le Bail, A., Crystallography Open Database (COD): an open-access collection of crystal structures and platform for world-wide collaboration. *Nucleic Acids Research* **2011**.

163. Elrod, U.; Luxsteiner, M. C.; Obergfell, M.; Bucher, E.; Schlapbach, L., Surface-chemistry of Zn_3P_2 single-crystals studied by XPS. *Applied Physics B-Photophysics and Laser Chemistry* **1987,** *43*, 197-201.

164. Bandyopadhyay, K.; Vijayamohanan, K.; Venkataramanan, M.; Pradeep, T., Self-assembled monolayers of small aromatic disulfide and diselenide molecules on polycrystalline gold films: a comparative study of the geometrical constraint using temperature-dependent surface-enhanced Raman spectroscopy, X-ray photoelectron spectroscopy, and electrochemistry. *Langmuir* **1999,** *15*, 5314-5322.

165. Rosario-Castro, B. I.; Fachini, E. R.; Hernandez, J.; Perez-Davis, M. E.; Cabrera, C. R., Electrochemical and surface characterization of 4-aminothiophenol adsorption at polycrystalline platinum electrodes. *Langmuir* **2006,** *22*, 6102-6108.

166. Arima, V.; Matino, F.; Thompson, J.; Cingolani, R.; Rinaldi, R.; Blyth, R. I. R., Ex-situ prepared films of 4-aminothiophenol on Au(111): photoemission, NEXAFS and STM measurements. *Surface Science* **2005,** *580*, 63-70.

167. Koestner, R. J.; Salmeron, M.; Kollin, E. B.; Gland, J. L., Adsorption and surface reactions of H_2S on clean and S-covered Pt(111). *Surface Science* **1986,** *172*, 668-690.

168. Franke, R.; Chasse, T.; Streubel, P.; Meisel, A., Auger parameters and relaxation of phosphorus in solid compounds. *J. Electron Spectrosc. Relat. Phenom.* **1991,** *56*, 381-388.

169. Gresch, R.; Mullerwarmuth, W.; Dutz, H., X-ray photoelectron spectroscopy of sodium phosphate glasses. *J. Non-Cryst. Solids* **1979,** *34*, 127-136.

170. Ocal, C.; Ferrer, S., The strong metal–support interaction (SMSI) in Pt–TiO_2 model catalysts. A new CO adsorption state on Pt–Ti atoms. *Journal of Chemical Physics* **1986,** *84*, 6474.

171. Carraher, C. E., Seymour, R. B., *Seymour/Carraher's Polymer Chemistry*. 6 ed.; CRC Press 2003; p 123.

172. Katsuyama, S.; Watanabe, M.; Kuroki, M.; Maehata, T.; Ito, M., Effect of NiSb on the thermoelectric properties of skutterudite $CoSb_3$. *Journal of Applied Physics* **2003,** *93*, 2758-2764.

173. Poudel, B.; Hao, Q.; Ma, Y.; Lan, Y. C.; Minnich, A.; Yu, B.; Yan, X. A.; Wang, D. Z.; Muto, A.; Vashaee, D.; Chen, X. Y.; Liu, J. M.; Dresselhaus, M. S.; Chen, G.; Ren, Z. F., High-thermoelectric performance of nanostructured bismuth antimony telluride bulk alloys. *Science* **2008,** *320*, 634-638.

174. Bux, S. K.; Fleurial, J.-P.; Kaner, R. B., Nanostructured materials for thermoelectric applications. *Chemical Communications* **2010,** *46*, 8311-8324.

175. von Stackelberg, M.; Paulus, R., Examinations on phosphides and arsenides of zinc and cadmium - The Zn_3P_2 lattice. *Zeitschrift für physikalische Chemie. Abteilung B, Chemie der Elementarprozesse, Aufbau der Materie* **1935,** *28*, 427-460.

176. Spitzer, D. P., Lattice thermal conductivity of semiconductors: a chemical bond approach. *Journal of Physics and Chemistry of Solids* **1970,** *31*, 19.

177. Yang, R.; Chueh, Y.-L.; Morber, J. R.; Snyder, R.; Chou, L.-J.; Wang, Z. L., Single-crystalline branched zinc phosphide nanostructures: synthesis, properties, and optoelectronic devices. *Nano Letters* **2006,** *7*, 269-275.

178. Nagamoto, Y.; Hino, K.; Yoshitake, H.; Koyanagi, T. *Thermoelectric properties of α-Zn_3P_2*. IEEE: New York, 1998; p 354-357.

179. Abreu, C. R. A.; Tavares, F. W.; Castier, M., Influence of particle shape on the packing and on the segregation of spherocylinders via Monte Carlo simulations. *Powder Technology* **2003,** *134*, 167-180.

180. Zhu, Y.; Xu, F.; Qin, Q.; Fung, W. Y.; Lu, W., Mechanical properties of vapor−liquid−solid synthesized silicon nanowires. *Nano Letters* **2009,** *9*, 3934-3939.

181. Stan, G.; Krylyuk, S.; Davydov, A. V.; Levin, I.; Cook, R. F., Ultimate bending strength of Si nanowires. *Nano Letters* **2012,** *12*, 2599-2604.

182. Hoffmann, S.; Utke, I.; Moser, B.; Michler, J.; Christiansen, S. H.; Schmidt, V.; Senz, S.; Werner, P.; Gösele, U.; Ballif, C., Measurement of the bending strength of vapor−liquid−solid grown silicon nanowires. *Nano Letters* **2006,** *6*, 622-625.

183. Gordon, M. J.; Baron, T.; Dhalluin, F.; Gentile, P.; Ferret, P., Size effects in mechanical deformation and fracture of cantilevered silicon nanowires. *Nano Letters* **2009,** *9*, 525-529.

184. Bergman, T. L.; Incropera, F. P., *Fundamentals of heat and mass transfer*. 7th ed.; Wiley: Hoboken, NJ, 2011; p 78.

185. Yang, R. G.; Chen, G., Thermal conductivity modeling of periodic two-dimensional nanocomposites. *Phys. Rev. B* **2004,** *69*.

186. Chen, G., Thermal conductivity and ballistic-phonon transport in the cross-plane direction of superlattices. *Phys. Rev. B* **1998,** *57*, 14958-14973.

187. Dresselhaus, M. S.; Chen, G.; Tang, M. Y.; Yang, R. G.; Lee, H.; Wang, D. Z.; Ren, Z. F.; Fleurial, J. P.; Gogna, P. In *Materials and Technologies for Direct Thermal-to-Electric Energy Conversion*, Pittsburgh, Pa2005; J. Yang, T. P. H., R. Funashahi, G. S. Nolas, Ed. Materials Research Society Press: Pittsburgh, Pa; pp 3-12.

188. Yee, S. K.; Coates, N. E.; Majumdar, A.; Urban, J. J.; Segalman, R. A., Thermoelectric power factor optimization in PEDOT:PSS tellurium nanowire hybrid composites. *Physical Chemistry Chemical Physics* **2013,** *15*, 4024-4032.

189. Kanatzidis, M. G., nanostructured thermoelectrics: the new paradigm? *Chemistry of Materials* **2010,** *22*, 648-659.

190. Babu, V. S.; Vaya, P. R.; Sobhanadri, J., Electrical and thermoelectrical properties of Zn_3P_2 films grown by the hot wall epitaxy technique. *Journal of Applied Physics* **1988,** *64*, 1922.

191. Yoon, M. H.; Lee, S. H.; Park, H. L.; Kim, H. K.; Jang, M. S., Solid solubility limits of Ga and Al in ZnO. *Journal of Materials Science Letters* **2002,** *21*, 1703-1704.

192. Palmer, G. B.; Poeppelmeier, K. R., Phase relations, transparency and conductivity in Ga_2O_3-SnO_2-ZnO. *Solid State Sciences* **2002,** *4*, 317-322.

193. Colinas, J. M. F.; Areán, C. O., Kinetics of solid-state spinel formation: effect of cation coordination preference. *Journal of Solid State Chemistry* **1994,** *109*, 43-46.

194. Munir, Z.; Anselmi-Tamburini, U.; Ohyanagi, M., The effect of electric field and pressure on the synthesis and consolidation of materials: a review of the spark plasma sintering method. *J Mater Sci* **2006,** *41*, 763-777.

195. Noh, J.-Y.; Kim, H.; Kim, Y.-S.; Park, C. H., Electron doping limit in Al-doped ZnO by donor-acceptor interactions. *Journal of Applied Physics* **2013,** *113*, 153703-5.

196. Hansson, R.; Hayes, P.; Jak, E., Experimental study of phase equilibria in the Al-Fe-Zn-O system in air. *Metall and Materi Trans B* **2004,** *35*, 633-642.

197. Hu, J.; Gordon, R. G., Textured aluminum-doped zinc oxide thin films from atmospheric pressure chemical-vapor deposition. *Journal of Applied Physics* **1992,** *71*, 880-890.

198. Hu, J.; Gordon, R. G., Atmospheric pressure chemical vapor deposition of gallium doped zinc oxide thin films from diethyl zinc, water, and triethyl gallium. *Journal of Applied Physics* **1992,** *72*, 5381-5392.

199. Jaworski, C. M.; Kulbachinskii, V.; Heremans, J. P., Resonant level formed by tin in Bi_2Te_3 and the enhancement of room-temperature thermoelectric power. *Phys. Rev. B* **2009,** *80*, 233201.

200. Heremans, J. P.; Jovovic, V.; Toberer, E. S.; Saramat, A.; Kurosaki, K.; Charoenphakdee, A.; Yamanaka, S.; Snyder, G. J., Enhancement of thermoelectric efficiency in PbTe by distortion of the electronic density of states. *Science* **2008,** *321*, 554-557.

201. Heremans, J. P.; Wiendlocha, B.; Chamoire, A. M., Resonant levels in bulk thermoelectric semiconductors. *Energy & Environmental Science* **2012,** *5*, 5510-5530.

202. Anderson, J.; Chris, G. V. d. W., Fundamentals of zinc oxide as a semiconductor. *Reports on Progress in Physics* **2009,** *72*, 126501.

203. Imai, Y.; Watanabe, A., Comparison of electronic structures of doped ZnO by various impurity elements calculated by a first-principle pseudopotential method. *Journal of Materials Science: Materials in Electronics* **2004,** *15*, 743-749.

204. Imai, Y.; Watanabe, A.; Shimono, I., Comparison of electronic structures of doped ZnS and ZnO calculated by a first-principle pseudopotential method. *Journal of Materials Science: Materials in Electronics* **2003,** *14*, 149-156.

205. Tsidil'kovskiĭ, I. M., Zero-gap semiconductors with magnetic impurities forming resonance donor states. *Soviet Physics Uspekhi* **1992,** *35*, 85.

206. S.M. Sze, K. K. N., *Physics of Semiconductor Devices*. 3 ed.; John Wiley & Sons 2007.

207. Fistul', V. I., *Heavily Doped Semiconductors*. Plenum Press: New York, NY, 1969.

208. Baer, W. S., Faraday Rotation in ZnO: Determination of the electron effective mass. *Physical Review* **1967,** *154*, 785-789.

209. May, A. F.; Toberer, E. S.; Saramat, A.; Snyder, G. J., Characterization and analysis of thermoelectric transport in n-type $Ba_8Ga_{16-x}Ge_{30+x}$. *Phys. Rev. B* **2009,** *80*, 125205.

210. Sales, B. C.; Mandrus, D.; Chakoumakos, B. C.; Keppens, V.; Thompson, J. R., Filled skutterudite antimonides: electron crystals and phonon glasses. *Physical Review B* **1997,** *56*, 15081-15089.